HOST GUEST COMPOSITES BASED ON NANOPOROUS MATERIALS

By

Xiaoming Zhang

A dissertation submitted to the Graduate Faculty in Chemistry in partial fulfillment of the requirements for the degree of Doctor of Philosophy, The City University of New York

2006

UMI Number: 3187806

ProQuest Information and Learning Company
300 North Zeeb Road
P.O. Box 1346
Ann Arbor, MI 48106-1346

This manuscript has been read and accepted for the graduate faculty in Chemistry in satisfaction for the dissertation requirement for the degree of Doctor of Philosophy

Date Chair of Examining Committee: Daniel L. Akins

Date Executive Officer: Gerald Koeppl

Michael C. Drain

James D. Batteas

THE CITY UNIVERSITY OF NEW YORK

ACKNOWLEDGMENTS

In retrospect of the past years, I have always realized that there are many people who have directed, assisted and supported me during my Ph.D study. Without them I would never be able to reach this stage in my scientific growth. Although it would be impossible to name each of them, I would like to express my deep gratitude to all of them. First, I would like to thank my mentors, Dr. Daniel L. Akins and Dr. James Batteas, for their tremendous effort in guiding, helping and encouraging me. Their broad knowledge, insightful thoughts and sparkling ideas have significantly widened my horizons and inspired my research. Personally, I have also greatly benefited from their devoted, energetic and enthusiastic manner towards science. I also thank a member of my candidacy exam and dissertation committee, Dr. Charles M. Drain, for his time and valuable suggestions.

I would like to thank many of my collaborators and associates. I specially thank Ms. Sandra Smith for her valuable guidance and assistance when I first started my research at the City College of the New York. Many thanks are due to Mr. Hanru Zhu, who has provided generous help in my research, especially in the intramolecular charge transfer project. Many thanks go to all my labmates, Dr. Hui Yang, Dr. Metin Adyin, Dr. Yanting Liao, Nathan Stevens, Fleumingue Jean-Mary, Philippe Mercirer, Shiunchin C. Wang, and Dionne Miller. They have greatly enriched my experience at the City College and brought me many cherishable memories.

I also want to thank many members of the Department of Chemistry at City College, including all professors, staff and my fellow graduates, for providing such a

joyful study and work environment.

I am grateful to my parents, Mr. Yisheng Zhang and Mrs. Yuefang Wang, and my sister, Ms. Xiaohui Zhang, for their continuous encouragement and unconditional love throughout. I shall be indebted to them forever. Finally, I want to thank my wife, Dr. Haiquan Guo and daughter Michelle. It is their always being there, brightening my spirit, keeping my heart warm, and making my everyday meaningful and happy.

ABSTRACT

HOST GUEST COMPOSITES BASED ON NANOPOROUS MATERIALS

By Xiaoming Zhang

Advisor: Professor Daniel L. Akins

Porous materials are used as adsorbents, catalysts and catalyst supports owing to their high surface areas and large pore volumes. This dissertation describes methods of preparing nanocomposites from mesoporous silicates with uniform channel structures, as well as some of their applications. Functional groups have been placed selectively on the internal or external pore surfaces. Organic functionalization of these solids permits tuning of the surface properties (hydrophilicity, hydrophobicity, binding to guest molecules), alteration of the surface reactivity, protection of the surface from attack, and modification of the bulk properties (e.g., mechanical or optical properties) of the material. Recent applications of modified mesoporous silicates are highlighted, including catalysis, adsorption of metals, anions, and organics, fixation of biologically active species, and optical applications.

For these reasons, three different kinds of molecules were successfully encapsulated within the channels of the mesoporous materials. Novel properties were found to be result from the confinement within the cavity of the matrices.

DCM is a well-known laser dye that has high fluorescence efficiency and is photochemically stable. We have been able to observe the dual emission from the by encapsulation of dye molecules within an alumino-MCM-41. The interaction between DCM and the internal surface of MCM-41 was found to modify the optical properties

of the confined DCM molecules. The dynamics of DCM in MCM-41 was found to correspond to a biexponential relaxation with one component of 0.6 ns (57%) and a very long component of 1.9 ns (43%).

Nanostructural ferric oxide was encapsulated within porous silicate matrices, resulting in the formation of nanocomposites. The resulting nanocomposites were characterized by UV–vis, IR, TEM, EPR and X-ray diffraction. EPR measurements indicate that the various nanocomposites (whose dimensions were controllable by the pore sizes of the silicate materials), when sufficiently loaded with small Fe_2O_3 nanoparticles, possess nonzero absorptions at zero applied magnetic field, as well as significant microwave absorption capacities as a function of applied magnetic field strength.

The novel polyoxometalate ($Eu_8P_4W_{43}$) has been immobilized inside the channels of MCM-41 mesoporous molecular sieve material by means of the incipient wetness method. For proper host-guest interaction, amine groups were introduced into the system as a result of an aminosilylation procedure. A stable and integrated $Eu_8P_4W_{43}$ polyoxometalate was shown to be formed inside the channels of he modified MCM-41. The products were characterized by XRD, UV-Vis absorption, emission, Raman excitation, Raman and ^{31}P solid-state NMR measurements. A strong photoluminescence suggests the potential utility of the polyoxometalate as a luminescent material.

PREFACE

The overall objective of the dissertation is to develop new functional materials, specifically, nanostructured porous composites, for potential applications in uses of electro-optical devices, magnetic materials, and drug delivery systems. Two main considerations are present throughout this dissertation. Firstly, the efforts focus on constricted syntheses within mesoporous materials of guests (e.g., dye molecules, polyoxometalates, and Fe_2O_3) within solid matrices, for their optical spectroscopic and other potentially useful properties. Secondly, it is always desirable to have versatile and controllable synthesis process and products. Of our special interest is the versatile of the new developed sol-gel pathway. Materials with different morphologies and composition can be produced and the entire process can be fine tuned. The organization of the dissertation is as follows.

Chapter 1 is an overview of synthesis and characterization of nanostructural materials. Based on an introduction of fundamental sol-gel chemistry, nanocomposites with mesoporous materials are described in detail. Discussions include the template species, templating mechanisms, reaction conditions and encapsulation methods. Description of general characterization and testing methods for porous materials is also provided.

In Chapter 2, we try to provide a summary of the spectroscopic characteristics of DCM. We employed time dependent density functional theory (TD-DFT) on DCM to investigate Potential Energy Surfaces (PES) of the ground and excited states in gas phase. The results suggested that the rotation of the donor group is more favorable

candidate for the intramolecular charge transfer presses of the DCM. We also studied TICT of DCM encapsulating inside channels of MCM-41. In particular, two fluorescence bands are observed for DCM occluded within MCM-41. The dual bands are attributed to emissions from the lowest excited (LE) state and a state created as a result of intramolecular charge transfer, specifically, the twisted intramolecular charge transfer (TICT) state. The decay lifetimes for the LE and TICT states are found to be 0.6±0.1 and 1.9±0.1 ns, respectively. The single emissions from the DCM/Y-zeolite composite and the homogeneous DMSO solution show single exponential decays with lifetimes of 1.3±0.1 and 2.0±0.1 ns, respectively, both assigned to the TICT state.

In Chapter 3, Nanostructural ferric oxide was encapsulated within one-dimensional (1-D) silicate mesoporous molecular materials, resulting in the formation of nanocomposites. The resulting nanocomposites were characterized by UV-vis, IR, TEM, EPR and X-ray diffraction. The occluded Fe_2O_3 nanostructures were found to evince optical spectra and magnetic properties that were significantly different from that of bulk Fe_2O_3. EPR measurements indicate that the various nanocomposites (whose dimensions were controllable by the pore sizes of the silicate materials), when sufficiently loaded with small Fe_2O_3 nanoparticles, possess nonzero absorptions at zero applied magnetic field, as well as significant microwave absorption capacities as a function of applied magnetic field strength. By choosing different matrices, we studied effects of the particle size and morphology on the magnetic behaviors. It was found that the pore dimension of the matrix plays a crucial role in the magnetic properties of the resultant nanocomposite.

Chapter 4 describes the development of a synthetic route to prepare magnetic

Fe_2O_3 nanoparticles via sol-gel process. The study demonstrates the morphological controllability of the sol-gel templating method. The experimental method, material characterization and template effect on pore structures are discussed. In this work, amorphous SiO_2 was selected as host because it has been proven previously a very effective and biofriendly matrix. With well-defined morphology and nanostructure, the nanospheres are potentially useful for a variety of applications, such as drug delivery, bio-sensor and catalyst.

Chapter 5 presents the studies on novel polyoxometalate (POM, $[(Eu_2PW_{10}O_{38})_4(W_3O_8(H_2O)_2(OH)_4]^{22-}$) nanoparticles dispersion in mesoporous silica matrices MCM-41 for the perceivable application in functional luminescent materials. The POM-silica nanocomposites were prepared through a surface-modificated pathway. The obtained nanocomposites exhibit mesoporosity of the silica framework as well as the unique size dependent optical properties of the second material phase, i.e., POM nanoparticles. The products were characterized by XRD, UV-Vis absorption, emission, Raman excitation, and Raman measurements. Infrared and Raman spectra of the polyoxometalate/MCM-41 composite systems are interpreted as showing electrostatic interaction induced spectral shifts. The photoluminescent behavior of the composite at room temperature indicates a characteristic Eu3+ emission pattern for $5Do–7F_J$ transitions. The characteristics of the materials such as composition, morphology, porosity, and optical properties are discussed.

In Chapter 6, Eu(III) doped MCM-41 and Nb_2O_5 were studied. Surface valence transition of Eu(III) and Eu(II) is observed, which is much stronger in Nb_2O_5 mesoporous matrix. $7F_j \rightarrow 5L_6$ transitions around 394nm is totally shielded for Eu(III)

in MCM-41. But this band can be found in Eu(III)/Nb_2O_5 composite. For the MCM-41, which consists of a corner-sharing network of tetrahedally coordinated SiO_4 unites, only has low vibration quanta, which are not expected to contribute much to nonradiative deactivation of the excited state of the lanthanide ions. And Eu(III) in MCM-41, the magnetic dipole transition is more obvious than that of Eu(III) in Nb_2O_5.

TABLE OF CONTENTS

LIST OF TABLES

LIST OF FIGURES

Chapter 1 Introduction

1.1 Chemistry of Advanced Materials

Since the past two decades, there have been major advances in materials chemistry and the subject is growing rapidly. Some examples include high-temperature cuprate superconductors (1986), fullerenes (1990), mesoporous silica (1992) and colossal megnettoresistance (CMR) in manganates (1993), etc. Nowadays, materials chemistry has become a new branch of modern chemistry related to the development of high technological materials [1, 2].

The most important motivation of materials chemistry is to understand, to predict, and to design the properties of materials with respect to chemical composition, crystal and electronic structures [3]. Today's materials chemistry is concerned with the development of new synthesis methods, new ways of identifying and characterizing materials and of describing their structures. Although there have been major advances in the synthesis of materials, we are still far away from a tailor-making of materials with specified structures/properties. Most of the discoveries of new functional materials still have been made by chance. Therefore, rational design and synthesis of novel materials have remained important objectives. The control over the composition is often possible, but still then there must be a way of producing materials in any required nanoscopic shape or form. Also, the characterization is a critical ingredient to progress, because it provides guidance for further research efforts [4].

1.2 Nanotechnology and Nanomaterials

Nanotechnology is concerned with the development of novel methods for the synthesis and characterization of chemical systems within the size range of about 1 to 100 nm [5]. The interest in nanoscale objects is due to the exhibition of novel electronic, optical, magnetic, transport, photochemical, electrochemical, catalytic and mechanical behavior, depending on composition, size, and shape of the particles. The physical properties of nanoparticles correspond neither to those of the free atoms or molecules making up the particle nor to those of the bulk solids with identical chemical composition [6]. It is astonishing that many relevant phenomena at nanoscale are caused by the tiny size of the organized structure and by interactions at their predominant and complex interfaces [7]. Once the chemists are able to gain control over size and shape of the particles, further enhancement of material properties and device functions will surely be possible. Each change in both, composition or size can lead to different physical and chemical properties, providing a large number of new materials [8].

The most important aspect is still the development of new strategies for the synthesis of nanomaterials, particularly soft chemical routes. But the chemist not only has to be able to synthesize perfect, i.e., monodispersed and shape-defined objects having nanometer dimensions, but also he may have to position these objects in appropriately organized arrays. This may be tackled either by using lithographic techniques [9] or templating methods (molecular and supramolecular assembly processes, [10] or deposition inside nanoporous host materials [11]). However, the templating methods may become the most

favorable in the far run towards directed self-assembly.

1.3 Properties of Nanostructural Materials

Nanomaterials are single-phase or multiphase polycrystals with a typical crystal size of 1 to 100 nm in at least one dimension. Depending on the dimensions they can be classified into (a) nanoparticles (0D), (b) filamentary structures or nanowire (1D), (c) layered or lamellar structures (2D), and (d) bulk nanostructured materials (3D).

Nanoscale structures offer great potential for advancements in electronics, optioelectronics, magnetic storage, and biomedical applications. These nano-sized materials display properties that differ from their respective bulk material counterparts. Size and surface effects dominate the behavior of nanoparticles. The details of the relationships between shape, surface structure, composition and the resulting properties of nanoparticles are currently unclear. Now we know that the properties of nanomaterials mainly depend on four features, namely (a) grain size and size distribution, (b) chemical composition, (c) presence of interfaces (grain boundaries, free surface), and (d) interactions between the constituent domains [12]. Due to these four features in nanophase materials (Figure 1-1), a variety of size-related effects can be introduced [13]:

1) The density of dislocation, interface to volume ratio and the grain size strongly influence the mechanical properties.

2) Quantum confinement, i. e., quantization of the energy levels of the electrons due to confined grain size, has applications in semiconductors, optoelectronics, and non-linear optics. Quantum dots can be developed to emit and absorb a specific wavelength of light by changing the particle diameters.

3) The large amount of surface atoms increases the activity for catalytical applications.

4) The magnetic properties of nano-sized particles depend on the large surface to volume ratio. Unlike bulk materials consisting of multiple magnetic domains, several small ferromagnetic particles can form only a single magnetic domain, giving rise to superparamagnetism. This behavior opens the possibility for uses in information storage.

1.4 Fabrication and Characterization of nanomaterials

In general, synthetic methods for the fabrication of materials with nanometer scale dimensions can be classified into two categories: one from molecular precusors such as most chemical methods (bottom up), the other from processing of bulk precursors such as mechanical attrition (top down).

Chemical methods are widely used for fabrication of nanoparticles and nanocomposites. Some most frequently used are precipitation, reduction, pyrolysis, aerogel/xerogel process, reverse micelle microemulsion, etc. That is partly due to mild reaction conditions, and less expensive equipment needed. It has been observed that the fabrication techniques have greatly influence on the properties of nanoparticles,

even though they have the same grain size. Some chemical techniques also provide great control over the size and size distribution of particles such as reverse micelle synthesis. This part will survey the recently applications of matrix-mediated methods (especially mesoporous materials as hosts).

1.4.1 Matrix-Mediated Method

Matrix-mediated or confined synthesis means that a rigid structure is provided to act as a host or matrix for the confined growth of the nanoscale particles. Several such host materials have been explored including those based on organic resins, polymers, zeolite, and mesoporous solids. The host or matrix not only provides spatially localized sites for nucleation but also imposes an upper limit on the size of the nanoparticles. As a result, this method will produce the nanoparticles with uniform dimensions.

1.4.1.1 Mesoporous Materials

The discovery of the M41S series ordered mesoporous materials in 1992 has drawn great interests because they are promising as catalyst in their own right and also proved to be of useful as catalyst support, separation medium, and host material for inclusion compounds [14]. Since then, numerous mesoporous or nanoporous silicate and other metal oxides with narrowly distributed pore diameters of 2-50 nm have been prepared through various synthetic routes and strategies to contain a wide diversity of materials of various framework chemical compositions and pore structures [15-17]. In most of the studies, charged (cationic and anionic) and neutral surfactants have been employed as templates, which direct the mesophase formation based on the electrostatic interaction and hydrogen-bonding interactions, respectively. The synthesis, stabilization,

modification, application, structure characterization, mechanistic study, structural simulation and computational modeling of the ordered molecular sieves have been extensively studied and reviewed [18].

The originally proposed mechanic pathways of the formation of the MCM-41 structure are illustrated in Figure 1-2. In the first, the presence of the liquid-crystal mesophase prior to the addition of the reagents, i.e., preexistence of surfactant aggregates (rodlike micelles), followed by the migration and polymerization of silicate anions, results in the formation of the MCM-41 structure. The second postulates self-assembly of the liquid-crystal-like structures as a result of the mutual interactions between the silicate anion and the surfactant cations in the solution, i.e., the silicate species generated in the reaction mixture influence the ordering of the surfactant micelles to the desired liquid-crystal phase. Further, the formation of hexagonal, cubic, and lamellar structures through variations in the silica concentration at constant surfactant concentration. By covalently anchoring a number of functional groups to the channel walls, the internal surface reactivity of the mesoporous hosts can be modified. The attachment of ligands can also be used to induce the molecules inside the channel or even to form the bulky metal complexes.

No doubt, those mesoporous materials opens definitive new possibilities for preparing catalysts with uniform pores in the mesoporous region, which should importantly allow the relatively large molecules present in crude oils and in the production of fine chemicals to react. MCM-41 can act just as molecular “factories” where quantum sized particles can be manufactured inside. The uniform pore structures of molecular sieves can act as solid solvents to control the particle size and

topology. Various metals, metal oxides, semiconductor clusters and nanowires, organic and organometallic compounds were within MCM-41.

1.4.1.2. Nanocomposites from Mesoporous Materials

Mesoporous materials are of great research interests for their potential application as catalysts, absorbents, chemical sensors and optical/electronic nanodevices, etc. Mesoporous materials, due to their periodic and size-controllable pore channels (2-10 nm) and high surface areas, have been regarded as a "natural micro-reactor" for the construction of novel ordered and well dispersed nanocomposites with controlled size and size distribution [19,20]. Many novel processes for the introduction of guest nanomaterials to the pore channels of mesoporous materials have given new nanocomposites with significantly improved performance. The critical significance of encapsulation of molecules inside the channel of mesoporous material is evident from the fact that many commercial processes rely on immobilized catalysts and process economy demands a repeated use of catalyst.

There are several routes to introduce inorganic or organic guests into the host pore channels. Here in this section, we will focus on the following four kinds of routes: 1) co-condensation method; 2) wetness impregnation and ion exchanging; 3) covalent bonding; and 4) surface modification method, to prepare nanocomposite with novel catalytic, optical, electronic and magnetic properties.

Co-condensation method. Co-condensation, also called a one-pot process, is the simplest method to introduce compounds into channels of mesoporous materials [20]. It usually leads to the highly-dispersed doping of compounds into the framework of

mesoporous materials. Otherwise, embedding of the guest in the framework prevents their contact with the reactants in a catalytic process which limits their application to a certain extent.

Wiesner and his group [21] presented a simple block-copolymer-based one-pot self-assembly approach to synthesize mesoporous aluminosilicate materials with superparamagnetic Fe_2O_3 particles embedded in the inorganic walls. The pore blocking by outwards-dispersed particles is avoided, even for high metal oxide loadings. The authors believed that these multifunctional nanostructured materials were likely to be applied in novel biopolymer separation technologies, which combines size-exclusion principles and the separation function of magnetically labeled materials. Rare earth oxides have also been incorporated into the pore walls of mesoporous materials by a solution chemical co-condensation process [22-25].

Wetness impregnation and ion exchanging. The wetness impregnation is another widely used technique. Here the precursor is dissolved in aqueous or non-aqueous media using volumes equal to the pore volume of the support and contacted with the carrier. Rare earth oxides were dispersed in SBA-15 by a solution impregnation method with subsequent calcinations [26]. Further analyses showed that rare earth oxide coatings had formed on the pore wall surface. Through high temperature thermal treatment, the guest oxides would most probably diffuse into the pore channels. For example, when the mesoporous silica MCM-41 doped with Eu^{3+} ions was treated at around 1273 K, $Eu_8(SiO_4)_6$ crystalline nanorods formed and grew along the pore channels, which showed remarkable luminescence enhancement compared to $Eu_8(SiO_4)_6$ crystals synthesized by common sol-gel

methods.

Ion exchange and wet impregnation often result in low guest dispersion because the metal salts can easily diffuse onto the outer surface of the host silica during the reduction or thermal treatment process, thus large metal particles could readily form on the particle surface. In order to avoid this, researchers have tried various different approaches including surface modification and in-situ reduction techniques.

Covalent bonding. This is a common way to introduce oxides and sulfides into mesoporous materials by the covalent grafting of ligands, including metal complexes [27], organometallic compounds [28], and chlorides [29]. These compounds all contain active ligands that can be attached to the inner surface *via* direct reaction with Si-OH groups.

As a wide bandgap semiconductor, TiO_2 of controlled size and structure is of great interest because of its excellent photocatalytic activity and electronic properties [27]. Most of the Ti precursors can hydrolyze to form Ti-O- bonds and easily bind to the pore surface of ordered mesoporous silica *via* Ti-O-Si covalent bonds. It is a common method to reflux the mixture of the mesoporous materials and the toluene solution of Ti precursor for the introduction of Ti into mesoporous materials. These TiO_2-containing composites showed good activity in the photodecomposition of phenol and photoreduction of Cr(VI) to Cr(III).

Surface modification method. Organic functionalization of silicates permits precise control over the surface properties, modification of the hydrophilic/hydrophobic of the surface, alteration of the surface reactivity, protection of the surface from attack,

modification of the bulk properties of the materials and at the same time stabilizing the materials towards hydrolysis (please see figure 1-3). By modifying the MCM-41 with ethylenediamine groups, which could coordinate inorganic and organic guests inside mesoporous materials [30]. For the semiconductor nanoclusters of TiO_2 and ZnO confined in a mesoporous matrix, both of their optical absorption spectra showed massive blue shifts relative to their bulk materials. This organosilane coupling route can be employed to synthesize many host-guests nanocomposites.

Highly dispersed ZnS nanoclusters have also been synthesized in ethylenediamine functionalized mesoporous silica MCM-41 [31]. Compared with the sample prepared by a simple ion-exchange method, the amount of ZnS on the external surface is much lower. ZnS mainly formed, and was retained, in the channels of the MCM-41 host, and its growth was controlled well by the channels.

By using a new surface modification and ion-exchange reaction, CdS nanoparticles confined in mesoporous silica have been reported [32]. The mesoporous materials were functionalized selectively to minimize the uncontrolled precipitation reactions of Cd^{2+} outside the mesopores. The onset UV-Vis absorption of the composite shows a significant blue shift to that of the bulk CdS. Hirai *et al.* [33] incorporated CdS nanoparticles into thiol-modified MCM-41, using a reverse micelle system. Using mesoporous material templates with different pore diameter, the size-selectivity of CdS nanoparticles has been realized. It was demonstrated that the composites had a good photocatalytic activity for H_2 generation from 2-propanol aqueous solution. Thereafter Dr. D. L. Akins [34]

compared the optical properties of CdS nanoclusters formed in two mercapto-modified ordered mesoporous silica templates with different pore sizes. Except an obvious blue shift of absorption band-edge at decreased CdS particle size, the photoluminescence from these composites showed substantial Stokes shifts, which increases with the decrease of the nanoparticle size. The authors concluded that the photoluminescence derives from the recombination of holes and electrons at surface traps whose concentration increases with decreasing particle size.

Very recently, Mokaya *et al.* [35] reported the successful preparation of zinc phthalocyanine (ZnPc)-containing transparent mesoporous thin films or monoliths *via* a one-step synthesis or a post-synthesis adsorption route. An interesting result was reported by Kuroda *et al.*,[36] with a highly aligned mesoporous thin film as the matrix to incorporate cyanine dyes. In its visible absorption spectra, not only an absorption maximum at 525 nm resulting from the dye monomers, but also the polarization dependence of the absorbance, can be observed. Obviously, for the film with aligned mesochannels, its absorbance depends on the relative orientations of the polarized incident light and mesochannels alignment.

Molecular guests confined in the pore channels of mesoporous materials show special chemical and/or physical properties, *e.g.*, enhanced catalytic activity, predominant quantum size effect, *etc.* The highly dispersive and narrow-sized guests in mesoporous materials are especially favorable for catalytic applications if the pore structure still remains open for the easy access of reactants. In contrast, the complete and homogeneous filling of the pore channels of mesoporous materials with functional guests become essential for the preparation of nanowires or nanostructures for potential application in future opto-

electronic nanodevices. Inclusion chemistry of non-silica mesoporous materials has also been presenting greater challenges. More extensive investigations on the various kinds of properties of the host-guest nanocomposites are underway.

1.4.2 Characterization Methods

One of the most important recent developments in materials science is the ability to engineer material microstructures at the atomic level. While in its early stages of development, this capability offers the potential for significant increases in the performance capabilities of structural materials. Now it is very important that appropriate materials characterization techniques be developed to quantitatively evaluate the microstructural features of nanomaterials.

1.4.2.1 Transmission Electron Microscopy

Transmission Electron Microscopy (TEM) is a versatile tool capable of characterizing the internal structure of a wide variety of materials, including particle size, morphology and crystal structure. This characterization includes not only the imaging of the microstructure directly but at the same time, the identification of the phases present in the specimen by either electron diffraction or spectroscopic chemical analysis. The results obtained from a typical TEM characterization of materials allow a better understanding of the relation between microstructure and properties.

1.4.2.2 Raman / Infrared Spectroscopy

In nanosize powders the surface species absorption can compete with the absorption of the bulk species. Therefore, the characterization of these powders cannot

be complete without the identification of the surface chemical species. FTIR can be utilized to analyze the surface contamination. Typically there will be contamination from atmospheric CO_2, water and hydrocarbons. Especially oxide surfaces that are always more or less hydrolyzed can easily adsorb water molecules and CO_2 to form carbonate species.

1.4.2.3 X-Ray Diffraction

A rich variety of information can be extracted from X-ray Diffraction (XRD) measurements. From the position and shape of the lines, one can obtain the unit cell parameters and microstructural parameters (grain size, microstrain, etc.) respectively. By using the flexibility of a four circle diffractometer one can obtain information about the distribution of the orientation of the crystallites (texture measurements).

X-ray diffraction analysis was used to study the crystallinity of powder samples. This method can be used for phase identification, grain and unit cell size determination. Several Guiner cameras and diffractometers were utilized in these studies but in all cases Cu $\alpha 1$ radiation with wavelength 1.5405 Å was used.

1.4.2.4 Atomic Force Microscopy

The atomic force microscope is one of about two dozen types of scanned-proximity probe microscopes. All of these microscopes work by measuring a local property - such as height, optical absorption, or magnetism - with a probe or "tip" placed very close to the sample. The small probe-sample separation (on the order of the instrument's resolution) makes it possible to take measurements over a small area. To

acquire an image the microscope raster-scans the probe over the sample while measuring the local property in question. The resulting image resembles an image on a television screen in that both consist of many rows or lines of information placed one above the other.

1.4.2.5 Nitrogen adsorption

Nitrogen adsorption at 77 K is a commonly applied technique to determine various characteristics of porous materials. The amount of adsorbed nitrogen is measured as a function of the applied vapor pressure, which comprises the adsorption isotherm. The following characteristics are derived from the nitrogen adsorption isotherm: 1) pore volume; 2) surface area; 3) pore size distribution.

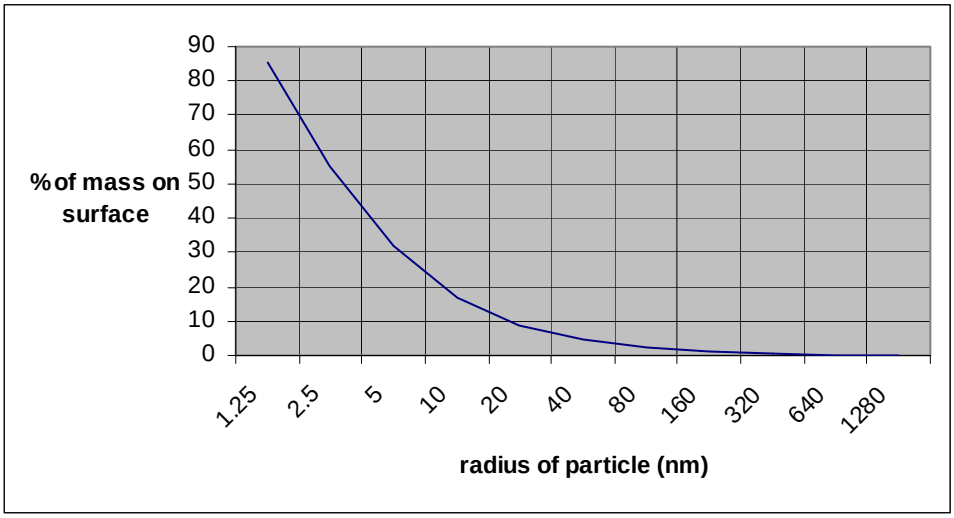

Figure 1-1: % Mass of surface atoms as a function of particle radius.

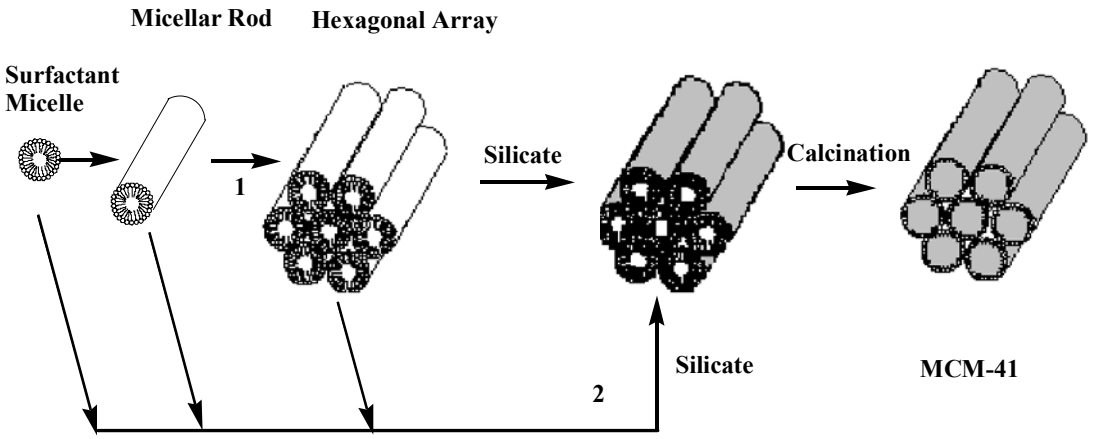

Figure 1-2 Possible mechanistic pathways for the formation of MCM-41: (1) liquid-crystal-phase-initiated and (2) silicate-anion-initiated.

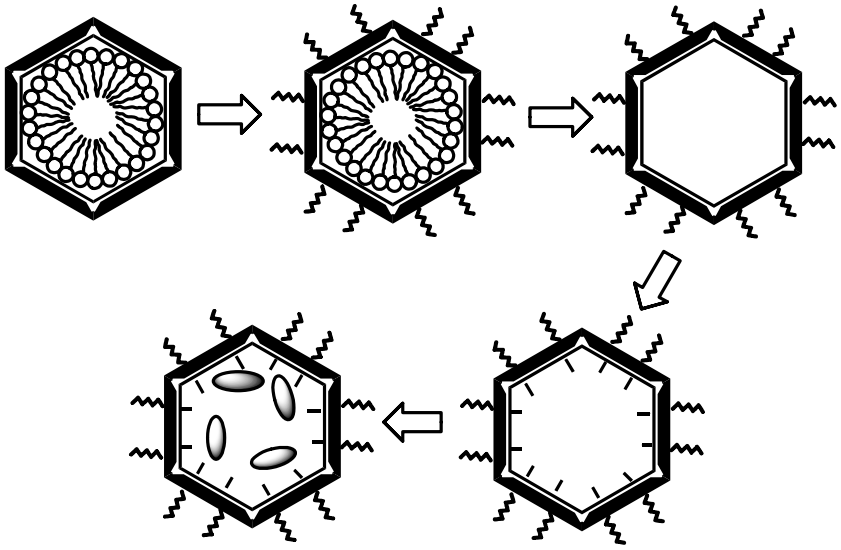

Figure 1-3 A schematic drawing of the synthesis of nanoparticles in the modified channels of mesoporous silica.

Chapter 2: Spectroscopy and Dynamics of DCM in Mesoporous Materials

2.1 Introduction

The photoreaction of p-dimethyl-aminobenzonitrile (DMABN) in solution led to the concept of *twisted intramolecular charge transfer* (TICT) [1-4]. Within this model, the excited state photoreaction of DMABN should involve an (approximately) 90° torsion of the dimethylamino group, producing a polar, charge-separated state. The internal twist is presumed to decouple the donor and acceptor centers in the molecule electronically. The concept was transferred to other molecules with substituents of electron-donating or -accepting character linked by flexible chemical bonds, so-called "TICT-compounds". As the fluorescence exhibited in the charge transfer state is red shifted with increasing solvent polarity and does not appear when the molecule is isolated, it is termed 'anomalous' fluorescence; if emission from the primarily excited precursor state can be recorded as well, one speaks of "dual emission". [5, 6]

It has been deduced that for DCM in its electronic excited state, an electron is intramolecularly transferred (i.e., an ICT occurs) from a so-called donor group to an acceptor group (both within the same molecule). In addition to ICT, DCM also undergoes either a twisting about an ethylenic double bond or about the bond joining the dimethylamino group and the aromatic ring, resulting in a twisted intramolecular charge-transfer (TICT) state [7,8]. As a result of interest in deciphering and quantifying rates for the several ultrafast processes that possibly exist, there have been several attempts to detail the primary photophysical processes for DCM. In general, it has been found that when polar solvents are used an emitting TICT state is formed, but

the elementary steps coupled to the ICT process are extremely fast and not quantifiable even with ultrafast instrumentation [9-12].

A widely investigated molecule in regards to TICT transformations is 4-(dicyanomethylene)-2-methyl-6-(*p*-dimethylaminostyryl)-4H-pyran (DCM; see Figure 2-1), a well known laser dye that has high fluorescence efficiency and is photochemically stable. The nature or existence of the charge transfer state of the TICT compounds has been the subject for a long time. It has been found that the bending of the cyano group connected with rehybridization of the carbon atom of the cyano group could be responsible for the charge transfer reaction. Independent of the torsional angle, the minimum energy in the excited state was always found for planarization of the amino group. In polar solvents, a 90°-twisted conformation represented the global minimum in the lowest electronic excited state. In confirmation of the TICT thesis, the twisted conformation was lower by 6 kJ/mol in energy than the 0° torsional conformation in acetonitrile. For DCM, it was found that there exists a large increase in dipole moment (from 14.3 to 22.5 D) upon a 90° twist of the dimethylamino group in S2. In contrast to the idea of a competition between the dimethylamino group rotation and the rotation around the central double bond, these processes were characterized as being independent of each other. No dipole moment increase was observed for other single bond rotations.

We used time dependent density functional theory (TD-DFT) on DCM to investigate potential energy surfaces (PES) of the ground and excited states in gas phase and also found the similar results.

The predicted PESs of the DCM as a function of rotation about double bond, trans to cis configuration as shown in Figure 2-2. The PES of the ground state (S_0) shows a high-energy barrier (2.61 eV), which prevents the trans to cis isomerization via rotation around centeral double bond. This prediction is consistent with the experimental observation that the trans- isomer of DCM is thermally stable without light exposure. At rotation of the double bond at 90 degree, there is a zwitterionic character of the S_1 state as expected. For the photo-isomerization in the S_1 excited state, there is a 0.56 eV energy barrier for the trans-perpendicular while there is almost no potential energy barrier for the cis-perpendicular energy pathway. Those predictions are consistent with the nanosecond laser photolysis experiments, which have proven that cis-trans photoisomerization efficiency is greater than that of the trans-cis photoisomerization. The PESs of the S_1 and S_0 state exhibit a strong avoiding crossing along trans-cis conversion. The predicted transition dipole moment suggest that the potential energy barrier of the S_0 state would have similar shape in polar and nonpolar environments as for that in gas phase. The energy deference between the trans to cis and cis to trans photoisomerization is about 0.46 eV. This prediction is in agreement with the experimental founding that the experimental shift between the emission spectra of the two DCM isomers (on solid samples) is about 0.3 eV.

The PESs for the rotation of the donor group of DCM from 0 to 180 degree is given Figure 2-3. For the rotation of the donor relative to phenyl ring, there is no any coupling between the singlet excited states. The S_1 excited state PES has an energy barrier about 0.27 eV around 60 degree and minimum at 90 degree while the S_2 states gradually increase and has a maximum energy barrier about 0.29 eV at 90 degree. The

energy difference between S_1 and S_2 state for planar structure is 0.47 eV. The predicted transition dipole moment for S_2 state increase from 0 degree thought 90 degree while that in the S_1 state decreases. This result suggests that in polar environments, the S_1 and S_2 states would be inversed and S_2 state may be responsible for the TICT process (S_2-TICT state). In nonpolar solvent or in gas phase, the predicted $S_0 \rightarrow S_1$ transition of the DCM is 2.86 eV in agreement with the experimental value of 2.79 eV(445nm) (DCM in hexane). Because of the surface touching between S_1 and T_2 PESs at the twisting angle 90 degree that might lead to $T_2 \rightarrow T_1$ transition following the $S_1 \rightarrow T_2$ (due to the intersystem crossing ISC). Since the $T_2 \rightarrow T_1$ is very efficient process which follows $S_1 \rightarrow T_2$ transition, molecule would have enough internal energy to overcome energy barrier along C=C bond rotation path on the relatively flat T_1 surface.

This process might be responsible for the trans and cis isomers on the S_0 potential energy surface of DCM since $T_1 \rightarrow S_0$ transition occurs more efficiently, which is in agreement with the experimental finding that the trans to cis photoisomerization of DCM in nonpolar environment has high quantum yield. The result also indicates that the electron densities in HOMOs and LUMOs levels of the DCM for planar and donor group rotated 90 degree relative to phenyl ring. In LUMO+1, the charge relatively transfers from donor to phenyl group at the donor 90 degree. The calculated net atomic charge of the DCM for the excited singlet states is calculated using HF method. The result indicates that there is a significant change for S_2 state in the charge distribution and dipole moment relative to ground state. The donor group losing about 0.5e, however, the phenyl ring gains 0.5e for the S_2 state and the dipole moment in S_2 state significantly increases as much as twice time.

We investigated PESs as function of the all-possible bond rotations. The results suggested that the rotation of the donor group is more favorable candidate for the intramolecular charge transfer presses of the DCM. For instance, the rotation of the acceptor part relative to the pyron ring that leads to transition dipole moments for all states decrease with increasing rotational bond angle of the acceptor and reach to zero at 90 degree.

In recent years, however, temporal dynamics of DCM in many organized assemblies, such as protein, DNA, cyclodextrin, microemulsions, micelles, lipid vesicles, sol-gel matrix and polymer cavities, have been analyzed [13-21]. In these organized and constricting media, the local polarity and viscosity differ from solution values and substantially influence the photophysics and chemical dynamics of photoreactions. In general, it has been found that the rate of the TICT process is considerably reduced in constricted environments, by several orders of magnitude, and it is possible to observe dual emissions. However, dual emissions from DCM have not been observed because the TICT transformation occurs too rapidly even using ultrafast laser spectroscopy. We report in this chapter the room temperature observation of dual emissions of DCM encapsulated in mesoporous MCM-41, resulting from reduced rates associated with photophysical relaxation processes.

2.2 Experimental Section

2.2.1 Synthesis of Modified Al Containing MCM-41

Polycrystalline powders of the mesostructural aluminosilicate MCM-41 were prepared by using cetyltrimethylammonium bromide (CTAB) as the template. Briefly,

Na_2SiO_3 (Aldrich, ~27% SiO_2) solution and a calculated amount of $NaAlO_2$ (Alfa) solution were added to CTAB (Aldrich) solution according to the molar composition ratio $5SiO_2$:xAl_2O_3:CTAB:$610H_2O$ (x=0.03-0.125). The pH was lowered to 11 with 2 M H_2SO_4 and the mixture was stirred for more than 3 h at about 318 K. Then the temperature was raised to 373 K and the reaction allowed for 72 h in a Teflon-lined autoclave. The resulting precipitate was filtered, washed thoroughly with distilled water, and calcined in air at 773 K to obtain the final product, MCM-41 (see discussion below for XRD patterns).

To stabilize the synthesized MCM-41 and allow DCM incorporation, it is necessary to modify the interior structure of MCM-41 through use of a silylation reagent (specifically, (aminopropyl)triethoxysilane, i.e., NH_2-$(CH_2)_3$-Si-$(C_2H_5O)_3$ (APTES)), thus linking oxygen atoms on the aluminosilicate surface and rigidifying the mesoporous framework, as well as satisfying guest-host intermolecular and/or electrostatic interactions. For our studies, the modified MCM-41 was prepared according to reference 22. Briefly, about 1.5 g of the calcined MCM-41 was mixed with a chloroform solution of APTES (100 ml, 0.2 M) and stirred overnight at room temperature. The precipitate was filtered and washed with chloroform and dichloromethane.

2.2.2 Formation of DCM/MCM-41 composites

DCM/MCM-41 composite was prepared by forming a mixture of 200 mg of modified MCM-41 with 10 ml of 1 g/l DCM in DMSO solution. The mixture was stirred at room temperature for more than 24 h, with the pH held at about 5.0 using 2 M

H_2SO_4. The suspension was then centrifuged. The residue was washed at least twice with DMSO to remove the DCM from the external surface, then dried at about 80 ^oC.

2.2.3 Formation of DCM/Y-Zeolite composites

Zeolite NH_3-Y (Alfa) was used as received. The zeolite sample was initially calcined at 450 ^oC. DCM/zeolite composite was prepared by stirring a mixture of 200 mg Y-zeolite in 10 ml of 1g/l DCM in DMSO solution. The pH of the resultant suspension was near 5. The suspension was then stirred at room temperature for more than 24 h and then centrifuged. The residue was washed at least twice with DMSO to remove the DCM from the external surface and then dried at 80 ^oC.

2.2.4 Instrumentation

Absorption spectra were recorded using a Perkin-Elmer, Lambda 18, UV-Vis-NIR spectrometer. Steady-state fluorescence spectra were acquired using a SPEX Fluorolog-ι2 spectrofluorometer. The X-ray diffraction (XRD) instrument used was a Rigaku diffractometer using Cu $K_{\alpha 1}$ (0.154nm) X-rays: typically run at a voltage of 40 kV and current of 30mA. For fluorescence decay measurements, the sample was excited at 480 nm with pulses of ca. 1 ps duration at a repetition rate of 1 KHz, provided by an all-solid state Spectra-Physics laser system, consisting of a Spectra Physics OPA 800 pumped by a Spitfire regenerative amplifier, which in turn was pumped by Merlin and seeded by a Millennia pumped Tsunami laser. The emission was detected by a Hamamatsu streak camera, model C4334. The temporal dynamics of the emission was analyzed using fluorescence lifetime software (HPD-TA 32) provided by Hamamatsu.

2.3 Results

XRD patterns of pristine, uncalcined MCM-41, modified MCM-41, and the DCM/MCM-41 composite are shown in Figure 2-5. Using Bragg's equation and comparison with reference studies, the pore size of uncalcined MCM-41 is estimated to be ca. 33 Å. Additionally, we find, upon attachment of the (putative) monolayer of silylation product to the internal channels of the calcined MCM-41, the peak at index (100) shifts to higher angle, with the pore size estimated to be ca. 25 Å. This latter size is sufficiently large to allow DCM, of approximate dimensions (8 × 16) $Å^2$, to be incorporated into the modified MCM-41. The XRD pattern of DCM/MCM-41 shows a strong (100) peak, suggesting framework stability is maintained for the modified MCM-41 when DCM is incorporated.

Y zeolite has a tridirectional geometry encompassing almost spherical cavities (of ca. 13 Å diameter) interconnected through four tetrahedrally arranged portals of ca. 8 Å diameter [23]. Although DCM can be accommodated inside the cavities of Y zeolite, the shape and the orientation of DCM are expected to be severely restricted. Such confinement will tend to decrease photophysical relaxation rates for the dye in the host [24], since ultrafast ICT reactions are facilitated when the configuration of the excited structure promotes an orbital interaction between donor and acceptor, as occurs, generally, when the excited state leads to molecular planarity.

Diffuse reflectance (DR) UV-vis spectra of DCM/MCM-41 and DCM/Y-zeolite samples are shown in Figure 2-6. Also included in this figure, for comparison, is the transmission UV-vis spectrum of DCM in highly polar DMSO solution. For

DCM/MCM-41 composites with different Si/Al ratio, the absorption spectrum does not change much. For the DCM/MCM-41 composite, DCM exhibits a broad absorption spectrum that is suggestive that at least three peaks exists (located at 365, 411 and 472 nm) instead of a single peak at 480 nm found for the dye dissolved in DMSO. The broad absorption is attributed to "site specific effects" [25], resulting from ground state DCM molecules being distributed within the channels of MCM-41 and experiencing, as a result, a range of perturbations. The interactions that are most likely of major influence in determining the blue shifted, broad absorption structure derive from the molecular resonance structures of DCM, where one finds that a greater density of electrons is expected to occur at the cyano group, and this charge is expected to result in stronger interactions between the cyano groups and the interior wall of the modified MCM-41, helping to anchor DCM within the pore, moreover, the positive charge on the dimethylamino group would be expected to result in neighboring DCM molecules in the cavity repelling one another, favoring a twisted structural character for DCM, which would militate ICT processes again. The diffuse reflectance spectrum of Y zeolite (in Figure 2-6), on the other hand, reveals only a small amount of blue-shifting (from the absorption maximum in DMSO) and a minor change in band width. We attribute this to the spatial dimensions of the Y zeolite supercages, which allow only a single DCM molecule to be encapsulated, resulting in an absence of a "site specific effect." Additionally, the small blue-shift that is evidenced can be attributed to the presence of twisted single DCM molecules within the supercages.

Figure 2-7 presents our principal fluorescence findings for the DCM system. As shown, for excitation using 480 nm radiation, the composite system DCM/MCM-41

shows an emission that possesses peaks at 555 and 585 nm, while the DCM/Y-zeolite composite evinces one band with peak position almost coincident with the 585 nm peak of DCM/MCM-41. We assign this latter peak to emission from an emitting TICT state for the following reasons. Firstly, it is well known that the photophysics of trapped molecules in matrices may depend on several parameters, and for the system examined here, the spatial constriction of the cavity would be expected to result in motional restriction for excited DCM guest molecules, which would trigger fast internal conversion relaxation processes and impart some ICT character to the resultant state for DCM in both MCM-41 and Y zeolite. Secondly, environmental polarity can dramatically affect optical properties of a confined dye, and an increase in polarity often leads to the formation of a red shifted TICT excited state and a resulting thermally driven enhanced TICT emission [17,26-28,31]. For our system, the polarity of MCM-41 lies between those of dichloromethane and 2-propanol, while Y-zeolite has a greater polarity than acetonitrile [28,29]. These relative values indicate that the polarity of Y-zeolite is greater than that of MCM-41, which rationalizes the red shift in the emission that is shown in Figure 2-7 when the host changes from MCM-41 to Y-zeolite. Moreover, DMSO has a greater polarity than both of the solid hosts, and, accordingly, the red shift is even larger in this solvent. It is also to be noted, for comparison with the literature, that MCM-41 has a greater polarity than n-heptane, which has been used in ICT studies involving DCM [16], and it is not unreasonable that the emission intensity of DCM might be higher for our system involving MCM-41 (given the greater environmental polarity) than that observed for the n-heptane system.

As regards the difference between the shapes of the emission from the MCM-41 and Y-zeolite systems, it is to be noted that the Y zeolite cavity is significantly more polar than that of MCM-41 [28,29], resulting in a lower activation energy between the LE and ICT states than expected in the case of MCM-41. Consequently, a faster ICT process for the Y-zeolite composite may result in a decrease in the number of emitting states—in the present case to a single emission as compared to what happens for MCM-41 (see Figure 2-7, spectrum c). Hence, the emission band at 585 nm is attributed to the emission from the excited ICT state resulting from relaxation of the initial formed LE state, while the emission band at 555 nm is attributable to a transition from the locally excited (LE) state.

Fluorescence spectra of the DCM/MCM-41 composite at three excitation wavelengths were acquired. The aim in this case was to determine whether the broad absorption spectrum in Figure 2-8 pertains to absorption by the same species, albeit distributed amongst different sites within MCM-41. Figure 2-8 shows spectra resulting from excitation at 360, 440, and 480 nm that fall near three peak absorption regions evidenced in Figure 2-7. The resulting emissions are all quite similar, and are suggestive of the existence of two overlapping emission bands (see below). Hence, we can conclude that the emissions derive from a common species. For DCM in Y-zeolite and dissolved in DMSO, we also acquired emission spectra using different excitation wavelengths. In both cases, only one emission band occurred.

Fluorescence decay curves, using 480 excitation, were also measured for DCM in various environments, as shown in Figure 2-9 for 480 nm exciting radiation. For DCM in DMSO, the emission decay in Figure 2-9 fits a single exponential function with time

constant of 2.0 ± 0.1 ns, where the ± error was assessed by changing the spectral window used by the Hamamatsu streak-camera software—in selecting and fitting data to exponential decays—and determining the ranges of the calculated decays that results from varying the spectral window; this same approach was used for all indicated error assignments. For DCM in Y zeolite, the decay also is monoexponential, but of shorter lifetime, 1.3 ± 0.1 ns. The shortening of the lifetime for the DCM/Y-zeolite system, of course, can be attributed to interactions of DCM and Y-zeolite, which open nonradiative deactivation channels for decay. In particular, as a result of ionic bonding at the internal surface, energy transfer between the DCM molecules and Y-zeolite can occur, which introduces an additional pathway for depopulating the ICT state [30]; also electronic confinement, which leads to mixing of the HOMO and LUMO, can occur, with resultant enhanced nonradiative relaxations rates [31]. The emission decay for DCM in MCM-41 (see Figure 2-9), while being shortened, however appears biexponential, independent of whether the fluorescence dynamics is monitored at 555 or 585 nm. The biexponential character is attributed to the capturing of photons from the overlapping wings of the two unresolved bands. Hence, both bands, as expected, have essentially the same values for the two relaxation times, although with possibly different amplitude factors. For the 555 nm peak the fast component is found to have a decay lifetime (Figure 2-10) (percent contribution) of ca. 0.6 ns (57%), while the slower component has a decay lifetime (percent contribution) of ca. 1.8 ns (43%), resulting in an average decay time ($<\tau>=a_1\tau_1+a_2\tau_2$) of ca. 1.1 ns; the 585 nm peak gives the same decay constants and only slightly different amplitude factors. It is to be noted that the relative percentage for the contributions also are in agreement with the relative

intensity of the two deconvoluted bands as found from the steady state emission spectrum (Figure 2-10).

We attribute the slow component to emission from a stabilized TICT state and the faster component to normal emission from the LE state. The relative amplitude of TICT emission is determined by the polarity of the MCM-41. Since the difference between the electronic energy levels of LE and TICT states is not large, the two states may co-exist in environments of moderate polarity [32]. For the DMSO solution system, where a twisting motion is expected to result in the formation of a TICT state, we observed only one decay component (with lifetime of 2.0 ± 0.1 ns), consistent with the existence of an ultrafast relaxation from the LE state to a TICT state [10].

2.5 Conclusion

The present work shows that DCM can be successfully occluded within the pores of MCM-41 and Y-zeolite. From UV-Vis absorption and fluorescence measurements, DCM is found to exhibit different photophysics for MCM-41 and Y-zeolite mesoporous materials. For the composite consisting of DCM and MCM-41, ICT processes are found to be sufficiently reduced that a dual emission (attributed to emissions from the LE and ICT states) is observed. In this case, the optical decay leads to the assignment of lifetimes of 0.6 ± 0.1 ns for the LE state and 1.9 ± 0.1 ns for the TICT state. In the case of the Y-zeolite composite, only one emission (of decay lifetime 1.3 ± 0.1 ns) is found, which is rationalized in terms of the dimension of the supercages and the high polarity of the materials surface.

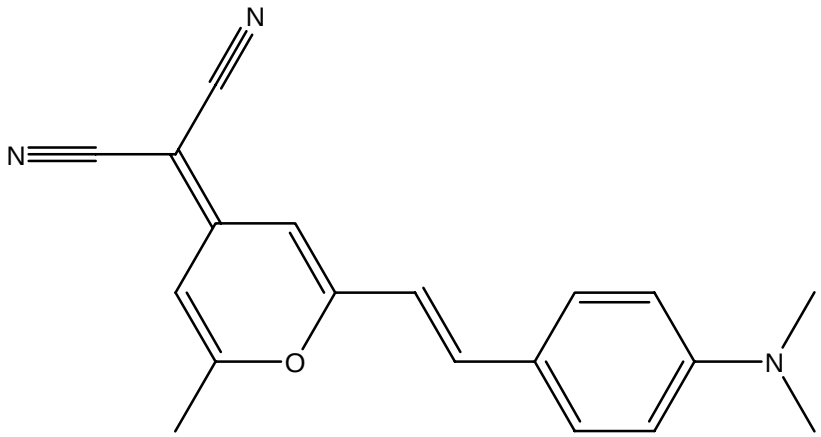

Figure 2-1: The structure of DCM.

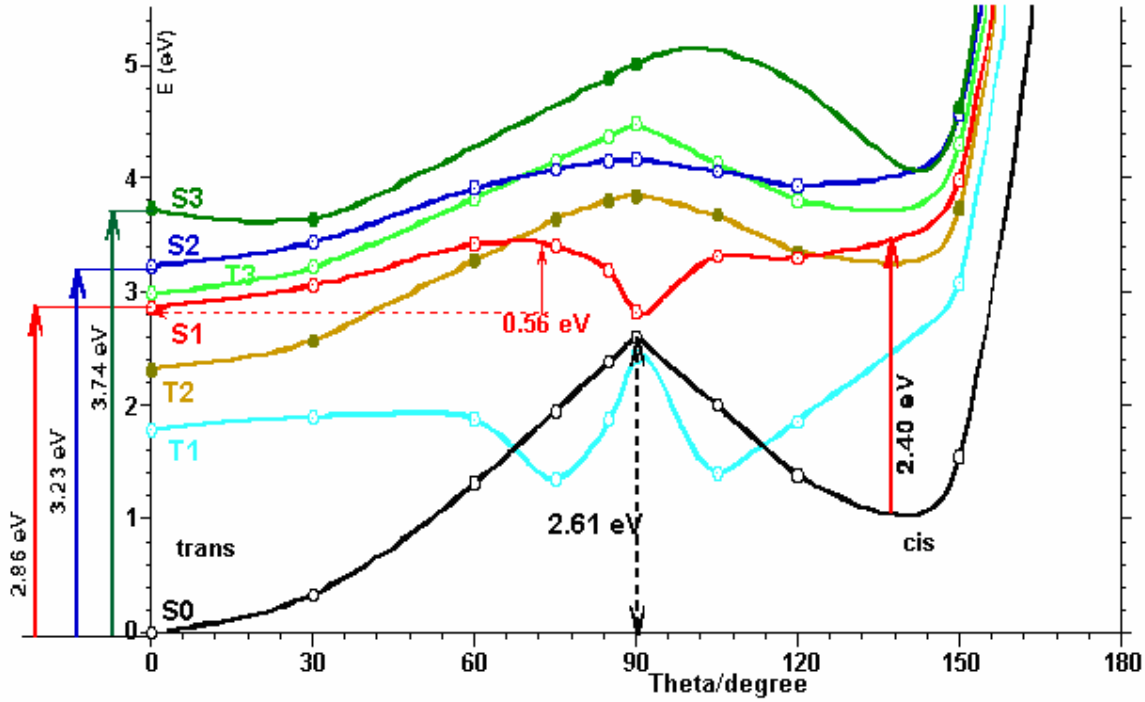

Figure 2-2 The predicted PESs of DCM as function of rotation from trans to cis configuration.

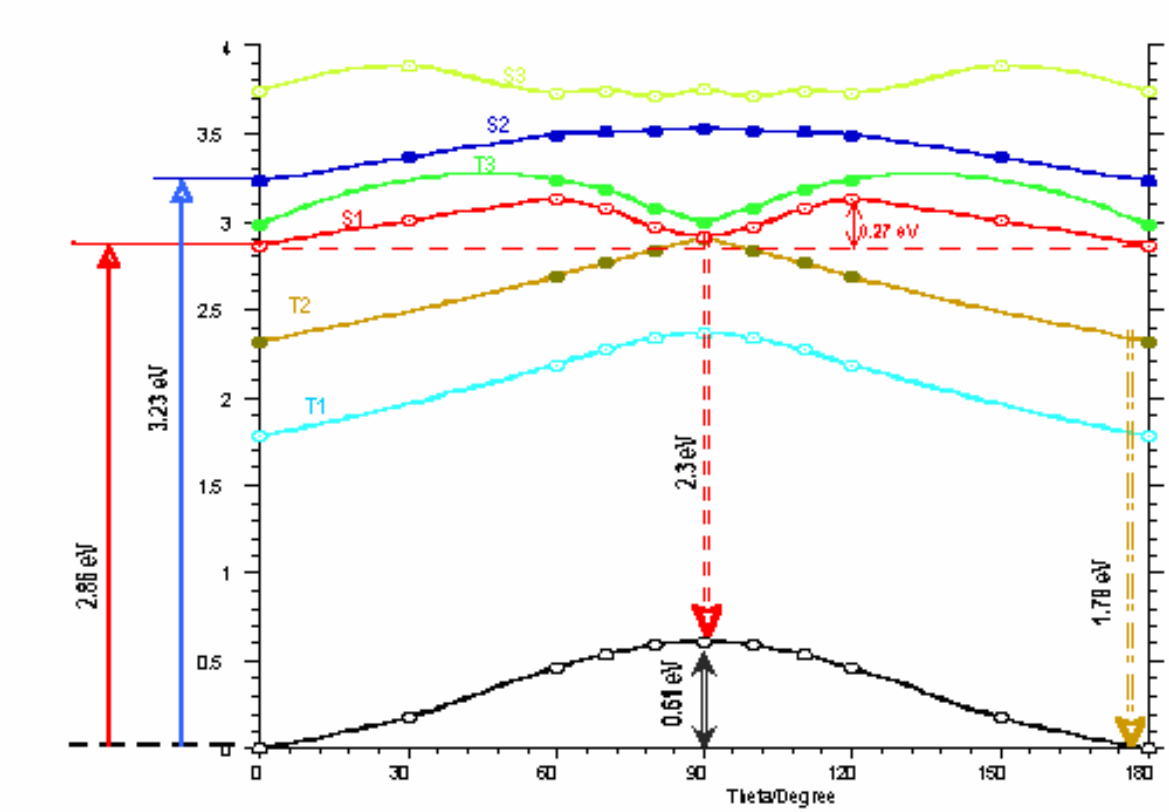

Figure 2-3 PESs of DCM as function of rotation of the donor group from 0 to 180 degree.

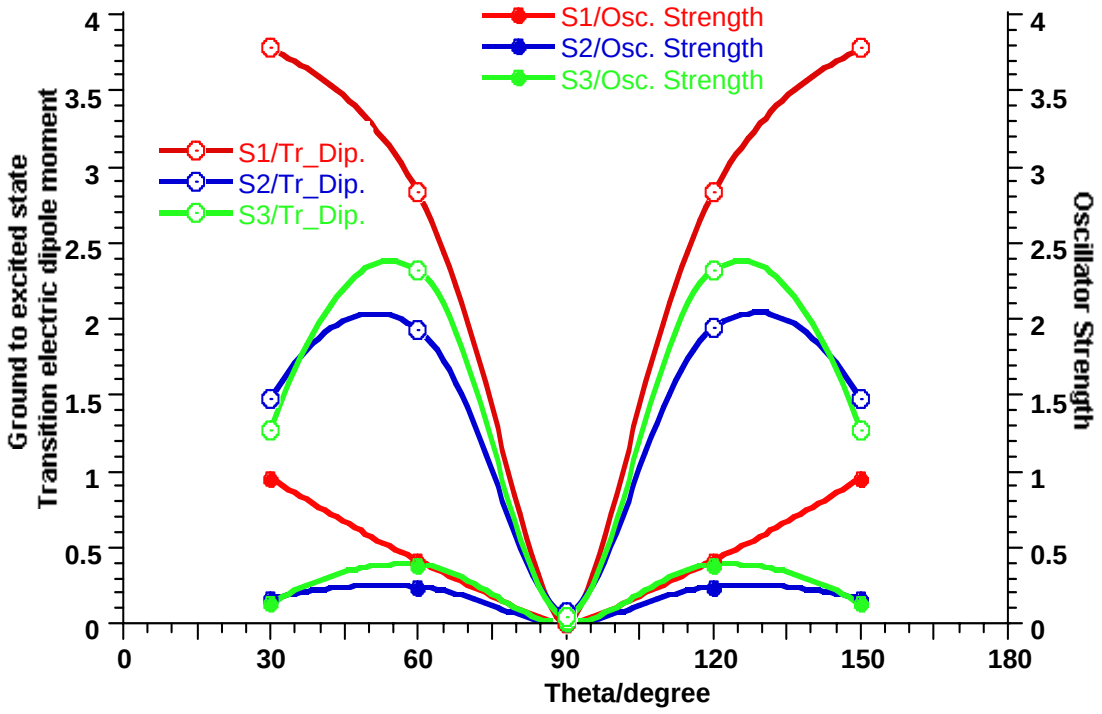

Figure 2-4 Ground to excited state Transition electric dipole moment as a function of rotation of the acceptor from 0 to 180 degree.

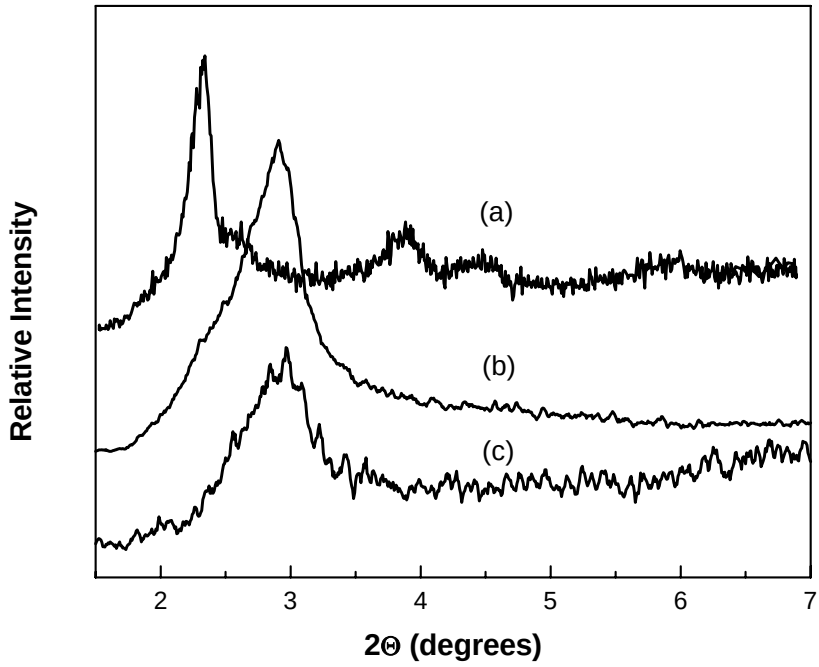

Figure 2-5: XRD patterns of pristine (a) uncalcined MCM-41, (b) modified MCM-41 and (c) the DCM/MCM-41 composite.

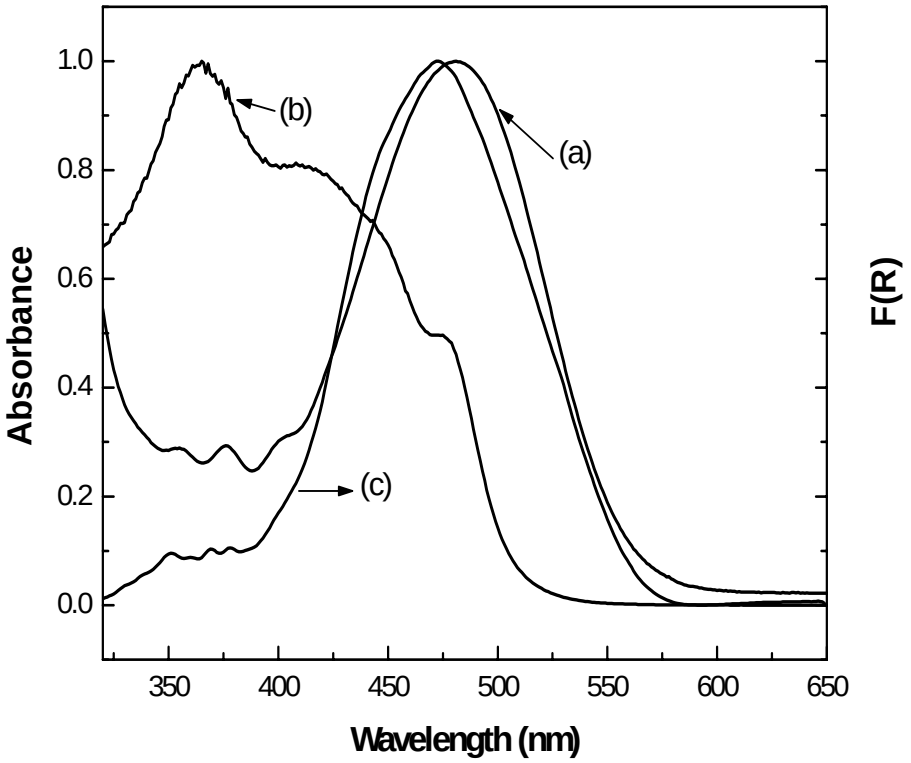

Figure 2-6: UV-vis spectrum of (a) 5×10^{-5} M DCM dissolved in DMSO; Diffuse UV-vis spectrum of (b) DCM/ MCM-41 and (c) DCM/Y-zeolite.

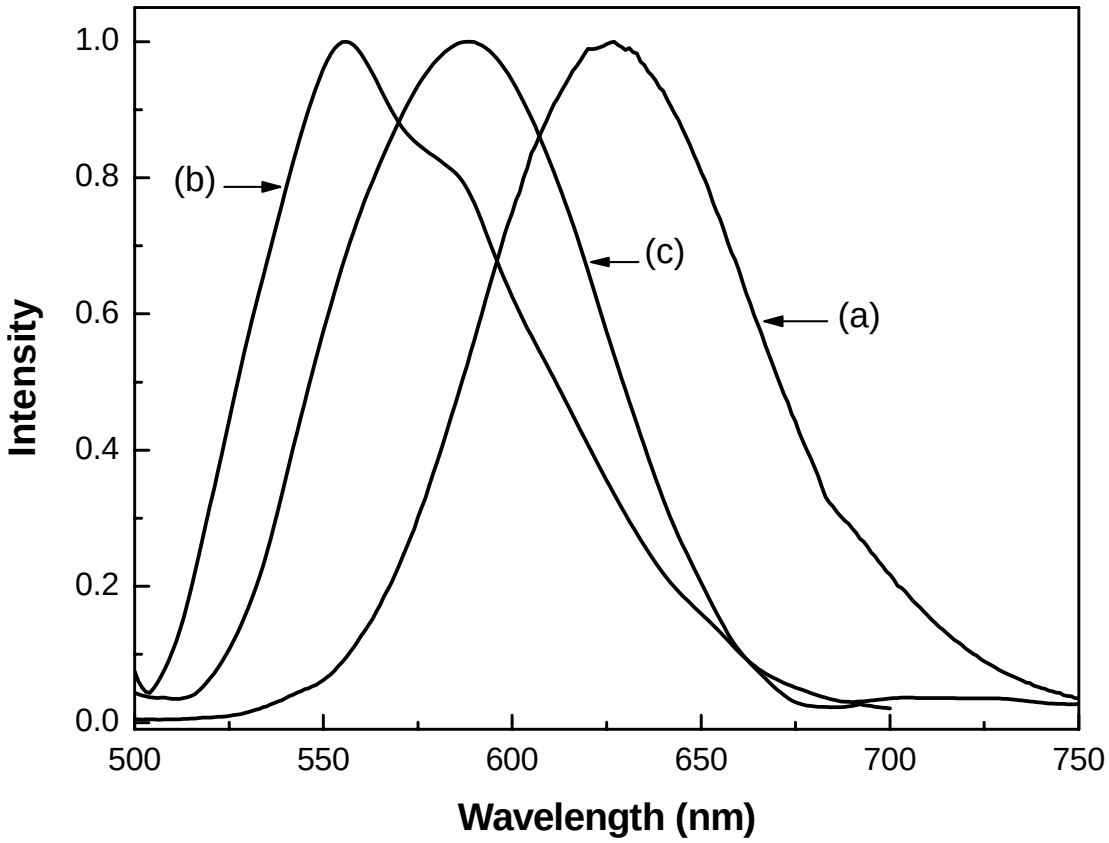

Figure 2-7: Fluorescence spectra of (a) 5×10^{-5} M DCM dissolved in DMSO, (b) DCM/ MCM-41 and (c) DCM/Y-zeolite.

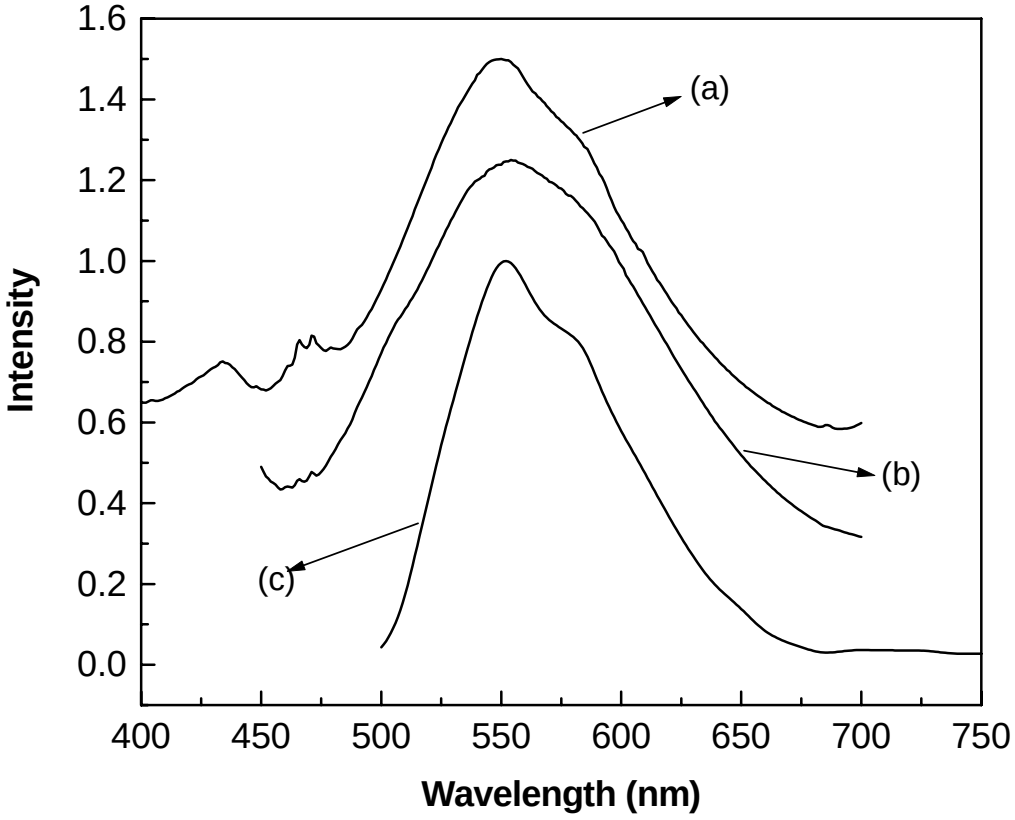

Figure 2-8: Fluorescence of DCM/MCM-41 composite, using a SPEX Fluorolog-τ2 spectrofluorometer. Excitation wavelength (a) 360 nm, (b) 440 nm, and (c) 480 nm.

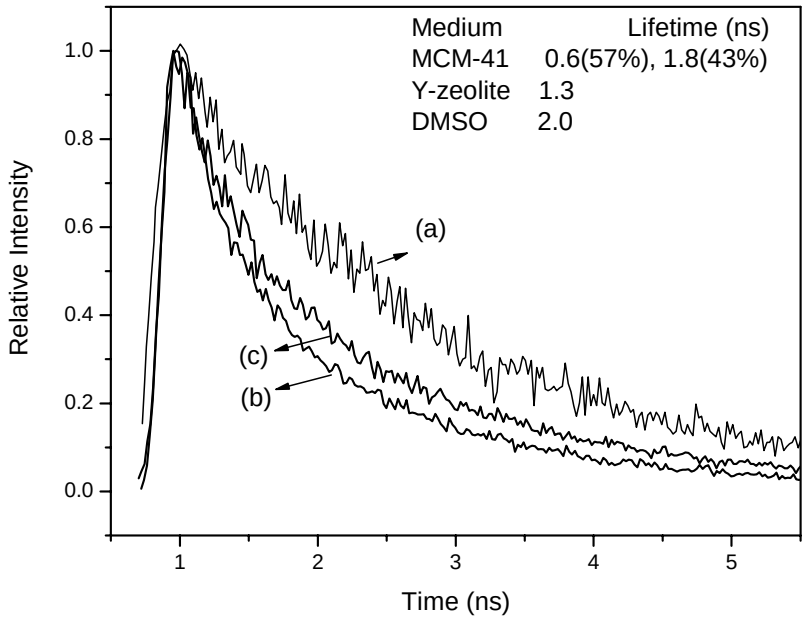

Figure 2-9: Lifetime decay curves of (a) 5×10^{-5} M DCM dissolved in DMSO; (b) DCM/MCM-41 and (c) DCM/Y-zeolite.(λex=480nm)

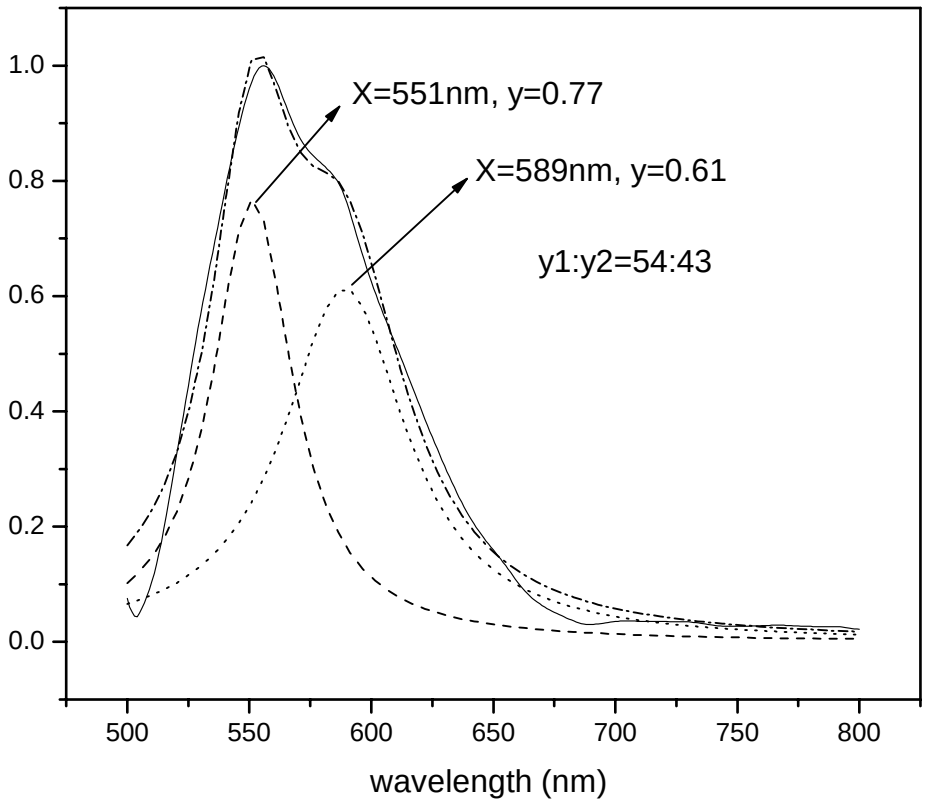

Figure 2-10: Deconvolution of the emission bands.

Chapter 3 Magnetic Ordering of Ferric Oxide within Mesoporous Materials

Currently, there is a great desire to prepare well-defined, discrete magnetic nanoparticles for both fundamental and societal benefits. These nano-sized magnetic materials display properties that differ from their respective bulk material counterparts due to the differences in size and surface effects. A major hurdle to understanding the relationship between structure and magnetic behavior is the availability of magnetic nanoparticles with well-defined structural features.

3.1 Introduction to magnetism

3.1.1 Origin of magnetism

Magnetism originates from the movement of electric charges. All materials display some magnetic response, however most effects are very small. The electrons in an atom govern magnetic properties of matter in two different ways. The first is the electron acting as a spinning charged sphere, where the spin resembles the magnetic field of a tiny bar magnet. The second is the effect of the electron circulating around the nucleus of the atom, which resembles a current loop. The flow of charge in a circular current loop produces magnetic lines of force known as a dipole. An electron in an atom has a magnetic moment due to its spin or spin and orbital motion.

3.1.2 Magnetization terms

The quantities of magnetism are defined by fundamental concepts of magnetic dipoles consisting of equal and opposite moments. Free currents generate fields

classified in terms of magnetic field strength or intensity (H). The magnetic induction (B) is a function of H and the magnetization or polarization (M).

$$B = H + 4\pi M$$

The magnetization (M) can be understood as the density of net magnetic dipole moments (μ) in a material.

$$M = \frac{\mu_{total}}{V}$$

The magnetic susceptibility (κ) is a measure of the effectiveness of an applied magnetic field for inducing a magnetic dipole in the material. Magnetic permeability (μ) is a ratio of the magnetic induction and magnetic field strength.

$$\kappa = \frac{M}{H} \qquad\qquad \mu = \frac{B}{H}$$

3.1.3 Magnetism in materials

Materials are classified by their response to an externally applied magnetic field. Descriptions of orientations of the magnetic moments in a material help to identify different forms of magnetism observed in nature (Figure 3-1). Five basic types of magnetism can be described: diamagnetism, paramagnetism, ferromagnetism, antiferromagnetism and ferrimagnetism.

In the presence of an externally applied magnetic field the atomic current loops created by the orbital motion of electrons respond to oppose the applied field. All materials display this type of weak repulsion to a magnetic field known as

diamagnetism. However, diamagnetism is very weak and therefore any other form of magnetic behavior that a material may possess usually over-powers the effects of the current loops. In terms of electronic configurations of materials, diamagnetism is observed in materials with filled electronic sub-shells where the magnetic moments are paired and overall cancel each other. Diamagnetic materials have a negative susceptibility ($x < 0$) and weakly repel an applied magnetic field. The effect of these atomic current loops are overcome if the material displays a net magnetic moment or has long-range ordering of magnetic moments.

All of the other types of magnetic behavior observed in materials are at least partially attributed to unpaired electrons in atomic shells, often in the 3d or 4f shells of each atom. Materials whose atomic magnetic moments are uncoupled display *paramagnetism.* Therefore, paramagnetic materials' moments have no long-range order. A generalized description of paramagnetism is when each atom carries a magnetic moment, which partially aligns in an applied magnetic field and hence enhances the magnetic flux density. The field acts independently on each atomic dipole. Hence, there is no long-range order and there is a small positive magnetic susceptibility ($x \sim 0$). Materials that possess *ferromagnetism* have aligned atomic magnetic moments of equal magnitude and their crystalline structure allows for direct coupling interactions between the moments which may strongly enhance the flux density. Furthermore, the aligned moments in ferromagnetic materials can confer a spontaneous magnetization in the absence of an applied magnetic field. Materials that retain permanent magnetization in the absence of an applied field are known as hard magnets.

Materials having atomic magnetic moments of equal magnitude arranged in an antiparallel fashion display antiferromagnetism. The exchange interaction couples the moments such that they are antiparallel hence leaving a zero net magnetization. Above the Néel temperature (T_N) thermal energy is sufficient to cause the equal and oppositely aligned atomic moments to randomly fluctuate leading to a disappearance of their long-range order. In this state the material exhibits paramagnetic behavior. Ferrimagnetism is similar to antiferromagnetism in that two different sub-lattices exist and antiferromagnetic exchange interactions occur. However, the magnitudes of the two different types of moments, arranged antiparallel, are not equal in magnitude and hence a net magnetization is produced.

3.1.4 Theory of ferromagnetism

Weiss first developed the molecular theory of ferromagnetism in the early 1900s, which sufficed as a semi-quantitative description. The theory is based on the assumption that each atomic dipole is subject to a local field that is proportional to the magnetization summed over all the other dipoles in the material. Later, the development of quantum mechanics led to the concept of exchange interactions between two atoms and spin-dependent Coulombic interactions. The spin exchange interaction is derived from the Pauli exclusion principle, where antiparallel spin arrangements in an atomic shell are forbidden. The exchange interaction is essentially the difference in Coulombic energies for different spin configurations in a sample. Above a certain temperature, known as the Curie temperature (T_C), the alignment of the moments in ferromagnetic and ferrimagnetic materials is lost due to thermal energy and

the material displays paramagnetic behavior.

3.2 Background

Recently, much effort has been devoted to the synthesis of various magnetic nanoparticles due to their peculiar optical and magnetic properties [1]. Among magnetic materials, Fe2O3 is technologically important with wide functionality in the semiconductor, pigment, magnetic storage, magneto-optical, nonlinear optical, catalyst and gas-sensor arenas [2-4]. Of late, enhanced interest has been directed at nanostructural Fe_2O_3 because of unique changes in electronic and optoelectronic properties of the nanomaterials from that of bulk Fe_2O_3—as a result of both quantum confinement and the greater influence of surface states [2].

Approaches for synthesis of nanostructural Fe_2O_3 have been varied. Numerous compositions and morphologies have been obtained by oxyhydrogen flame pyrolysis, electrochemical synthesis, sol-gel processes, and chemical oxidation in micellar, polymeric media or mineral matrices [5,6]. More recently, research efforts have aimed to encapsulate Fe_2O_3 within mesoporous materials, e.g., MCM-41 and SBA-15. These silica-based mesoporous materials have regular one-dimensional (1-D) pores that are hexagonally arrayed, and the diameters of the channels can be largely controlled through the use of surfactants of different chain lengths, which participate in pore formation through steps involving aligned micellar rods. Due to their unique structures, mesoporous materials have been used as "molecule factories" in which a 3-D dispersion of guests could be supported. This is important for magnetic nanoparticles because the particle size is confined and particles are isolated from each other.

In the present paper, we discuss in detail the effect of pore size and morphology of the mesoporous materials on microwave absorption abilities of the nanocomposites. Four SiO_2 based mesoporous hosts with different pore sizes and morphologies have been synthesized and characterized. The four host materials are labeled as C8-MCM-41, C16-MCM-41, SBA-15 and MCM-48; the first two corresponding to MCM-41 formed using surfactants with chain lengths involving 8 and 16 carbons atoms, respectively, and SBA-15 is a kind of the well known mesoporous material with hexagonally arranged hexagonal pores. Different from the structures of MCM-41 and SBA-15 with hexagonal 1-D channels, the structure of MCM-48 has a cubic pore system which consists of two independent and intricately interwoven networks of mesoporous channels (Fig. 3-2).

EPR and Q factor measurements for the nanocomposites indicate that the pore size affects microwave absorption strength at zero field strength. We have found that the microwave absorption ability increases with decrease of the pore size. The morphology the the host has little effect on the magnetic behavior of Fe_2O_3 loaded. The convenient synthesis method along with the unique magnetic properties of the composites suggests potential use as a microwave absorbing material.

3.3. Experimental

3.3.1. Synthesis of mesoporous materials

C8-MCM-41 was synthesized by using octyltrimethyl ammonium bromide as the template [7]. Briefly, 5.3 g octyltrimethyl ammonium bromide (OTAB) was dissolved

in 36.5 ml H_2O. 1.8 ml 5M NaOH aqueous solution was added to the OTAB solution, and, after stirring for half an hour, 5 ml tetramethyl orthosilicate (TMOS) was added. The mixture was then stirred for another one hour, followed by heating in a Teflon-lined autoclave at 373 K for five days. The resultant precipitate was filtered and washed thoroughly with distilled water.

For C16-MCM-41, cetyltrimethyl ammonium bromide (CTAB) was chosen as template. Briefly, C16-MCM-41 was synthesized according to the molar composition ratio SiO_2:0.085 Na_2O:0.16 CTAB:63 H_2O [8, 9]. Steps involved dissolving ca. 2.4 g of CTAB in 40 ml distilled water, followed by addition of 6.5 ml of 1.1 M NaOH. After stirring for half an hour, 6.3 ml TMOS was added and the mixture stirred for another one hour, then heated in a Teflon-lined autoclave at 373 K for 24 hours. The resultant precipitate was filtered and washed thoroughly with distilled water.

SBA-15 was prepared by using a triblock copolymer as the template. Specifically, 4 g of poly(ethylene oxide)-poly(propylene oxide)-poly(ethylene oxide), i.e., $EO_{20}PO_{70}EO_{20}$, also referred to as Pluronic 123 (Aldrich), was mixed with 9 ml TEOS and 120 ml of 2 M HCl. The mixture was stirred for 2 hours; then allowed to react at 308 K for 20 hours, followed by heating the mixture at 373 K for two days. The product was then filtered and washed using distilled water [10].

MCM-48 was prepapred by using hexadecyltrimethylammonium bromide (HTABr) as the surfactant. In a typical synthesis batch, HTABr (Aldrich) was dissolved in a mixture of distilled water and ethanol to give the resulting molar composition of 1.0 HTABr : 5.0 EtOH : 120 H_2O. The TEOS was added to this surfactant solution at room

temperature, dropwise with vigorous magnetic stirring. The resulting gel mixture, with a molar composition of 1.4 SiO_2 : 1.0 HTABr: 0.35 Na_2O: 5.0EtOH : 140H_2O, was heated for 4 days at 373 K in an autoclave and subsequently cooled to 340 K. The product was then filtered and washed using distilled water.

3.3.2. Modification of mesoporous materials

In a typical process, 1 g of the as-prepared mesoporous material had its surface passivated by suspension of the material (for 6 ~ 10 h at room temperature) in a solution of 2 ml $C_6H_5Si(OCH_3)_3$ in 25 ml chloroform. After surface passivation the organic template was extracted using ethanol, then the internal surface of the residual sample was modified (to rigidify the structure) by suspending the material in 5 ml of 3-(2-aminoethylamino)propyltrimethoxysilane (APTMS) in 50 ml toluene for 12 hours; the final modified mesoporous material was filtered and washed using ethanol [11-13].

3.3.3. Formation of ferric oxide encapsulated within mesoporous materials

0.25 g of the modified mesoporous material was mixed with ca. 50 ml of 0.1 M ethanolic $Fe(NO_3)_3 \cdot 9H_2O$. The mixtures were vigorously stirred and evaporated at 80 ^oC to remove ethanol; the net effect is to enhance the amount of Fe_2O_3 formed within the channels of the mesoporous materials. The dark brownish sample was then washed several times and heated at 180 ^oC for 24 h. To obtain different amounts of iron (III) oxide inside the mesopores of MCM-41, various volumes of 0.1 M ethanolic $Fe(NO_3)_3$ solutions were applied.

3.3.4. Instruments

Absorption spectra were recorded using a Perkin-Elmer, Lambda 18, UV-vis-NIR spectrometer. The X-ray diffraction (XRD) instrument was a Rigaku diffractometer using Cu $K_{\alpha 1}$ (0.154 nm) X-rays and typically was run at a voltage of 40 kV and current of 30 mA. IR spectra were taken on Thermo Nicolet Auntar 360 FTIR. The EPR spectra were recorded with a Bruker ESO380E spectrometer operating at the X-band and equipped with a HIP 5361 frequency counter; spectra at room temperature were obtained under the following settings: microwave power, ~0.7 mW; modulation amplitude, 10.45 G; modulation frequency, 100 KHz; time constant, 1.28 ms; sweep period, up to 168 s; sweep width, 7000 G; and the X axis resolution, 4 K. Transmission electron microscope images were acquired using powered samples that were dry loaded onto Cu grids with holey carbon films, and utilized a Tecnai F 20 TEM operated at 200 KV for bright field images; also the stability of the MCM-41 samples was checked by both a JEOL 4000 EX microscope operated at 400 KV and a Topcon 002B microscope operated at 200 KV.

3.4 Results and Discussion

X-ray diffraction patterns for uncalcined, functionalized, and Fe_2O_3 loaded C8-MCM-41, C16-MCM-41, and SBA-15 are provided in Figure 3-3. For the system C8-MCM-41 one finds only one peak, which indexes with (100). For C16-MCM-41 and SBA-15, at least three indexable peaks are found, i.e., (100), (110) and (200), with their (100) peak much sharper than that observed for C8-MCM-41. The patterns shown in Figure 3-3 indicate that C16-MCM-41 and SBA-15 have more highly organized

channels than does C8-MCM-41; however, it is well known that the low-molecular-weight surfactants are difficult to self-organize and, hence, give less ordered materials.

One notes from the X-ray diffraction results that after passivation, the external surface and internally modified structures of the molecular sieve materials retained their organizations. From the Bragg relationship, the d-spacing (indicated by the location of the (100) peak) for each matrix was determined. The d_{100} spacing of functionalized C8-MCM-41 is found to be ca. 28 Å; for functionalized C16-MCM-41, the d_{100} spacing is close to 33 Å; while for functionalized SBA-15, the d_{100} spacing is ca. 82 Å. However, after encapsulation of Fe_2O_3, the (100) peak intensities of the three mesoporous materials decreased significantly, especially for C8-MCM-41 and C16-MCM-41, which is attributable to distortion of the mesoporous pores caused by the high-loading of Fe_2O_3. The α phase of Fe_2O_3, for the three composites, is judged to be present from large angle X-ray diffraction spectra (see insets of Figure 3-3; for comparison, see JCPDS CARDS 86-0550). The observed 2θ scattering angles of 33.2^o and 35.5^o correspond to the (104) and (110) peaks of α-Fe_2O_3, respectively. Additionally, as shown in Figure 3-4, the Raman spectra of the samples have five well-resolved vibrational peaks at ca. 219, 283, 396, 490 and 599 cm^{-1}, which, despite a small shift towards lower wavenumbers when compared to the bulk samples, correspond to the characteristic frequencies for α-Fe_2O_3. Furthermore, the absence of bands attributable to either γ-Fe_2O_3 (1370, 1580cm^{-1}) or Fe_3O_4 (670 cm^{-1}) indicates that the γ phase is not present [14-16].

Upon comparing XRD patterns of Fe_2O_3 in the different matrices, we ascertained that with pore size decrease (in the order SBA-15, C16-MCM-41, C8-MCM-41) the peak at ca. 35.5° becomes broader. This indicates that the average particle size of Fe_2O_3 in the matrix decreases as the pore size decreases. We deduce, therefore, that encapsulated particle size has been controlled by constricted growth within the cavities of the silicate mesoporous materials.

Figure 3-5 shows diffuse reflectance (DR), UV-vis spectra of the composites. The peak positions of the absorption bands for Fe_2O_3 nanocomposites encapsulated within C8-MCM-41, C16-MCM-41 and SBA-15 occur at 341 nm, 392 nm and 403 nm, respectively. All of the composite samples exhibit a blue shifted absorption bands when compared to the bulk Fe_2O_3, which has its absorption maximum at ca. 560 nm [17]. The large blue shifts are attributable to the existence of nanostructural Fe_2O_3, with the decrease of the pore size from SBA-15 to C8-MCM-41 guiding, successively, the formation of smaller Fe_2O_3 nanostructures. This result is consistent with the prediction from the XRD patterns. It is also worth noting that the SBA-15/Fe_2O_3 composite possesses an obvious shoulder band at ca. 530 nm, which likely indicates the presence of elongated structures.[1, 18]. This latter supposition is supported by TEM results provided below.

Infrared spectra of functionalized C16-MCM-41 and C16-MCM-41/Fe_2O_3 are provided in Figure 3-6. It is to be noted that IR spectra of the other samples are quite similar to those of C16-MCM-41 and C16-MCM-41/Fe_2O_3. Comparison of spectra before (A) and after (B) loading of Fe_2O_3, reveals that the IR bands at 1630, 1378, 790,

560 and 460 cm^{-1} are essentially unchanged upon occlusion of Fe_2O_3. These bands likely are associated with the external passivating agent and surface vibration of the mesoporous lattice. Other bands are found to shift, e.g., 1074 cm^{-1} to 1090 cm^{-1} and 976 cm^{-1} to 959 cm^{-1}, attributed to the Si-O-Si and the Si-OH groups, respectively. Still other bands exhibit lowered intensity upon formation of the composite, i.e., the 2854- and 2918-cm^{-1} bands, while bands at 1569, 1484, 1316, 1225, 698 and 666 cm^{-1} vanish. These latter bands are attributable to the stretching vibrations of C-H, Si-C, C-N, and the bending vibration for $–NH_2$, associated with the silylation compound APTMS (see above). These IR changes are interpreted as indicating that with the treatments discussed, Fe_2O_3 is incorporated in the mesoporous channels of MCM-41, resulting in constricted motion due to spatial confinement.

Transmission electron microscopy (TEM) provides further insight into the morphology and nanostructural details of the Fe_2O_3 composites. Ordered hexagonal arrays of the mesoporous framework of the as-prepared materials were confirmed by TEM. We ascertain from Figure 3-7 that Fe_2O_3 particles are densely distributed and packed within the channels of the mesoporous silicate materials. As a result of the high loading level of Fe_2O_3 nanoparticles, various sites in the matrix are found to be distorted or even destroyed. These finding are consistent with our deductions based on the XRD patterns. From the insets of Figure 3-7, one can conclude that a large number of nanocrystals are present throughout the sample. The average particle sizes of the Fe_2O_3 nanostructures within the matrices are 1-2 nm for Fe_2O_3/C8-MCM-41, 4-5 nm for Fe_2O_3/C16-MCM-41, and 8-9 nm for Fe_2O_3/SBA-15, respectively. These relative dimensions are consistent with the diameters of the channels of the as-prepared

mesoporous materials. Thus the particle size appears to be regulated by the mesoporous host pore diameter. In the lower inset of Figure 3-7C, the digital diffraction for Fe_2O_3 inside SBA-15 is shown. The lattice spacing is found to be ca. 0.27 nm, and the angle is around 60^o, which indicate the presence of the α phase of Fe_2O_3. Removal of the silica template for the SBA-15 composite, by addition of heated NaOH solution, results in free unsupported nanorod-like Fe_2O_3 nanostructures, with width ca. 12 nm and length up to ca. 75 nm, which are shown in Figure 3-7D.

As regards to the magnetic behavior of the as-prepared Fe_2O_3 nanocomposites, we carried out electron paramagnetic resonance (EPR) studies. Figure 3-8 provides room temperature first derivative EPR spectra for the three nanocomposite samples. Very broad EPR signals with g values of ca. 2.1 were observed for the three Fe_2O_3 nanocomposites. Moreover, the composite in which Fe_2O_3 is encapsulated within SBA-15 exhibits a small but distinct signal at $g \sim 4.3$, corresponding either to a strongly distorted rhombic site located on the surface of the encapsulated particle or to isolated iron (III) ions dispersed within the pores [19, 20]. Moreover, we find that the composites show strong absorption for a range of applied magnetic fields down to ~ 99 G, and even show a nonzero absorption when the field strength is extrapolated to zero. This non-zero absorption is neither found for the functionalized silicate mesoporous material nor for ferric oxide prepared by the same route but without the use of the mesoporous matrix material, indicating that the non-zero absorption likely results from some intrinsic level of alignment of the magnetic dipole moments within the pores. This intrinsic alignment most probably derives from strong dipole-dipole interactions (which vary inversely with particle size and shape) associated with the restricted size of

the pores and dense packing of a large quantity of Fe_2O_3 within pores. This conclusion is consistent with our observation of an increase in the g value of the absorption (near g ~2.1) with decrease in temperature, as shown in Figure 3-9 where an increase in the local field is attributable of a decrease in randomization with decrease in temperature.

In order to quantitate the microwave absorption, we determined the microwave absorption quality factor (Q) for each sample at 99 G (see Table 3-1):

$$Q = \frac{2\pi \quad (\text{Energy stored})}{\text{Energy dissipated per cycle}} \qquad 3\text{-}1$$

In the above equation, Q represents the efficiency of the cavity for storage of microwave energy, and indicates that upon comparing two materials, the one with the smaller Q factor generally absorbs microwave energy more strongly. As shown in Table 3-1, the Q factors of Fe_2O_3 in the three composites are substantially lower than that for a blank tube, indicating that the Fe_2O_3 nanocomposites have strong microwave absorption capacities. We note that, based on Q factor the composite Fe_2O_3/C8-MCM-41 has the strongest microwave absorption ability among the three samples; the Q factor for Fe_2O_3/C8-MCM-41 is found to be 1800, nearly 50% lower than that of the blank tube.

Such intrinsic alignment from strong dipole-dipole interactions was also found in the sample of Fe_2O_3 encapsulated within MCM-48. TEM images of the as-prepared composites with different Fe_2O_3 loading level are shown in Figure 3-10. For the high load Fe_2O_3 sample, one finds that the matrix is destroyed, but the particle size is quite uniform; the particle within the matrix has a diameter of is ca. 4-5 nm. Considering the

pore size of the MCM-48 matrix, it appears that the particle size of Fe_2O_3 is controlled by the pore size.

Similar to the result of Fe_2O_3 in MCM-41 and SBA-15, the EPR experiments (Figure 3-11) show that two distinct EPR signals of g value ~2.09 and ~4.3 are observed for Fe_2O_3 nanocomposites. It is noted that only the composites with Fe_2O_3 loading also show significant absorption at magnetic field of ~ 99 G and extrapolated nonzero absorption at zero field. Moreover, the microwave absorption were found to be 2000, which is similar to the ability in MCM-41. Thus, Fe_2O_3 encapsulated in MCM-48 was demonstrated to show strong microwave absorption ability in the absence of an external magnetic field.

The above deduction is also supported by the temperature dependence of the reciprocal of the integrated EPR signal, as shown in Figure 3-12. Generally, as expressed by the Curie-Weiss law, the EPR signal amplitude is inversely proportional to the absolute temperature, but not for the high load composite of Fe_2O_3 in MCM-48 matrix. As a consequence of such observations, we deduce that the morphology of the matrix will not affect the magnetic properties of ferric oxide loaded. It should be resulted form the dipole-dipole interaction between the nanoparticles, and this will be discussed in the next chapter.

4. Conclusion

A range of experimental measurement, including UV-vis, IR, TEM, EPR and X-ray diffraction, confirm that aligned magnetic Fe_2O_3 nanoparticles are formed within

the pores of selected mesoporous materials (C8-MCM-41, C16-MCM-41, SBA-15 and MCM-48). The pore dimension of the matrix is found to play a crucial role in the magnetic properties of the resultant nanocomposite. EPR measurements indicate that with sufficient loading of Fe_2O_3 the composite material exhibits nonzero absorption at zero magnetic field. Also, the composites show substantial microwave absorption capability even at moderate applied magnetic fields. This microwave absorption ability is attributed by us to the restricted size of the pores of the mesoporous materials and dense packing effects leading to aligned magnetic moments of nanostructual Fe_2O_3.

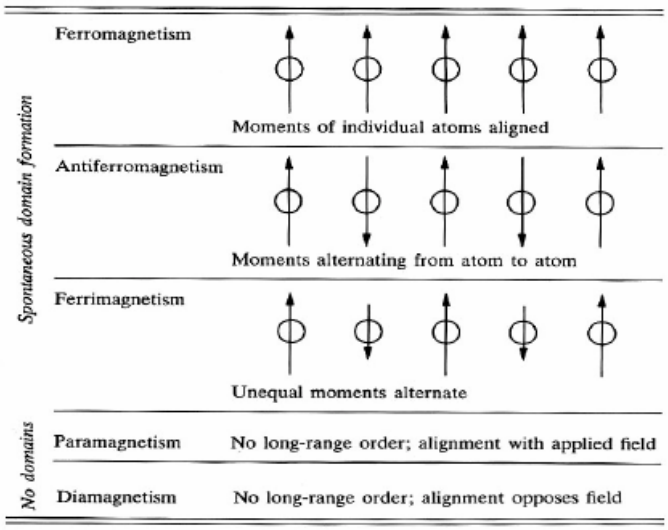

Figure 3-1 The different types of magnetic behavior.

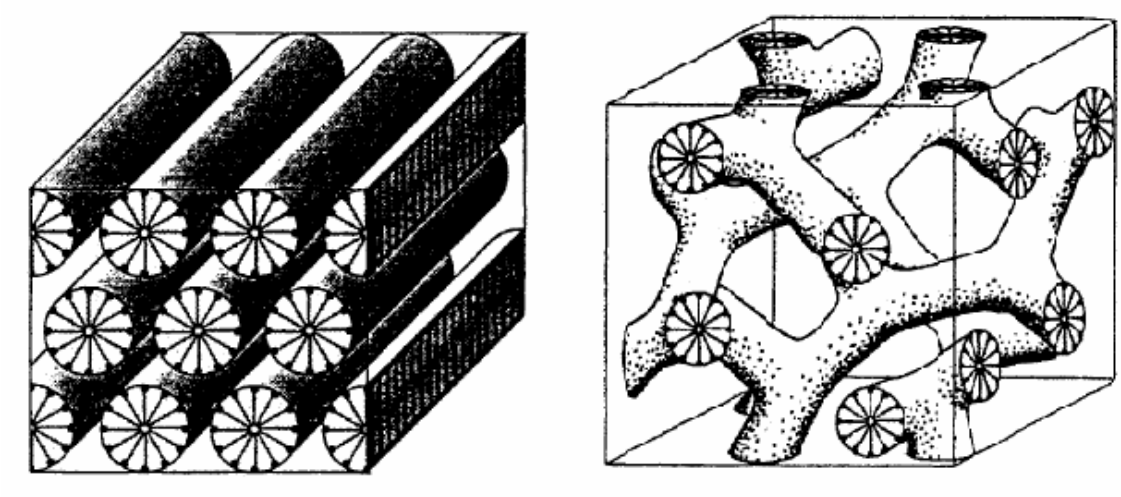

Figure 3-2 Structure of MCM-41 (left) and MCM-48 (right).

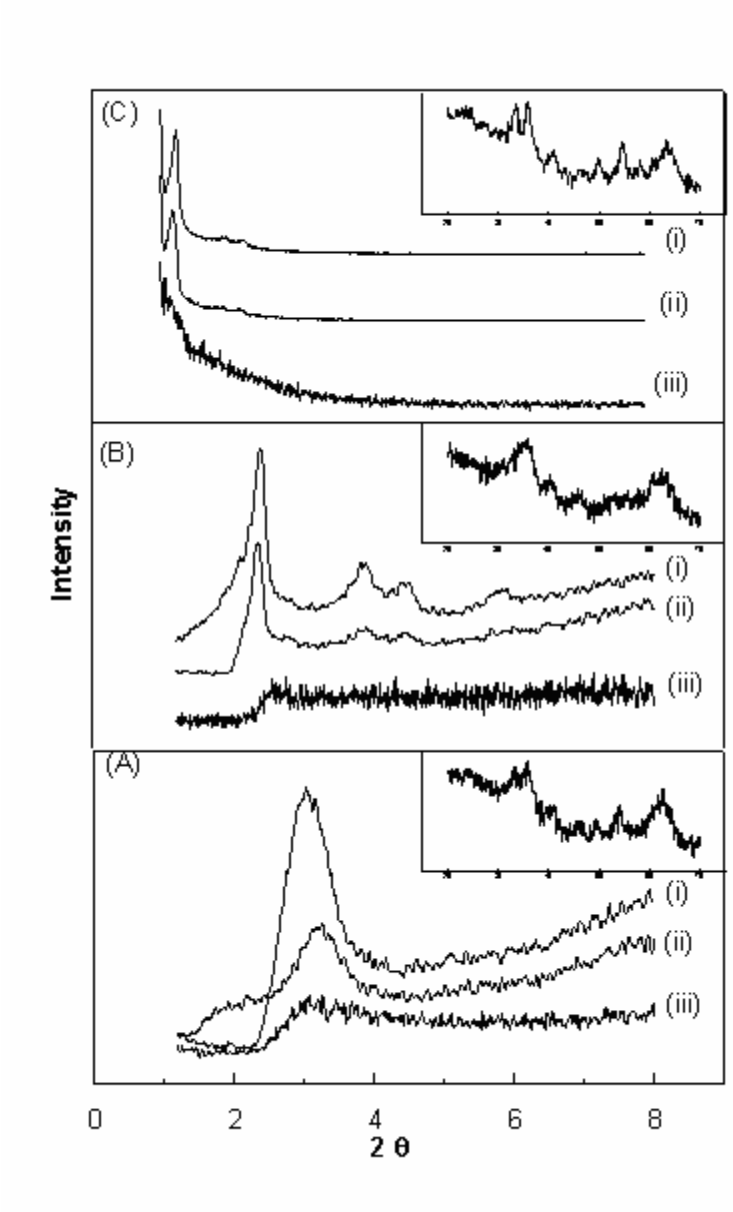

Figure 3-3 (A) XRD of (i) uncalcined, (ii) functionalized C8-MCM-41 and (iii) C8-MCM-41/Fe_2O_3; (B) XRD of (i) uncalcined, (ii) functionalized C16-MCM-41 and (iii) C16-MCM-41/Fe_2O_3; (C) XRD of (i) uncalcined, (ii) functionalized SBA-15 and (iii) SBA-15/Fe_2O_3.

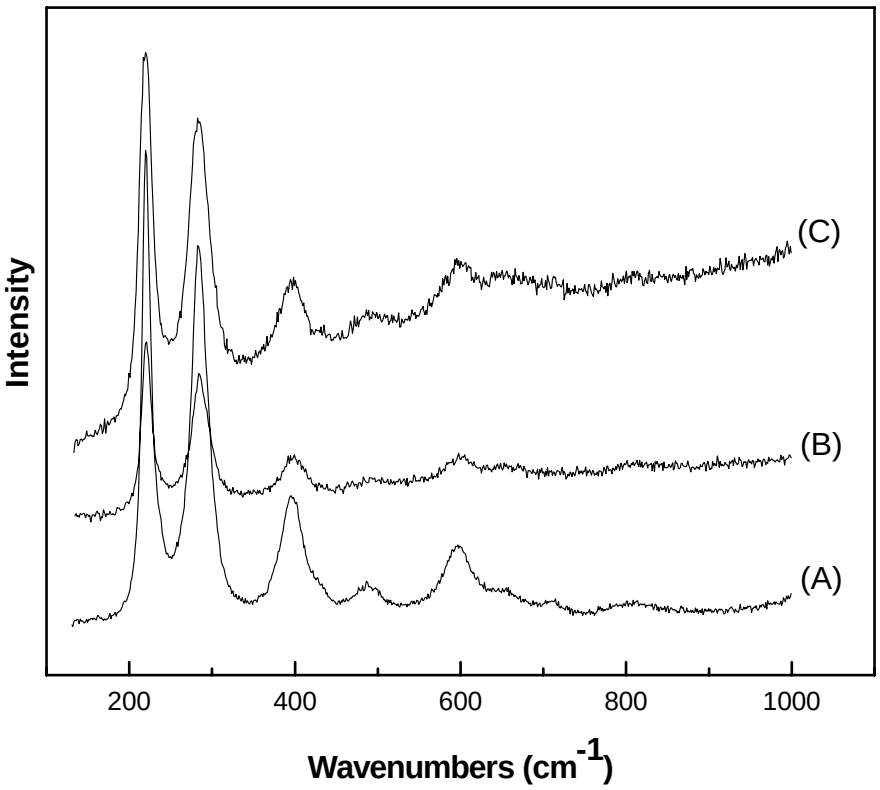

Figure. 3-4 Raman spectra of (A) C8-MCM-41/Fe_2O_3; (B) C16-MCM-41/Fe_2O_3; and (C) SBA-15/Fe_2O_3.

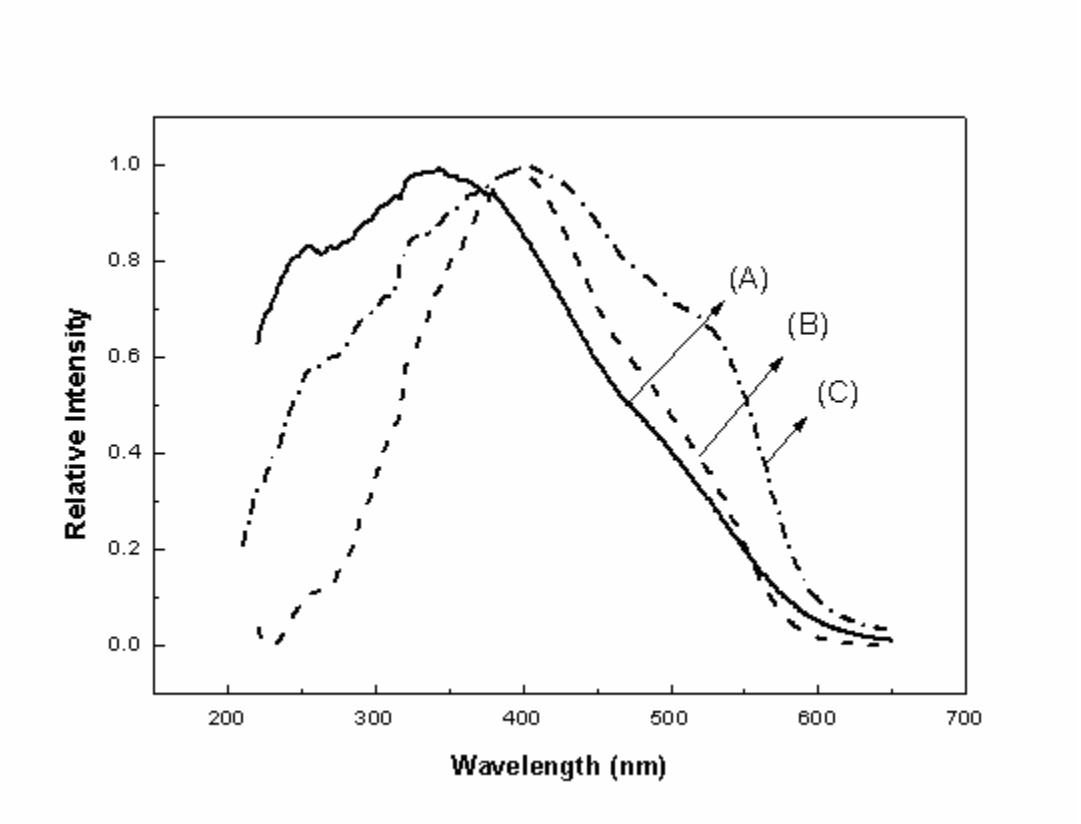

Figure 3-5 DR-UV-vis spectra of (A) C8-MCM-41/Fe_2O_3; (B) C16-MCM-41/Fe_2O_3; and (C) SBA-15/Fe_2O_3.

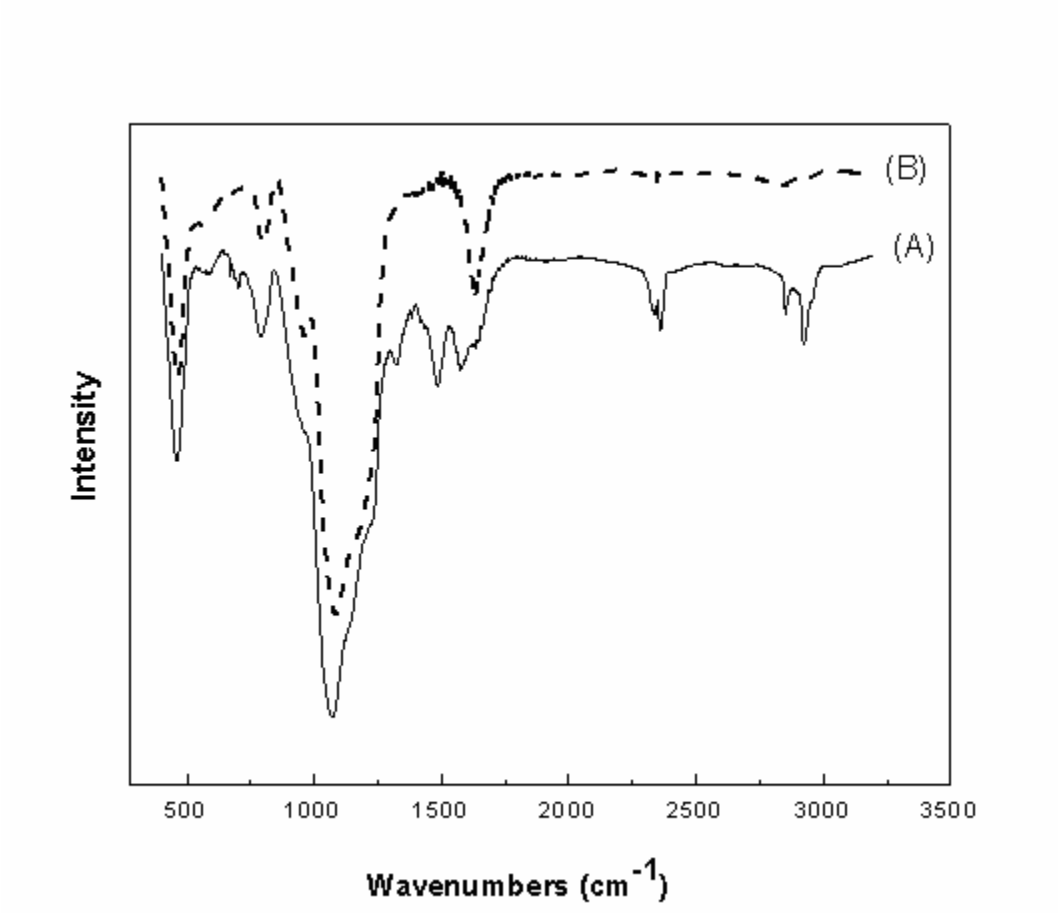

Figure 3-6 Infrared spectra of (A) functionalized C16-MCM-41 and (B) C16-MCM-41/Fe_2O_3.

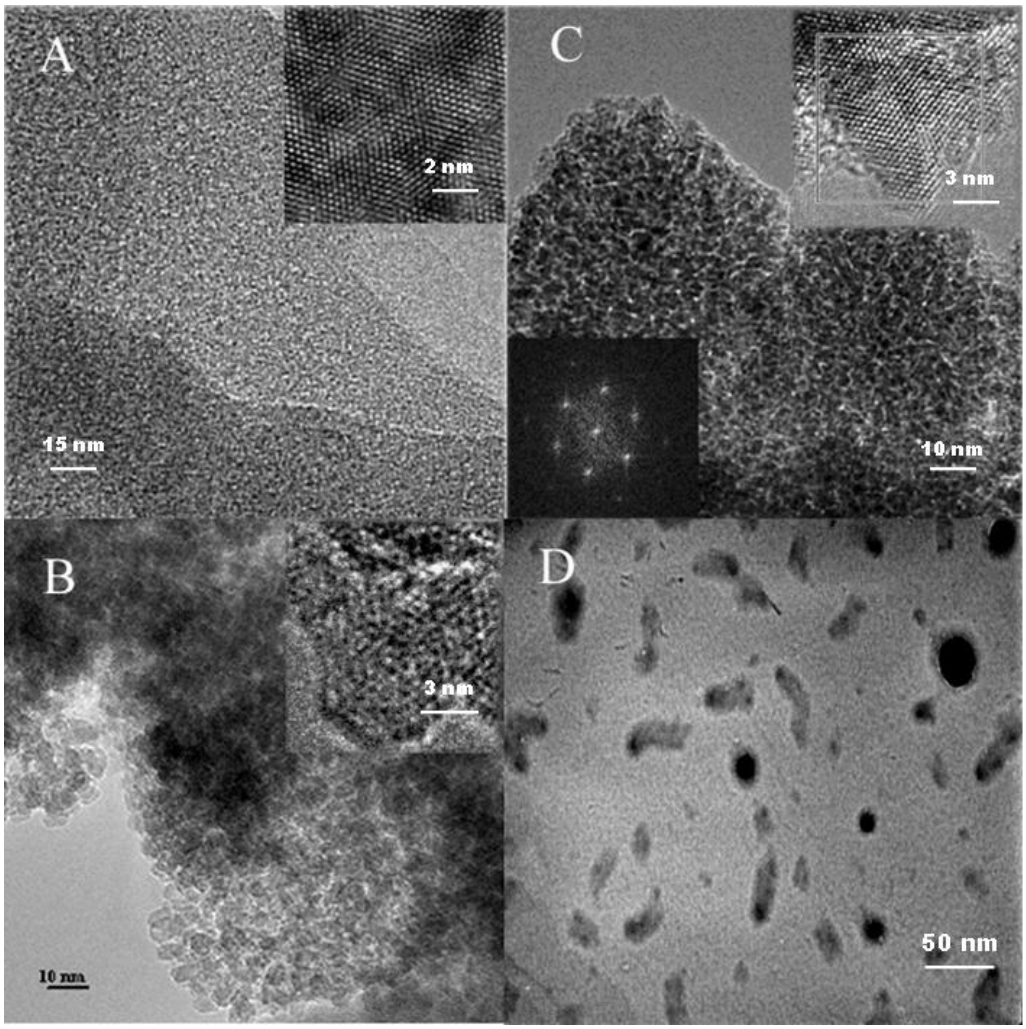

Figure 3-7 TEM of micrographs of (A) C8-MCM-41/Fe_2O_3, (B) C16-MCM-41/Fe_2O_3 and (C) SBA-15/Fe_2O_3. The bottom inset in (C) is the digital diffraction image of Fe_2O_3 in SBA-15. (D) Shows nanostructural Fe_2O_3 recovered from SBA-15/Fe_2O_3 after harvesting from the SBA-15 matrix; micrograph acquired using a JEOL 100cx TEM operated at 100kV.

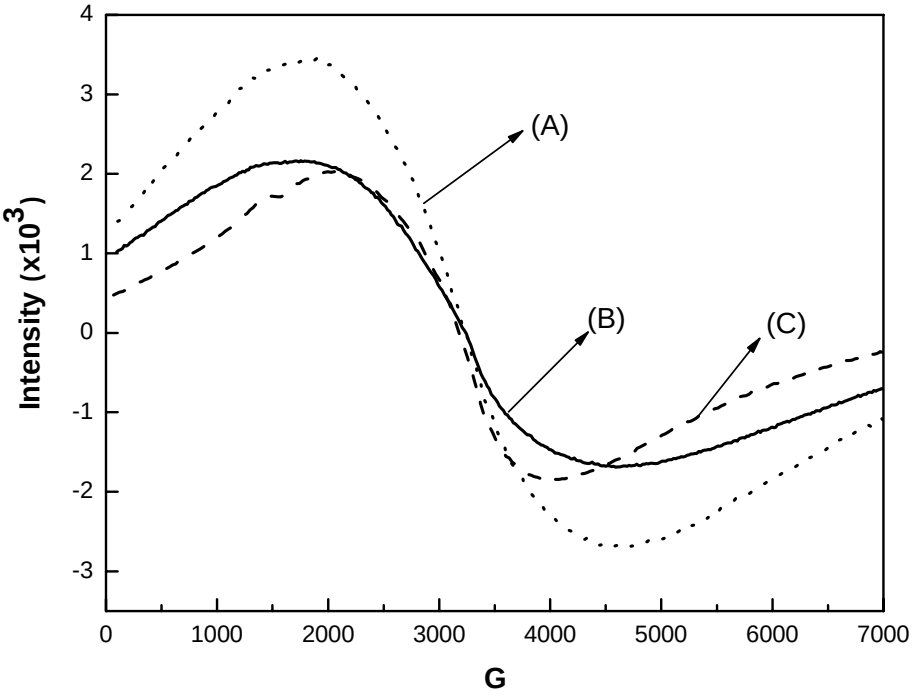

Figure 3-8 First derivative EPR spectra of a single scan from 99.15 G to 7099.15 G of (A) C8-MCM-41/Fe_2O_3, $Y'_{H\rightarrow 0} \cong 1060$; (B) C16-MCM-41/$Fe_2O_3$, $Y'_{H\rightarrow 0} \cong 810$; and (C) SBA-15/$Fe_2O_3$, $Y'_{H\rightarrow 0} \cong 502$.

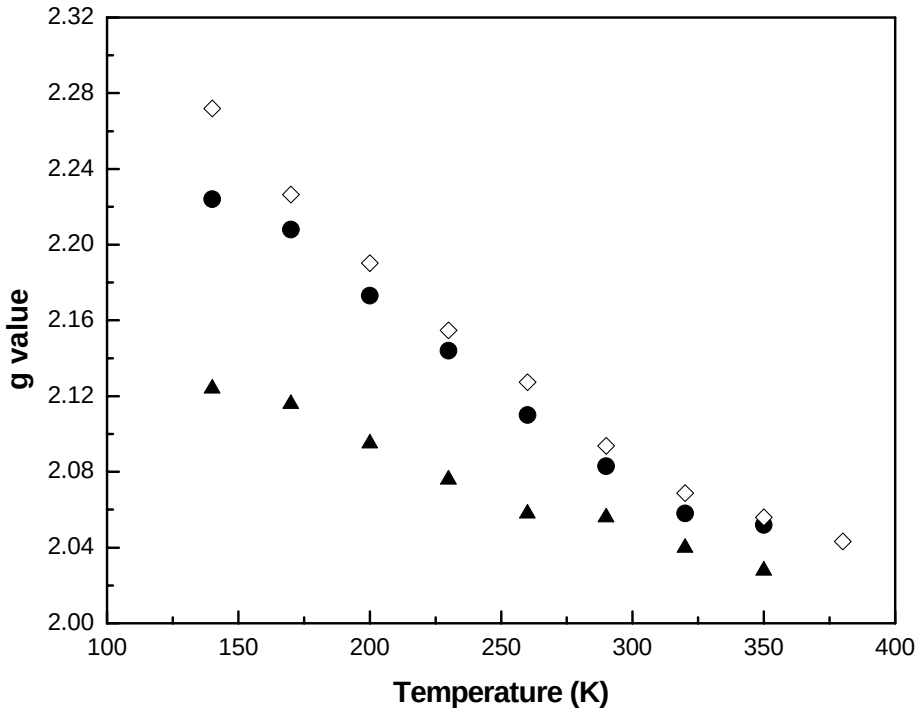

Figure 3-9 Temperature dependence of the g-value for (A) C8-MCM-41/Fe_2O_3 (•); (B) C16-MCM-41/Fe_2O_3 (◊); and (C) SBA-15/Fe_2O_3 (▲).

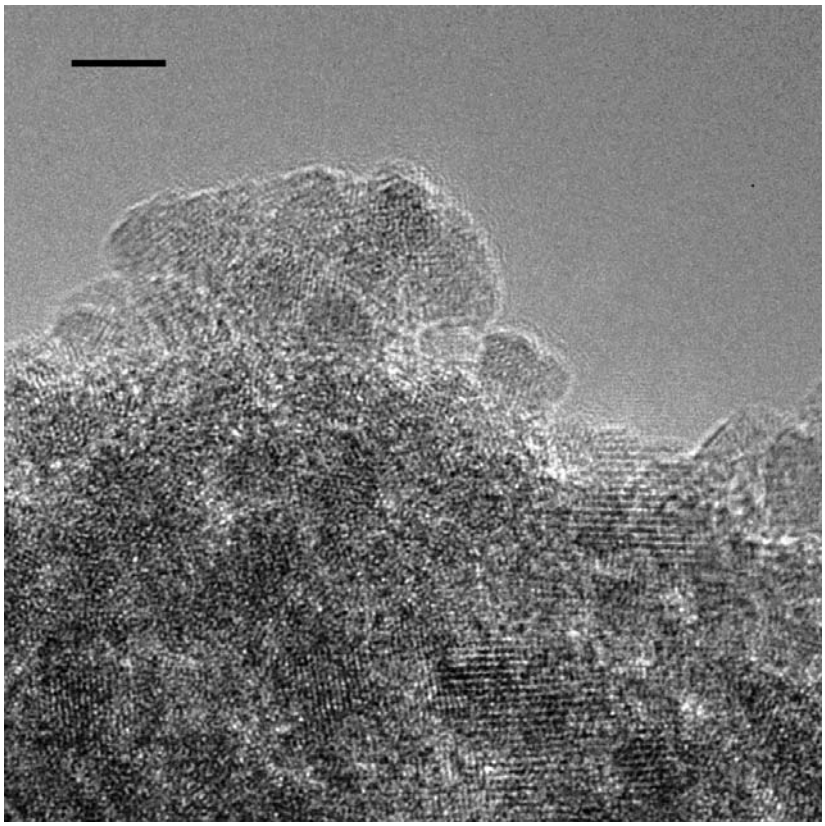

Figure 3-10 TEM of MCM-48/Fe_2O_3. Scale bar=5 nm.

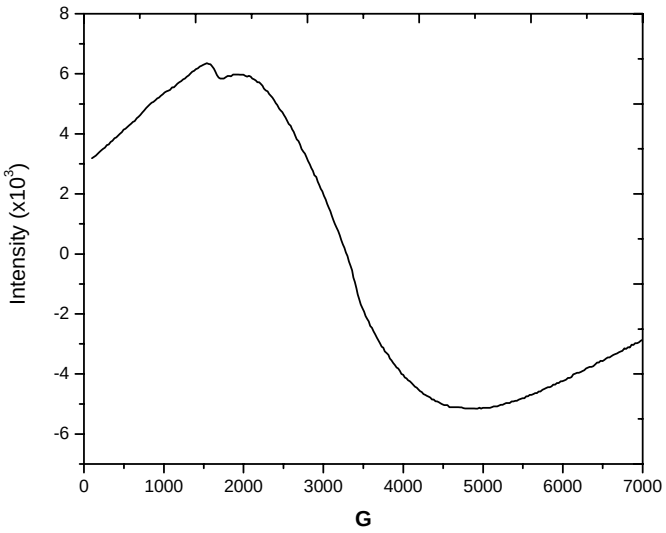

Figure 3-11 First derivation EPR spectra of 1 scan from 99.15 G to 7099.15 G of MCM-48/Fe_2O_3 with Fe_2O_3.

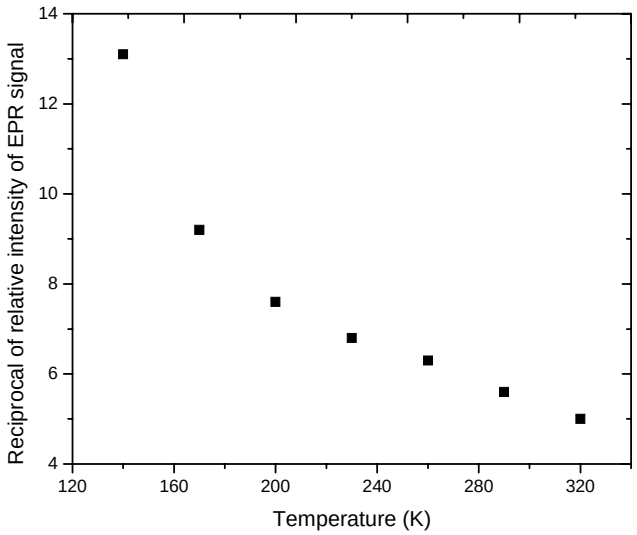

Figure 3-12 Variation with temperature of the reciprocal of integrated intensity of the EPR signals of MCM-48/Fe_2O_3 with Fe_2O_3 (●).

Table 3-1: Quality factor (Q) for the microwave cavity when the different composites are encapsulate. The experimental conditions are P = 0.7 mW, MA = 10.5 G, f = 9.49 GHz, and the cell is a 5 mm quartz tube. The applied field is 99 G.

Blank tube	C8-MCM-41	C16-MCM-41	SBA-15	MCM-48
3500	1800	2800	3000	2000

Chapter 4: Self-Aligned Magnetic Dipole Moments of Fe_2O_3 within Sol-Gel Matrix

4.1 Introduction to Sol-gel Process

The sol-gel process is a versatile solution process initially used for the preparation of inorganic materials such as glasses and ceramics of high purity and homogeneity. It involves the transition of a system from a liquid "sol" into a solid "gel" phase and has been the subject of several books and reviews [1]. The sol-gel process can ordinarily be divided into the following steps: forming a solution, gelation, aging, drying, and densification. In the preparation of a silica glass, one starts with an appropriate alkoxide, tetramethyl orthosilicate (TMOS) or tetraethyl orthosilicate (TEOS), which is mixed with water and a mutual solvent, such as ethanol or methanol, to form a solution, hydrolysis leads to the formation of silanol groups Si-OH. These species are only intermediates as they react further, i.e. condense, to form siloxane Si-O-Si groups. As the hydrolysis and condensation reactions continue, viscosity increases until the "sol" ceases to flow and form the "gel". The overall reactions leading to the formation of a

$$Si(OCH_3)_4 + 4H_2O \rightarrow Si(OH)_4 + 4CH_3OH$$
$$nSi(OH)_4 \rightarrow nSiO_2 + 2nH_2O$$

silica gel starting from TMOS are:

There are several parameters which influence the hydrolysis and condensation reactions (sol-gel process), including the activity of metal alkoxide, water/alkoxide ratio, solution pH, temperature, and nature of the solvent and additive. Another consideration is that catalysts are frequently added to help control the rate and the

extent of hydrolysis. By varying these processing parameters, materials with different microstructure and surface chemistry can be obtained. Further processing of the "sol" enables one to make ceramic materials in different forms. Thin films can be produced on a piece of substrate by spincoating or dip-coating. When the "sol" is cast into a mold, a wet "gel" will form. With further drying and heat-treatment, the "gel" is converted into dense ceramic or glass particles. If the liquid in a wet "gel" is removed under a supercritical condition, a highly porous and extremely low density material called "aerogel" is obtained. As the viscosity of a "sol" is adjusted into a proper viscosity range, ceramic fibers can be drawn from the "sol". Ultra-fine and uniform ceramic powders are formed by precipitation, spray pyrolysis, or emulsion techniques.

Sol-gel process is one of the most active and promising areas of ceramic research. Its ambient processing conditions enable one to encapsulate numerous organic, organometallic, and biological molecules within these sol-gel derived inorganic matrixes. Sensor technology is perhaps the field with highest commercial potential for these materials, since they combine the mechanical strength, transparency in the visible, high porosity and surface area of gel-derived oxides. Sol-gel is also an effective way and is extensively utilized to design and synthesize inorganic-organic hybrid materials with nanometer-scale architecture. Even the hybrid materials thus prepared are comprised of components having very different refractive index, they are often optically transparent due to small scale lengths over which phase separation may exist. As a result, these hybrid materials can find applications in many fields which are far beyond the scope of application of traditional composite materials. Tremendous progress in both fundamental understanding of the sol-gel process and the development

of new organic-inorganic hybrid materials have been made and extensively reviewed [2].

Magnetic iron oxide nanomaterials are currently of great interest because of their wide utility in magnetic and nonlinear devices, as catalyst, as active elements in gas-sensor systems, and as agents to aid in drug delivery [3-6]. Extensive research efforts, by a large number of groups, have shown that the magnetic properties of nanoscaled magnetic materials depend dramatically on the size of the particles, their surface states, as well as their state of dispersion [7]. An obvious approach for reducing the dimensions, separating, and protecting the surfaces of magnetic nanoparticles is to form composites consisting of nanometer-sized magnets within non-magnetic matrices, such as organic resins [8], polymers [9], zeolites [10], and mesoporous solids [11]. Such composite systems may have unique properties that can be exploited for device or sensor applications, but may also represent materials that are well suited for general studies of magnetism of nanoparticles.

Iron forms several oxides, with oxidation state II (FeO) and with oxidation state III (Fe_2O_3), or a mixture of both (Fe_3O_4). FeO has a cubic rock salt structure. The black powder is metastable disproportionating at temperatures below 575°C but can be obtained under rapid cooling. Fe_2O_3 is reddish-brown and has two modifications, namely α and γ. The α-form has a hexagonal close packed structure of oxygen ions and metal ions in the octahedral sites. Fe_2O_3 has a cubic close packed structure of oxygen ions and the metal ions occupy sites that give trigonal inverse spinel structure. Fe_2O_3 is extensively used in magnetic recording tape and disc manufacturing. It is used as such

or mixed with other metals e.g. cobalt. γ-Fe_2O_3 is a permanent magnet material, and is stable at ambient temperature. The demand of increasing recording density has created materials science research in order to decrease the domain size, but keep it stable towards thermal fluctuations. The lower limit for magnetic domains is about 30 nm.

Hematite has a rhombohedrally centered hexagonal structure of the corundum type with a close-packed oxygen lattice in which two-thirds of the octahedral sites are occupied by Fe(III) ions (Figure 4-1). A noticeable feature of the hematite structure is the arrangement, where the FeO_6 octahedra shares edges inside the basal (0 0 1) plane and one face in Fe_2O_9 dimers along the *c*-axis. α-Fe_2O_3 nanoparticles exhibit unique features in many industrial applications. Nanostructured hematite can be prepared by electrochemical synthesis, by decomposition of organic iron compounds in alkaline media (pH > 12) or by oxidation of pure iron at high temperature.

Recently, work from this laboratory has identified a new kind of microwave absorbent materials in which Fe_2O_3 nanoparticles are encapsulated within MCM-41 and SBA-15 mesoporous materials [12]. In the present paper we extend our studies with Fe_2O_3 nanoparticles and examine a convenient and simple sol-gel approach for forming Fe_2O_3 nanoparticles within a SiO_2 matrix. The sol-gel derived oxide matrix acts as an excellent support for the dispersion of metal or metal oxide magnetic particles. The process of forming the gel is based on the hydrolysis of a precursor, i.e., tetraethoxysilane (TEOS), and a subsequent condensation of hydrolyzed TEOS in a hydroalcoholic solution of the metal salt. The resultant silica matrix possesses pores that both limit the size of the precipitated phase and isolates particles from one another.

As with our earlier study, EPR and *Q* factor measurements in the present study indicate that there exists self-alignment of magnetic dipole moments within the composite material. We again find that this alignment leads to significant microwave absorption ability and absorption of microwave energy even at zero-applied field. The sol-gel medium enables the easy formation of films of this microwave absorbing material on different surfaces.

4.2 Experimental Section

The SiO_2 based composites with various Fe_2O_3 compositions were obtained by a sol-gel co-precipitation synthesis. Briefly, 1 ml of tetraethoxysilane (TEOS, Alfa, 98%) was dispersed in 25 ml solutions of ethanol containing 0.15, 0.33, 0.90 and 2.0 g of $Fe(NO_3)_3 \cdot 9H_2O$ (Alfa, 99.999%) to produce a series of stock compositions with wt% ratio $Fe_2O_3/(Fe_2O_3 + SiO_2)$ of 8.6, 16.4, 33.2 and 52.8, respectively. Small amounts of nitric acid solution were added to catalyze the reaction. The mixtures were stirred for 1 hour at room temperature and then heated at 80 °C to remove the solvent. The resultant dark brownish solids were washed and heated at 180 °C for 24 h in air to obtain the final products.

Absorption spectra were recorded using a Perkin-Elmer, Lambda 18, UV-vis-NIR spectrometer. X-ray diffraction (XRD) measurements were acquired with a Rigaku diffractometer using Cu $K_{\alpha 1}$ (0.154 nm) X-rays: typically run at a voltage of 40 kV and current of 30 mA. IR spectra were taken on Thermo Nicolet Auntar 360 FTIR. The Raman spectrum was acquired using a J-Y LabRam HR800 micro-Raman instrument with 632.8 nm excitation provided by a HeNe laser. EPR spectra were recorded with a

Bruker ESO380E spectrometer operating at the X-band and equipped with a HP 5361 frequency counter; spectra at room temperature were obtained under the following settings: microwave power, ~0.7 mW; modulation amplitude, 10.45 G; modulation frequency, 100 KHz; time constant, 1.28 ms; sweep period, up to 168 s; sweep width, 7000 G; and the X-axis resolution, 4 K. Transmission electron microscope images were acquired using powered samples that were dry loaded onto Cu grids with holey carbon films, and utilized a JEOL 100CX TEM microscope operated at 100 KV.

4.3 Results and Discussion

Fe_2O_3/SiO_2 ratios in the as-prepared compositions determined by elemental analysis are 8.6, 16.4, 33.2 and 52.8, respectively. No nitrogen can be detected which indicates ferric nitrate has been decomposed into ferric oxide after the heat treatment.

X-ray diffraction spectra recorded for the samples as a function of the amount of iron oxide contained within the silica matrix are presented in Figure 4-2. For samples with iron oxide contents of 8.6 wt% and 16.4 wt%, no characteristic diffraction lines of Fe_2O_3 were observed, due to the extremely small particle size, and a broad peak at about 20° can be attributed to the amorphous SiO_2. For the samples with 33.2 and 52.8 wt% Fe_2O_3, two weak and broad diffraction bands appear at approximate 33.1° and 35.6°. The position and relative intensity of these lines correspond to diffraction peaks for α-Fe_2O_3 (i.e., hematite, JCPDS CARDS 86-0550). Additionally, Raman spectroscopy, as provided in Figure 4-3 for the 60 wt% sample, was also be used to characterize the phase of the Fe_2O_3 in the composites. Five well-defined bands at approximately 222, 287, 401, 495 and 601 cm^{-1} are observed. These bands, although

blue-shifted by a few wavenumbers from those of the bulk materials, clearly indicate the existence of □α-phase Fe_2O_3 nanoparticles [13, 14]. Additionally, TEM dark-field images of Fe_2O_3 nanocomposites, as shown in Figure 4-4, reveal that nanocrystalline, nearly spherical particles are present, which can be seen to be dispersed throughout the SiO_2 matrix. The average particle sizes of iron oxide are roughly estimated to range from 3 nm to 11 nm, dependent on the Fe_2O_3 content in the composites.

Figure 4-5 shows the diffuse reflectance (DR) UV-vis spectrum of the composites. For the 8.6 wt% Fe_2O_3 nanocomposite, the 241 nm band can be assigned to the charge transfer from oxygen atom to Fe(III) ion [15]. For the 16.4 wt% sample, d-d transition of Fe(III) at higher wavelength becomes dominant in the range of 300 to 500 nm [16]. It should be noted that with higher iron content, the absorption tails to longer wavelength, which indicates the presence of iron oxide nanoparticles and their agglomerates within the cavities [17].

FTIR spectra recorded at room temperature for all Fe_2O_3/SiO_2 composites are shown in Figure 4-6. Most of the spectra show features attributable to vibrations of Si-OH and Si-O-Si [18], although the infrared band at ca. 570 cm^{-1} might be assigned to the stretching vibration of Fe-O. Since no absorption bands at 900 or 680 cm^{-1} occur, there is not a band that is attributed to Si-O-Fe structure features [19]. Thus, FTIR spectra suggest there is no strong interaction between Fe_2O_3 and the SiO_2 matrix (as evidenced by the absence of Si-O-Fe vibrations) and the FTIR spectrum of the composite can be reasonably considered the superimposed spectrum of iron oxide and the silica matrix.

To investigate the magnetic behavior of the as-prepared Fe_2O_3 nanocomposites, we carried out electron paramagnetic resonance (EPR) studies. Figure 4-7 shows first derivative EPR spectra of samples at room temperature. Broad EPR signals of g value ~2.0 were observed for Fe_2O_3 nanocomposites, corresponding to the resonance line coming from Fe^{3+} coupling pair (e.g., Fe^{3+}-O-Fe^{3+}) in the cage. Beside the g value of ca. 2.0, these Fe_2O_3 nanocomposites also exhibit a small but distinct signal at g ~ 4.3, corresponding either to a strongly distorted rhombic sites located on the surfaces of the particles or to isolated iron (III) ions dispersed in the pores [20].

We also observed that nanocomposites with Fe_2O_3 content of 33.2 and 52.8 wt% have strong absorptions at the magnetic field of ~ 99 G, and that even when one extrapolates the applied field to zero strength the microwave absorption remains nonzero. This nonzero absorption is neither found for the non-magnetic SiO_2 matrix, nor for iron oxide prepared by the same route but without the use of the matrix, indicating that the nonzero absorption likely results from some intrinsic level of alignment of the magnetic dipole moments of the encapsulated Fe_2O_3 nanoparticles. This intrinsic alignment most probably derives from strong dipole-dipole interactions associated with confinement and dense packing within the cavities.

The above deduction is supported by the observed temperature dependence of the integrated EPR intensities, as shown in Figure 4-8. Generally, the EPR signal amplitude is inversely proportional to the absolute temperature, according to the Curie-Weiss law. Such a dependency, indeed, is what is found for Fe_2O_3 in the SiO_2 matrix at low load levels (i.e., 8.6 wt% and 16.4 wt% samples), where confinement-forces due to the SiO_2 matrix would normally dominate the short-range interactions between

magnetic particles, and would effectively block the interaction between the Fe_2O_3 particles [21], resulting in the samples being paramagnetic. For the high-load samples (i.e., 33.2 wt% and 52.8 wt%), however, as shown in Figure 4-8, the EPR signal strength increases with increasing temperature, indicating that there exists a significantly stronger interaction between the magnetic nanoparticles, and that an exchange interaction (antiferro) is present [20]. The greater EPR signal with increase of temperature, of course, results from the reorientation of magnetic moments parallel to the field as the temperature is increased [22, 23]; this alignment of magnetic dipole moments explains the enhanced microwave absorption ability.

Quantitatively, the microwave absorption ability is represented by the microwave absorption quality factor (*Q*) at 99 G (see Table 1), where *Q* is defined by the following equation, and represents how efficiently the cavity stores microwave energy.

$$Q = \frac{2\pi(\text{energy stored})}{\text{energy dissipated percycle}}$$

Relatively speaking, a smaller *Q* factor indicates stronger microwave absorption ability for one material versus another. From Table 1, all of *Q* factors for Fe_2O_3/SiO_2 composites are lower than that of the blank tube, indicating that all the Fe_2O_3 nanocomposites have microwave absorption abilities greater than air, and the sample with 33.2 wt% Fe_2O_3 has the strongest microwave absorption. In fact, according to the literature [24], the SiO_2 matrix can contain up to 33.2 wt% Fe_2O_3, meaning that the composite formed from the 52.8 wt% sample likely has a substantial fraction of the Fe_2O_3 lying outside the matrix and thus has no enhanced microwave absorption ability.

It should be pointed out that the choice of a suitable gelation tempaerature is important for successful magnetic alignment of magnetic dipole of Fe_2O_3 in SiO_2 matrix. Different gelation temperature was changed to study the magnetic dipole moment alignment of Fe_2O_3 nanoparticles in so-gel matrix, it show that the gelation temperature affect the non-zero absorption greatly (Figure 4-10). At 50 ^oC for example, nearly no non-zero absorption can be observed compared to the results we discussed previously and Q factor is only 3000. Also the magnetism vs. temperature curves (Figure 4-11) show the under such conditions, the Fe_2O_3 show paramagnetic properties. The reason is not clear, however one possible explanation is that the gelation temperature will affect the phase of Fe_2O_3. At 50 ^oC some γ-Fe2O3 is present which show paramagnetic behavior.

4.4 Conclusion

The present work shows that composites derived from different loading percentages of Fe_2O_3 in a SiO_2 matrix can be formed using a sol-gel co-precipitation synthesis approach. EPR measurements have shown that for sufficient loading of Fe_2O_3, the composite material exhibits nonzero absorption at zero applied magnetic field as well as substantial microwave absorption capability for moderate applied fields. The convenient synthesis in conjunction with the magnetic properties of the composites suggests use as a microwave absorbing material.

Table 4-1: Quality factor (Q) of the microwave cavity for different composites at an applied field of 99 G.

Samples	Blank tube	8.6 wt%	16.4 wt%	33.2 wt%	52.8 wt%
Q	3600	3300	3000	2300	2400

Experimental conditions: power = 0.7 mW; modulation amplitude = 10.5 G; frequency = 9.49 GHz. Sample cell was a 5 mm quartz tube.

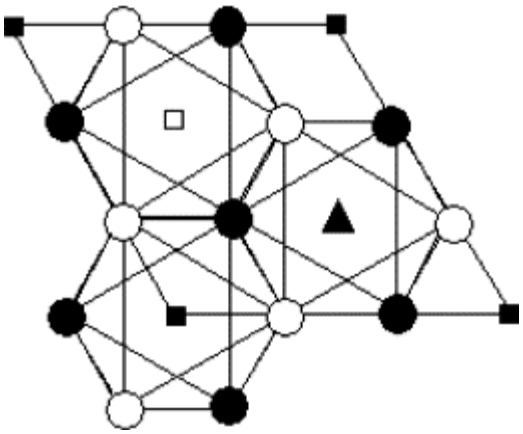

Figure 4-1: Schematic structure of α-Fe_2O_3. Projection along [0 0 1], •: O at z=1/12, 5/12, 3/4; o: O at z=1/4, 7/12, 11/12; ■: Fe at z=1/6, 1/3, 2/3, 5/6; ▲: Fe at z=0, 1/6, 1/2, 2/3; □: Fe at z=0, 1/3, 1/2, 5/6.

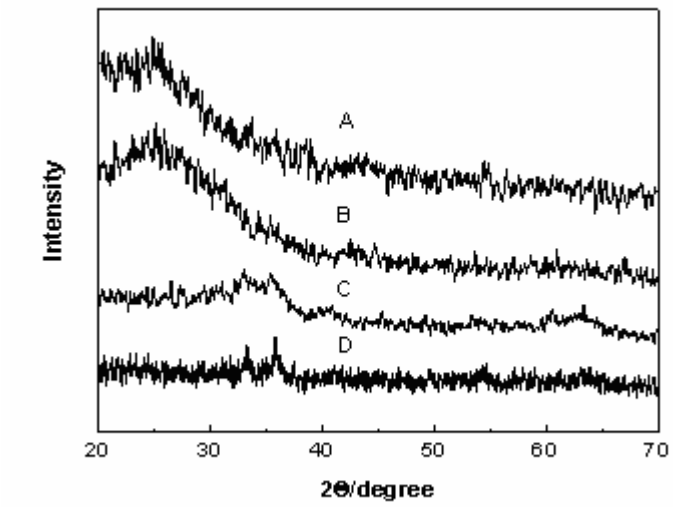

Figure 4-2: X-Ray diffraction patterns of Fe_2O_3/SiO_2 nanocomposites: (A) 8.6 wt%; (B) 16.4 wt%; (C) 33.2 wt%; and (D) 52.8 wt%.

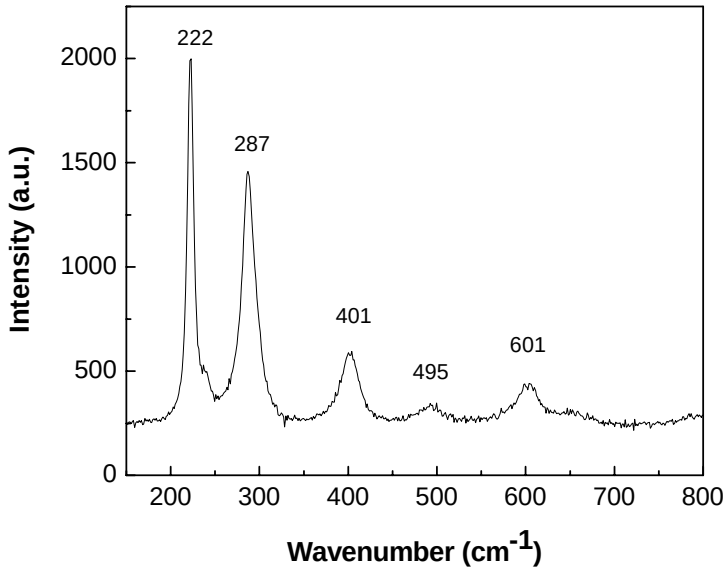

Figure 4-3: Raman spectrum of 52.8 wt% Fe_2O_3/SiO_2 nanocomposite.

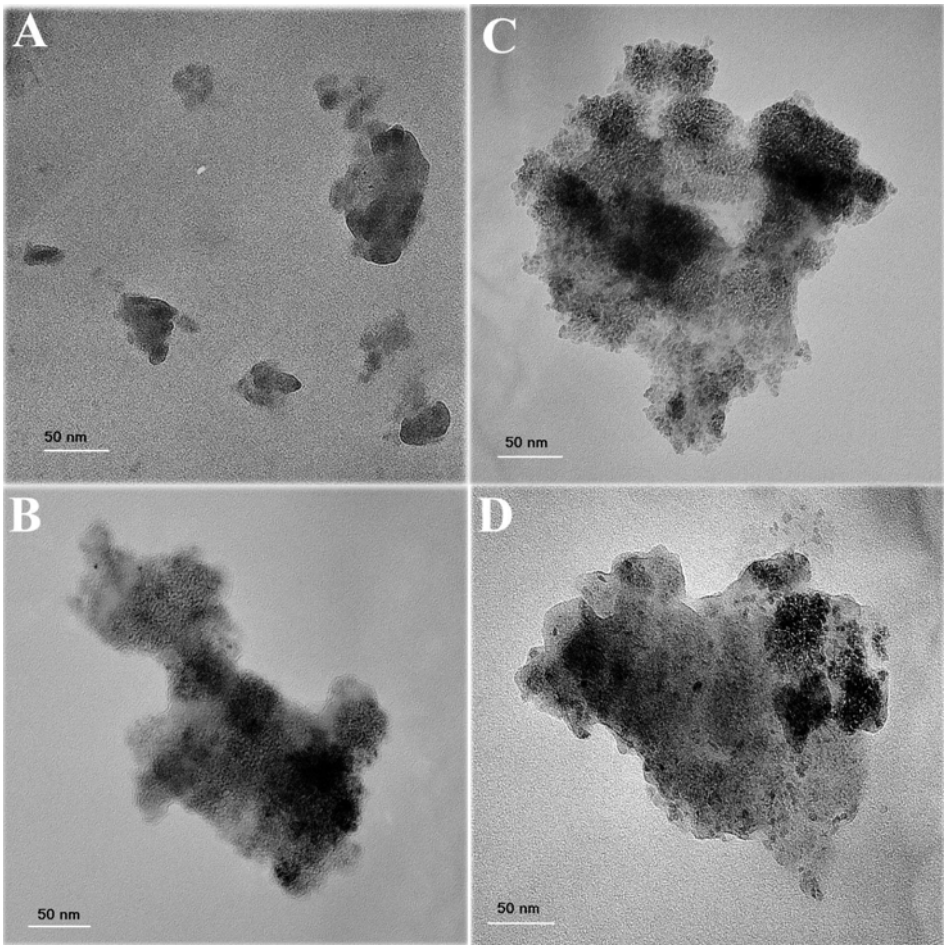

Figure 4-4: TEM micrographs of Fe_2O_3/SiO_2 nanocomposites: (A) 8.6 wt%; (B) 16.4 wt%; (C) 33.2 wt%; and (D) 52.8 wt%.

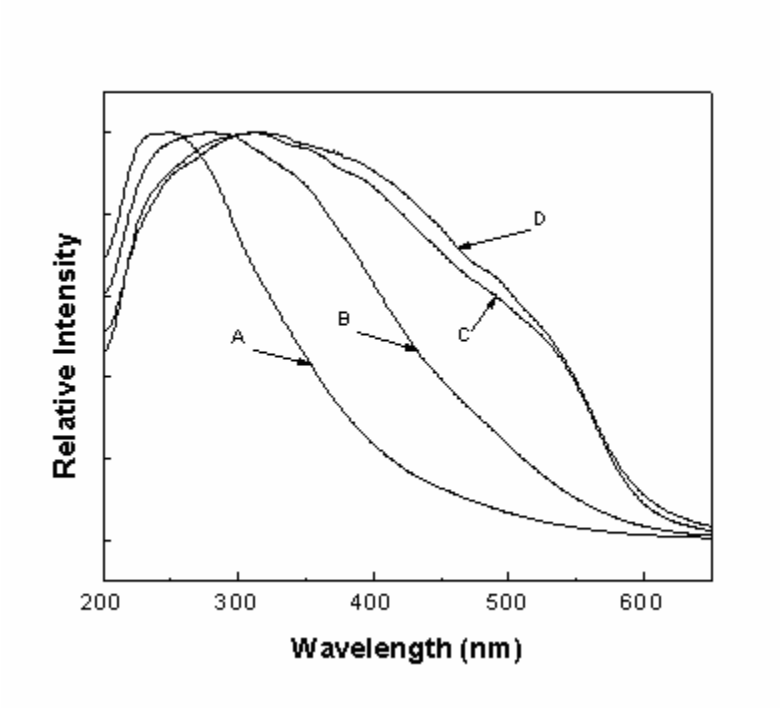

Figure 4-5: DR-UV-vis spectra of Fe_2O_3/SiO_2 nanocomposites: (A) 8.6 wt%; (B) 16.4 wt%; (C) 33.2 wt%; and (D) 52.8 wt%.

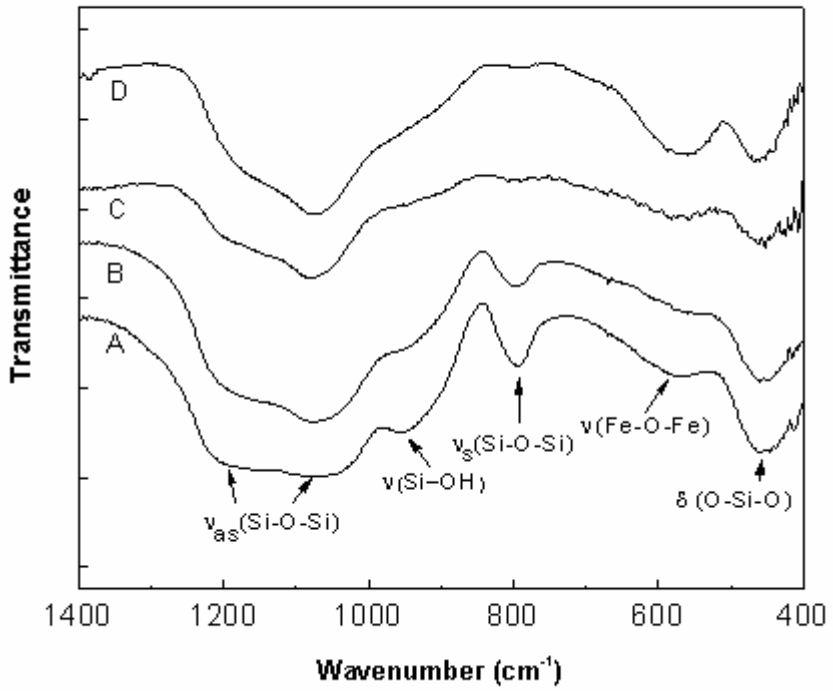

Figure 4-6: FT-IR spectra of Fe_2O_3/SiO_2 nanocomposites, (A) 8.6 wt%; (B) 16.4 wt%; (C) 33.2 wt%; and (D) 52.8 wt%.

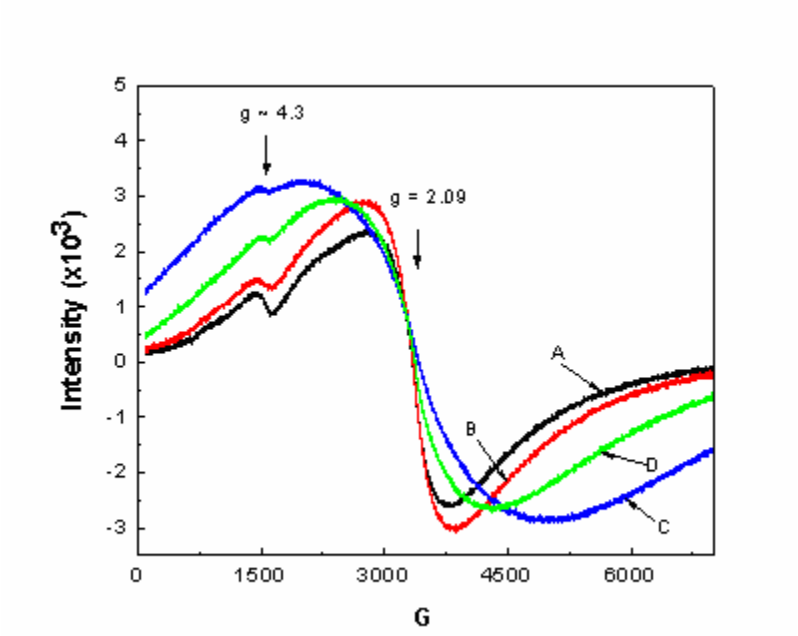

Figure 4-7: First derivative EPR spectra of single scans from 99.15 G to 7099.15 G for Fe_2O_3/SiO_2 nanocomposites: (A) 8.6 wt%; (B) 16.4 wt%; (C) 33.2 wt%; and (D) 52.8 wt%.

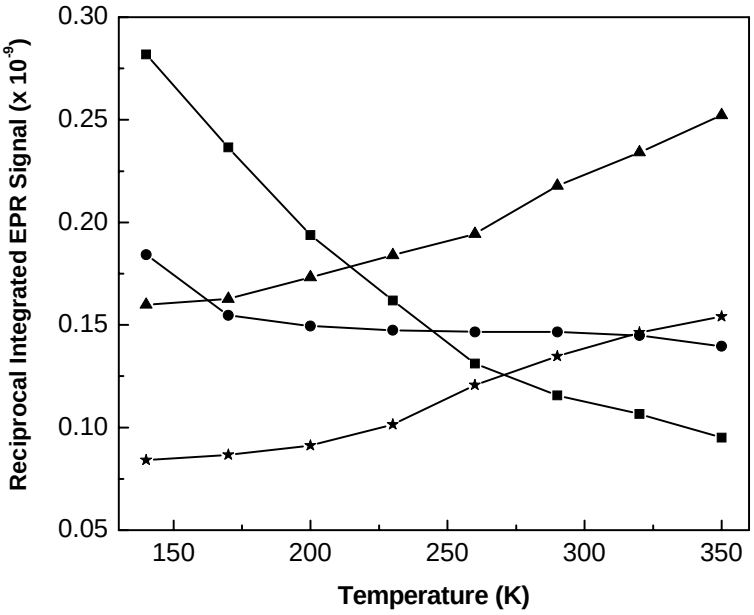

Figure 4-8: Variation with temperature of the reciprocal of the integrated intensities of EPR signals for Fe_2O_3/SiO_2 nanocomposites o (A) 8.6 wt% (▲); (B) 16.4 wt% (★); (C) 33.2 wt% (•); and (D) 52.8 wt% (■).

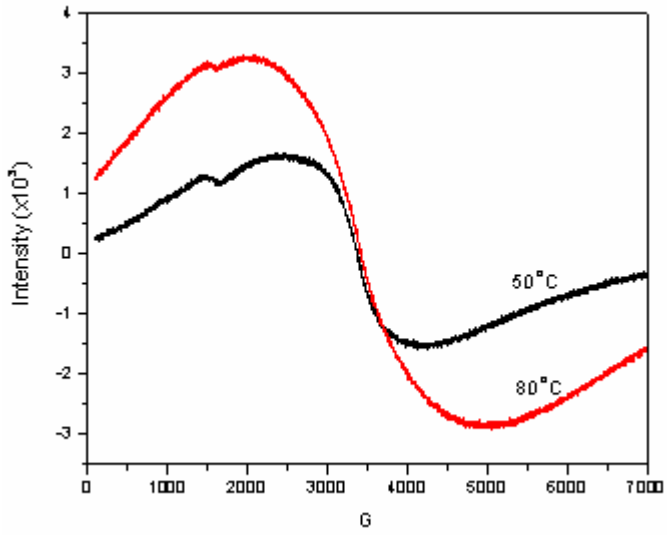

Figure 4-9: Gelation temperature influence on magnetic properties of Fe_2O_3, (A) 50 ^oC and (B) 80 ^oC

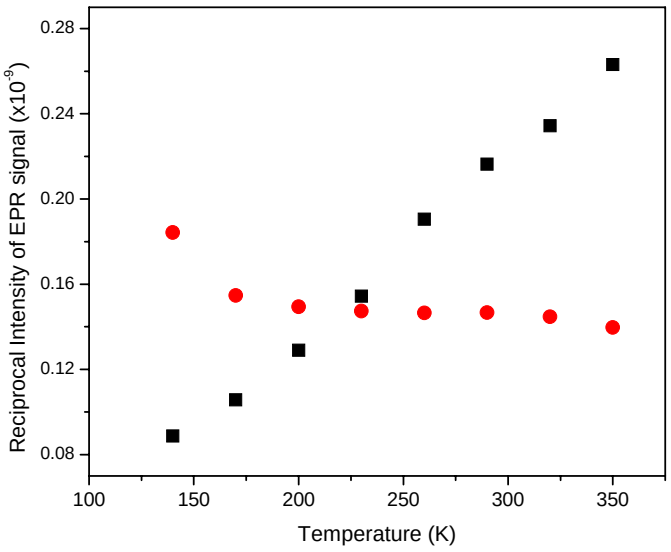

Figure 4-10: EPR signal amplitude variation with temperature of Fe_2O_3-SiO_2, at (A) 50 ^oC, (B) 80 ^oC.

Chapter 5: Optical Spectra Study of a Novel Polyoxometalate Occluded within MCM-41

The impact of polyoxometalate chemistry since the synthesis of the first derivative in 1826 is beyond all doubt. Experimentalists have studied these complexes for a long time and much is known about their behavior and applications. Experimental techniques were used to study their properties and knowledge rapidly increased. The unprecedented properties and the virtually unlimited structural possibilities of these compounds have focused the attention of a large number of chemists for decades. The present chapter introduces the general characteristics of polyoxometalates and in the latter section, the novel polyoxometalates ($[(Eu_2PW_{10}O_{38})_4(W_3O_8(H_2O)_2(OH)_4]^{22-}$) have been immobilized inside the channels of MCM-41 mesoporous molecular sieve by means of incipient wetness method. The photoluminescent behavior of the composite at room temperature was investigated to show the characteristic Eu^{3+} emission pattern of $^5Do–^7F_J$. The occurrence of photoluminescent activity confirms the potential for creating luminescent functional materials with polyoxometalates (POMs).

5.1 Introduction to Polyoxometalates

The great majority of inorganic compounds are constructed of metallic atoms as principal entities. This means that this subgroup of chemicals has considerable structural diversity, although it is still surpassed (in number of classified and characterised compounds) by organic compounds. However, inorganic molecules have greater potential because the number of elements in

purely inorganic molecules, combined with their structural diversity, makes them more powerful, particularly as far as their applications are concerned. In fact, the search for new features puts more importance on the elements in a framework than on the structure itself. In the organic world, the principal variable that produces novel behaviour is the structure. In this sense, maybe the field of polyoxometalates (POMs) lies between the organic and the inorganic worlds.

The first POM, the phosphomolybdate of formula $[PMo_{12}O_{40}]^{3-}$, was reported by Berzelius [1] in 1826. In the early 1930s, Keggin [2] solved the structure of the related anion $[PW_{12}O_{40}]^{3-}$. Since then, countless structures of POMs have been synthesized and characterized. The turning point came when spectroscopic techniques were used for characterization. Today, POMs constitute an immense class of polynuclear metal-oxygen clusters usually formed by Mo, W or V and mixtures of these elements. They have potential applications in many fields including medicine, catalysis, multifunctional materials, chemical analysis, etc. Dozens of elements have been reported as taking part in POM compounds. In addition, beyond this chemical flexibility, they have an 'organic-like' structural diversity and the number of frameworks synthesised increases daily.

5.1.1 Structural Principles of Polyoxometalates

5.1.1.1 Basic Structural Units

POMs are a family of medium-to-large-sized molecular (discrete) metal oxides. Nevertheless, due to the increasing diversity of structures classified as such in the literature, the unequivocal definition of this group of compounds becomes gradually

more and more diffuse. This diversity is somehow a consequence of the rich, unprecedented and unusual properties associated to POMs. Many authors claim that they can be regarded as packed arrays of pyramidal MO5 and octahedral MO6 units (see Figure 5-1). The very important MO_6 units (and the MO_5 partner as well but to a lesser extent) are, then, packed to form countless shapes. They join to one another, apparently, in accordance with a few simple rules (as $-CH_2-$ does in organic molecules). Observing a representative set of POM clusters, and identifying the MO_6 blocks, we notice that the molecule as a whole is built by edge- and/or corner-sharing MO_6 octahedra.

5.1.1.2 Clathrate-like Structures

Clathrate-like systems are molecular or supramolecular arrangements in which an internal unit is encapsulated by an external core. A formulation for molecules that accomplish the requirements of a clathrate-like system was introduced in the way $[XO_4]_m^{n-}@[MO_6]$. X^{n+} represents a central atom surrounded by a cage of M addenda atoms, such as molybdenum(VI) or a mixture of elements, each of them composing MO_6 (M-oxygen) octahedral units. The addenda atoms are partially substituted by other elements, such as vanadium, transition metals, lanthanides, halogens and inorganic radicals. Keggin, Wells−Dawson and Lindqvist anions were also formulated as

$[XO_4]^{n-}@M_{12}O_{36}$ Keggin,

$[XO_4]_2^{n-}@M_{18}O_{54}$ Wells−Dawson,

5.1.1.3 Chemical elements taking part in POMs

Many heteropoly-anions can be chemically manipulate to generate “holes” by removing up to six WO_6 units. The “holes” of the lacunary species can be filled with a variety of elements, such as molybdenum, vanadium and other metallic elements, lanthanides, etc. Fewer restrictions are found when the heteroatom X is part of a POM. Clusters with p-block elements (P, Si, Al, Ga, Ge...), transition metal elements (Fe(II/III), Co(I/II), Ni(II/IV), Zn(II)...), and even two H+ have been synthesized. This position can be either tetrahedrally coordinated (as in Keggin and Wells−Dawson, anions) or octahedrally coordinated (as in the Anderson structure). Figure 5-3 shows a typical heteropolyanion.

5.1.2 Applications

All the value-adding properties presented above have many applications in the technological, chemical and medical fields. There are too many interesting applications to be listed here. At present, excluding medical and catalytic applications, there are nearly 20 categories in which POMs are attractive species [3]. One of the traditionally reported applications concerns elemental analysis aided by POM chemistry. A large set of species, mostly metal elements, can be determined in solution. The reduction potentials in POM species vary considerably as a function of the geometrical characteristics of the cluster and the addenda atoms that take part. Redox potentials are affected by the overall charge of the species, too. So the reduction/oxidation properties can be tuned by choosing the heteroatom X, the addenda metal M and the framework. POMs have been applied to medicine with

considerable success and efficacy. Their oxidising ability is of particular interest. They catalyze many organic reactions and give high yields of reaction and good selectivity.

The medical or biological/chemical principles governing the interactions between target biomolecules and drugs are redox potential, polarity, shape, surface charge distribution and acidity, which are a set of attributes that chemists can skilfully control in POMs. So the features of POMs can be altered to fit the recognition rules for medical applications. An exhaustive compilation of the knowledge acquired in the field of medical applications of POMs can be found in the Reference [4]. The medical investigation of some oxometalates is promising although it is still in an initial stage. The modus operandi of POMs against viruses or tumoral agents, despite the amount of documentation on the subject, remains unclear. In fact, POMs show high selectivity toward the target system, whether it is an enzyme or a membrane. The data collected over the years suggest that the overall charge and the charge density play a key role in the efficiency of the inhibition. Some reports have concluded that there is a lock-and-key mechanism between POMs and enzymes, so the size and the electrostatic properties of the oxometalate are determining factors for successful remedies.

5.2 Scope of the work

Polyoxometalates (POMs for convenience), a class of molecularly defined inorganic metal oxide cluster with intriguing structures and diverse properties, are a focus of contemporary materials chemistry research [5, 6]. Certainly, one reason

for this interest has been the realization that these materials, when combined with lanthanide ions, can exhibit cooperative properties including: (i) catalytic activity for oxidation and acid dependent reactions [7], (ii) medicinal chemistry [8], (iii) magnetism [9, 10], and (iv) useful optical properties such as photochromism, electrochromism, and luminescence [11-13]. Obviously, polyoxometalates appear to be extremely versatile inorganic building blocks for the construction of functional materials.

Owing to their very low surface area and high solubility in polar solvent, it has necessary to incorporate POM into stable rigid spports, such as polymer, or silica matrices, and active carbon [14, 15]. Among the solid matrices, mesoporous materials are promising supports in application requiring large pores because of their well-defined mesoporous structure in combination with a high surface area. Because the pores are interconnected and open to the ambient environment, the nanoparticles within pores are in contact with the ambient environment. Molecules can diffuse inside the pore structure of mesoporous materials, thereby making the catalytically active site available for reaction [16]. Therefore mesoporous materials loaded with nanoparticles within their pores have received considerable attention recently for their unique properties. The encapsulation of POM structure into the pores of a molecular sieve may provide an active, stable catalyst [17-20]. It is to be noted that unmodified silicate mesoporous material contains many silanol groups and high energy vibration of these groups may quench the luminescence of rare earth ion. Also to promote the occlusion of POM, It is necessary to modify the interior structure of the mesoporous aluminosilicate through use of an alkoxysilane

silylation reagent, in order to incorporate functional groups inside the channels of the mesoporous molecular sieve which would be able to react with POM and form weak interaction. It seems probable that the exposed basic amine groups might react with POMs to form the salt $\cdot Si(CH_2)_3NH_3 \cdot POM$, which will be linked to the modified surface.

In the present study, we have utilized a silylation reagent that contains an amine group, resulting in a strong interaction with the encapsulated POM in MCM-41, with the chemical potential associated with forming the salt $Si(CH_2)_3NH_3 \cdot POM$, which would be attached to the modified surface [14,21]. We specifically report on the encapsulation of $[(Eu_2PW_{10}O_{38})_4(W_3O_8(H_2O)_2(OH)_4]^{22-}$, hereinafter referred to as $Eu_8P_4W_{43}$, within modified MCM-41. Figure 5-4 provides tat molecular mechanics determined the structure of $Eu_8P_4W_{43}$. The minor and major dimensions of this structure are ca. 20 Å and 25 Å for the minor and major dimensions, respectively [22].

5.3 Experimental

Synthesis of MCM-41 and Polyoxometalates ($Eu_8P_4W_{43}$): The POM material ($Eu_8P_4W_{43}$), polyoxotungstoeuropate, i.e., $K_{22}[(Eu_2PW_{10}O_{38})_4(W_3O_8(H_2O)_2(OH)_4]$, was prepared according to the literature method [22], while polycrystalline powders of the mesostructural aluminosilicate MCM-41 were prepared by using $C_{16}H_{31}(CH_3)_3NBr$ (Cetyltrimethylammonium Bromide, CTMABr) as surfactants according to ref. [21, 23]. To stabilize the synthesized MCM-41 and allow $Eu_8P_4W_{43}$ incorporation, it is necessary to modify

the interior structure of MCM-41 through use of a silylation reagent (specifically, (aminopropyl)triethoxysilane, i.e., NH_2-$(CH_2)_3$-Si-$(C_2H_5O)_3$ (APTES)), thus linking oxygen atoms on the aluminosilicate surface and rigidifying the mesoporous framework, as well as satisfying guest-host intermolecular and/or electrostatic interactions. For our studies, the modified MCM-41 was prepared according to ref. [24]. Briefly, about 1.5 g of the calcined MCM-41 was mixed with a chloroform solution of APTES (100 ml, 0.2 M) and stirred overnight at room temperature. The precipitate was filtered and washed with chloroform and dichloromethane.

Formation of $Eu_8P_4W_{43}$/MCM-41 Composite: A typical ion-exchange preparation of a $Eu_8P_4W_{43}$/MCM-41 composite involved stirring a mixture of 100 mg of modified MCM-41, 100 mg of $Eu_8P_4W_{43}$, and 20 ml of distilled water for over 24 h at room temperature with the pH held at about ca. 5 using 2 M H_2SO_4. The suspension was then centrifuged, and the supernatant aqueous solution decanted. The white powder (hereinafter designated $Eu_8P_4W_{43}$/MCM-41) was washed several times with pH/6 water to remove $Eu_8P_4W_{43}$ from the external surface and then dried in air.

Instrumentations: Steady-state emission and excitation spectra were acquired using a SPEX Fluorolog-□2 spectrofluorimeter. AFM was performed in air under ambient conditions using a TopoMetrix TMX2000 scanning probe microscope. The x-ray diffraction (XRD) instrument used was a Rigaku diffractometer, using Cu $K_{□1}$ (0.154 nm) x-rays: typically run at a voltage of 40 kV and current of 30 mA. IR spectra were taken on Thermo Nicolet Auntar 360 FTIR. The Raman spectrum was acquired using a J-Y LabRam HR800 micro-Raman instrument with 632.8 nm

excitation provided by a HeNe laser. Nitrogen isotherms were measured using an ASAP 2010 instrument (Micromeritics) at 77 K. Before each experiment, the samples were heated at 393 K and outgassed at this temperature under a vacuum of 10^{-5} Torr. The isotherms were then used to calculate specific surface area, micropore volume, and pore size distribution.

5.4 Results and Discussion

Topographical characterization of $Eu_8P_4W_{43}$ nanoparticles was conducted by atomic force microscopy (AFM). Figure 5-5 shows the AFM image of $Eu_8P_4W_{43}$ nanopartiles spin-coated on a mica slide. $Eu_8P_4W_{43}$ nanoparticles are clearly evident in the images. No aggregation was observed for $Eu_8P_4W_{43}$, which is ideal for such kind of Polyoxometalates to embedded in the pore of mesoporous materials. The Particle size is in the range of 1.8 nm to 2.7 nm and the average particle size is 2.3 nm in height. The result is consistent with the result from the calculation.

Structure and pore size of MCM-41 can be evaluated by the XRD and nitrogen desorption isotherms experiment. XRD patterns of pristine modified MCM-41 and the Polyoxometalate-incorporated composite ($Eu_8P_4W_{43}$/MCM-41) are shown in Figure 5-6. Using Bragg's equation and comparison with reference studies, the pore size of modified MCM-41 is estimated to be ca. 27 Å. This pore size is sufficiently large to allow $Eu_8P_4W_{43}$, of approximate dimensions (20 × 25) $Å^2$, to be incorporated into the modified MCM-41. The XRD patterns of the two samples show strong (100) peaks and proportional (110) and (200) peak intensities,

suggesting that the incorporation of Polyoxometalate in the channels does not affect the framework integrity of modified MCM-41.

For porous materials, the BJH pore size distribution, which is based on the Kelvin equation, is a useful method for the characterization of pore structure. Figure 5-7 shows the nitrogen adsorption–desorption isotherms of surface modified MCM-41 and $Eu_8P_4W_{43}$ embedded MCM-41 nanocomposite obtained at 77 K. All of the isotherms are of type IV classification, which is typical adsorption of mesoporous materials [25]. The BET surface area, pore volume and BJH pore diameter of the samples are listed in Table 1. Introduction of Polyoxometalate anions leads to a decrease in surface area and in pore volume. Such decrease in BET surface area, pore volume and BJH pore diameter of $Eu_8P_4W_{43}$/MCM-41 in comparison with that of MCM-41 implies $Eu_8P_4W_{43}$ nanoparticles have been confined inside the channels of MCM-41 [26].

The $Eu_8P_4W_{43}$ nanoparticles stabilized in MCM-41 matrixes provide a unique system for studying the luminescence and photophysical properties of POM nanoparticles. The rigid and non-connected one-dimensional channel structure protects the particles against aggregation or precipitation into solution. The excitation spectra (Figure 5-8; detection wavelength of 615 nm) of both solid-state $Eu_8P_4W_{43}$ and the composite $Eu_8P_4W_{43}$/MCM-41 exhibit maximum intensities at ca. 394 nm, with the intrinsic absorption band for the composite $Eu_8P_4W_{43}$/MCM-41 being somewhat broader. According to Figure 5-9 all the narrow peaks are due to f-f transitions within the $^4f_6$ configuration of the Eu^{3+} ion: 394 nm ($^7F_0$-$^5L_6$), 413 nm ($^7F_0$-$^5D_3$), and 466 nm ($^7F_0$-$^5D_2$) [27]. The broad band ranging from 350 to 370 nm

is corresponding to the O-W ligand-to-metal charge transfer (LMCT) [13]. It is to be noted that the exitation spectra for both samples are quite similar, indicating that $Eu_8P_4W_{43}$ anion structure does not change after it enters the channels of the MCM-41, and weak electrostatic interaction between the encapsulated Polyoxometalate and the surface walls of MCM-41.

Emission spectra of the pure solid-state $Eu_8P_4W_{43}$ and the composite $Eu_8P_4W_{43}$/MCM-41 are shown in Figure 6. Both emission spectra shown in Figure 5-10 exhibit bands near 536 nm corresponding to the $^5D_1 \rightarrow {}^7F_J$ transition, bands near 592 nm attributed to the $^5D_0 \rightarrow {}^7F_1$ transition, bands near 612 and 618 nm corresponding to the $^5D_0 \rightarrow {}^7F_2$ transition, a band near 647 nm corresponding to the $^5D_0 \rightarrow {}^7F_3$ transition, and a band near 699 nm corresponding to the $^5D_0 \rightarrow {}^7F_4$ transition [27, 28]. It is to be noted that the forbidden transition $^5D_0 \rightarrow {}^7F_0$ (Eu^{3+}), that would appear at ca. 578 nm, is present in the spectra of both samples. It is well-known that the $^5D_0$-$^7F_0$ transition is strictly forbidden in a field of symmetry. Hence, the above result reveals that Eu^{3+} in $Eu_8P_4W_{43}$ occupy sites with low symmetry and without an inversion center [29].

The $^5D_0$ - $^7F_1$ transition is a magnetic dipole transition, and its intensity varies with the crystal field strength acting on Eu^{3+}. On the other hand, the $^5D_0$ - $^7F_2$ transition is an electric dipole transition and is extremely sensitive to chemical bonds in the vicinity of Eu^{3+}. This is characteristic for the occupation the europium ions in silicon mesopores in low symmetry site. The intensity of the $^5D_0$ - $^7F_2$ transition increases as the site symmetry of Eu^{3+} decreases. Therefore, the intensity

ratio of the $^5D_0$ - $^7F_2$ transition to the $^5D_0$ - $^7F_1$ transition is widely used as a measure of the coordination state and the site symmetry of the rare earth. For $Eu_8P_4W_{43}$ nanocomposite, the strongest emission is in the $^5D_0$ - $^7F_2$ transition region and the $^5D_0$ - $^7F_2$ peak was split into two levels at 612 and 618 nm. The $^5D_0$ - $^7F_1$ transition was the next, and the emission peak was also split into two levels at 588 and 596 nm. The intensity ratio $I(^5D_0 - {}^7F_2)/I(^5D_0 - {}^7F_1)$ is equal to ca. 3.2, which also suggests the low site symmetry of the Eu^{3+} ion in nanocomposite [30].

Although exitation and emission spectra substantiate the incorporation of $Eu_8P_4W_{43}$ into MCM-41 mesoporous silica, convincing evidence for this can also be obtained by FTIR spectroscopy. Figure 5-11 is the FT-IR spectra of APTES modeified MCM-41 and $Eu_8P_4W_{43}$ before and after encapsulated inMCM-41. For MCM-41, the strongest bands relative to the silica host structure appear at 1000-1250 cm^{-1} and are due to asymmetric Si-O stretching vibration mode. 785 cm^{-1} can be attributed to the symmetric Si-O vibration. The Si-O-Si bending vibration can be observed at 475 cm^{-1}. The presence of water molecule can be observed the strong absorption bond at 1623 cm^{-1}. APTES modified MCM-41 show bond at 3249 cm^{-1} characteristic of the NH_2 groups and band at 2931 cm-1 characterstic of asymmetric vibrations of CH_2 group of propyl chain of the silylating agent [31]. For $Eu_8P_4W_{43}$, in the range 1000-700 cm^{-1} three characteristic bands were observed and assigned to the asymmetric stretching vibrations of the bridges (W-O_b-W) and of the terminal bonds (W-O_t). In the range of 1100-1000 cm^{-1}, asymmetric stretch vibration of the P-O band appear. The splitting of the characteristic P-O asymmetric stretching

vibration between 1100 and 1000 cm^{-1} suggests a decrease in the PO_4 group symmetry by coordination of the lanthanide ions to the ligand [32].

By comparing the FT-IR spectrum of MCM-41 samples (see Figure 5-11) before (A) and after encapsulation of $Eu_8P_4W_{43}$ (B) and (C), we find that the spectra displays the characteristic absorption peaks of both $Eu_8P_4W_{43}$ and MCM-41. Some bands were hidden upon formation of the composite, i.e. the 896.1 cm^{-1}, 765.3 cm^{-1} and bands around 1100 $cm^{-1,}$ due to the strong intensity of the MCM-41. Generally, the $M–O_d$ stretching can be considered as pure vibration and is an increase function of the anion–anion interaction. The $M–O_d$ and P-O asymmetrical stretching frequency of $Eu_8P_4W_{43}$ decreases from 955.1 to 939.5 cm^{-1} and 815.1 to 803.0 cm^{-1} when doped with MCM-41. This is attributed to the weakening of anion–anion interactions of the electrostatic type. We assume that due to the influences of silica such as the lengthening of the anion–anion distances, the anion–anion interactions are weakened [32].

Figure 5-12 shows Raman spectra of solid-state $Eu_8P_4W_{43}$ and the composite $Eu_8P_4W_{43}$/MCM-41. Similar Raman patterns for both samples are found. Both spectra have characteristic vibration peaks at ca. 218.2, 962.5, and 978.5 cm^{-1}, assigned to symmetric stretching γ_s ($W–O_t$; where O_t represents terminal oxygen), asymmetric stretching γ_{as} ($W–O_t$); and symmetric stretching γ_s ($W–O_i$, where Oi represents the bridging oxygen between the internal phosphorus heteroatom and tungsten addenda.). The relative weak bands at ca. 374, (860, 890, 912) and 1015 cm^{-1} are assigned to bending δ (W–O–W) and γ_s (W–O–P) and γ_{as} (W–O–P),

respectively. It is further to be noted that certain Raman bands for the composite vis-à-vis the respective bands for solid-state $Eu_8P_4W_{43}$ show blue shifts, e.g., the 218.2 and 215.7 for γ_s ($W–O_t$), 962.5 and 960.7 for and the 978.5 and 968.9 for γ_s, respectively. Based on the assignments above, an obvious explanation for the band shifts and their direction is that host-guest interaction between the negative-charged terminal oxygen and the $–NH^{3+}$ terminal functional group on the wall of MCM-41, which although weak, can be expected to promote redistribution of local electrons on the Polyoxometalate. The redistribution can be expected to decrease the electron densities of adjacent O, P and W atoms, leading to an increase in bond lengths of W–O and P–O, and an associated red shift. It is also important to notice that, for the Raman investigations, the vibration bands of polyoxometalate complexes shift towards higher energies providing evidence for an increase in polyoxometalate stability [33].

5.5 Conclusion

In summary, olyoxometalates with Keggin structure $Eu_8P_4W_{43}$ was introduced into mesoporous molecular sieve MCM-41 under weak acidic pH. Based on emission, excitation, FT-IR and Raman scattering measurements, the geometry of the Polyoxometalate ions was still preserved inside the channel of MCM-41 mesoporous structures, although some weak micro-environmental perturbation exists. Furthermore, by way of comparison of FT-IR and Raman band positions, we suggest that the incorporation of $Eu_8P_4W_{43}$ is implemented by host-guest interaction between the negative-charged terminal oxygen and $–NH^{3+}$ terminal functional group on the wall of MCM-41 at an appropriate pH. Due to its well-

organized stable structure and luminescent property, such a composite might represent a new material with potential applications as a photoluminescent device or phosphor.

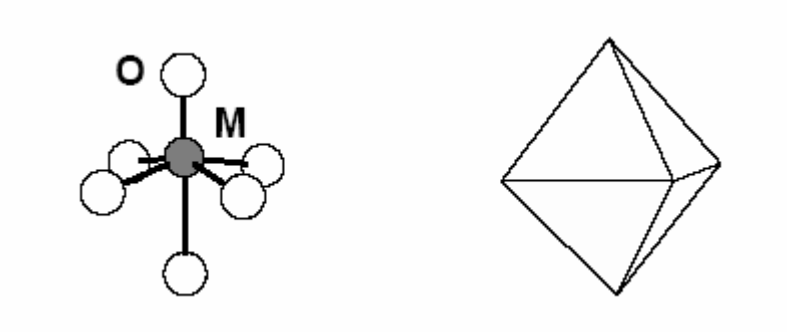

Figure 5-1: Ball-and-stick and polyhedral representations of the fundamental unit MO6. Note that the M atom is displaced off the geometrical centre of the octahedron towards one of the oxygens, thus giving rise to a distorted *C*4*v* unit.

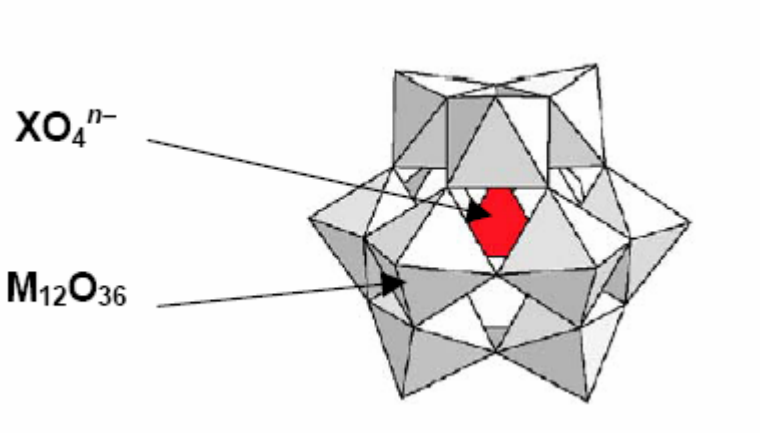

Figure 5-2: Polyhedral view of the clathrate-like structure of Keggin anion. The external $M_{12}O_{18}$ core encapsulates the internal unit.

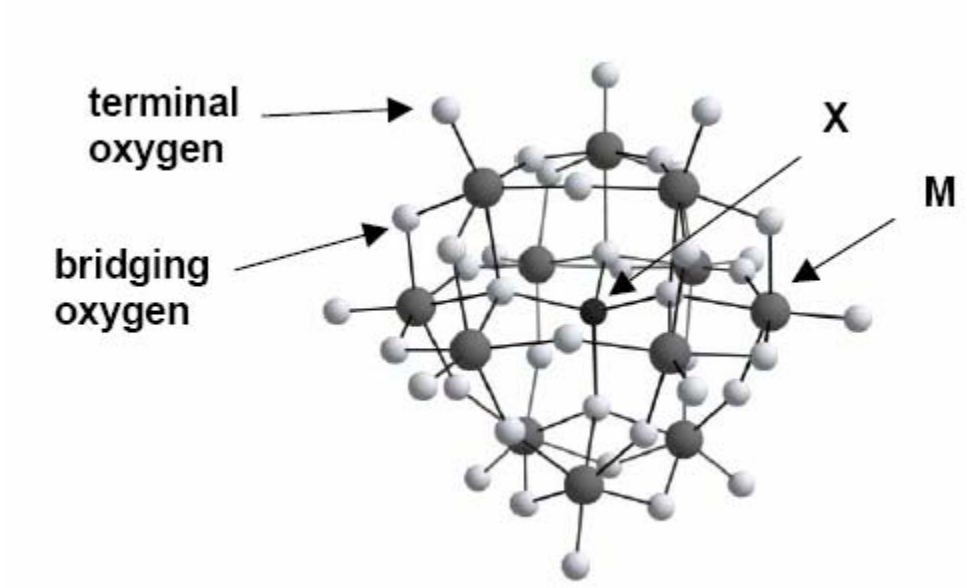

Figure 5-3: Ball-and stick representation of the Kegin heteropolyanion.

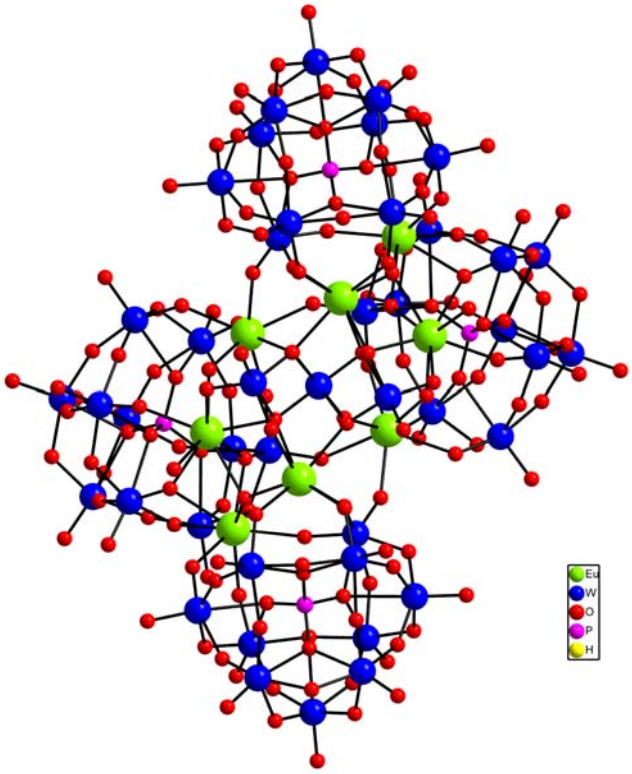

Figure 5-4: Ball and stick structure of the Polyoxometalate.

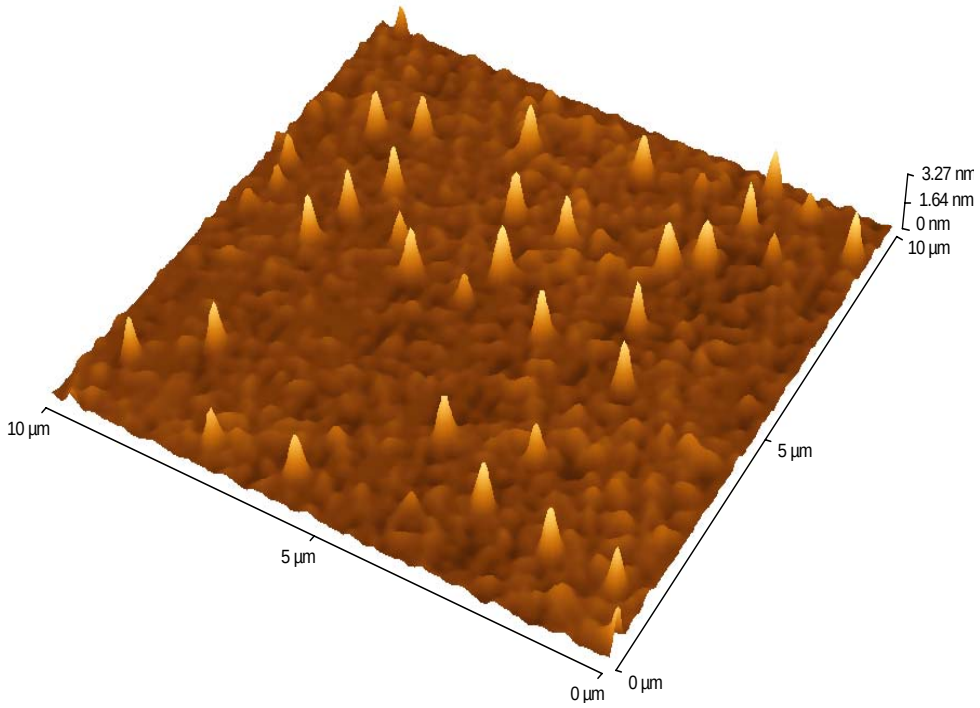

Figure 5-5: AFM image of the Polyoxometalate spin-coated on mica..

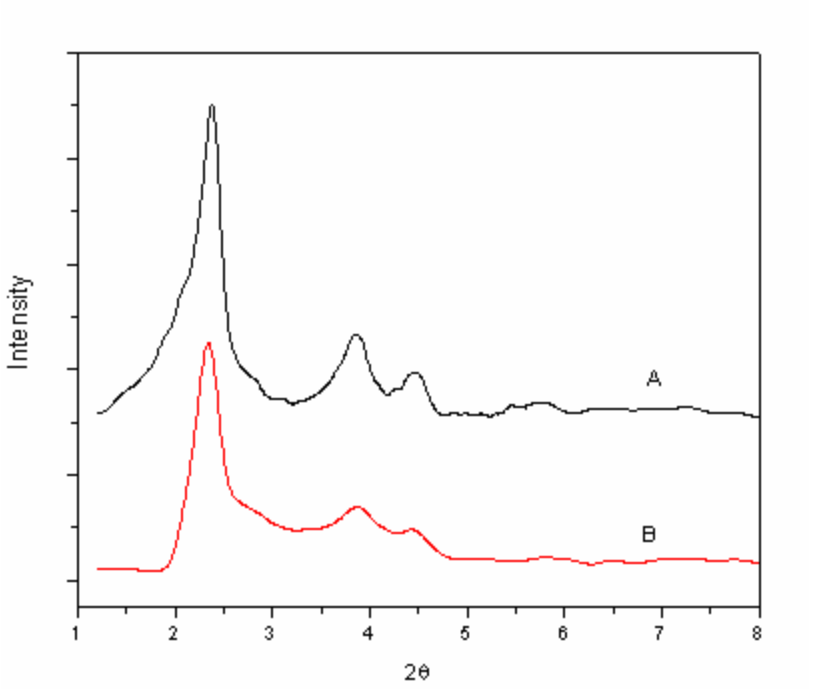

Figure 5-6: XRD patterns of (A) modified MCM-41, and (B) $Eu_8P_4W_{43}$/MCM-41.

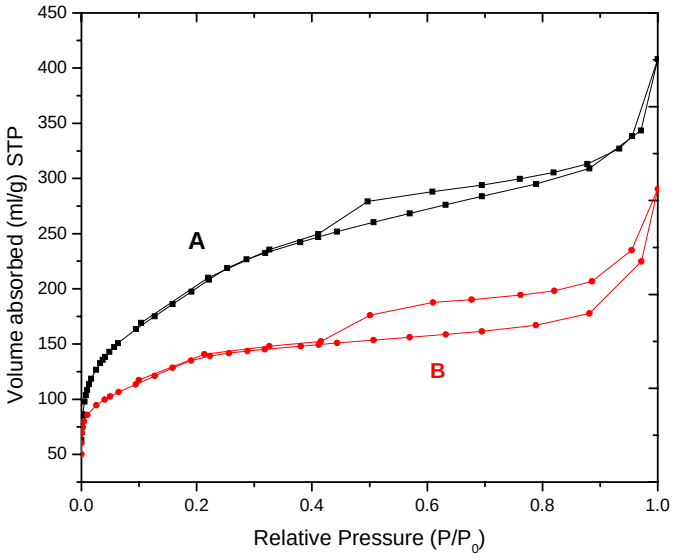

Figure 5-7: N_2 adsorption–desorption isotherms of (A) modified MCM-41, and (B) $Eu_8P_4W_{43}$/MCM-41.

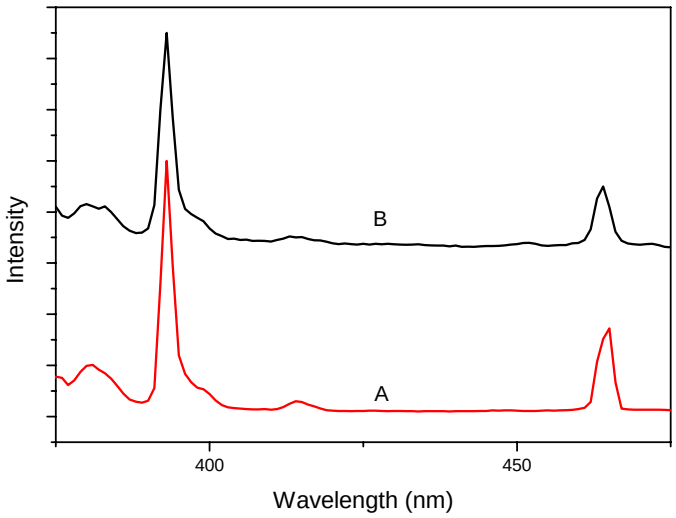

Figure 5-8: Excitation spectra of (A) solid $Eu_8P_4W_{43}$ and (B) composite $Eu_8P_4W_{43}$/MCM-41. Spectra were taken at 615 nm.

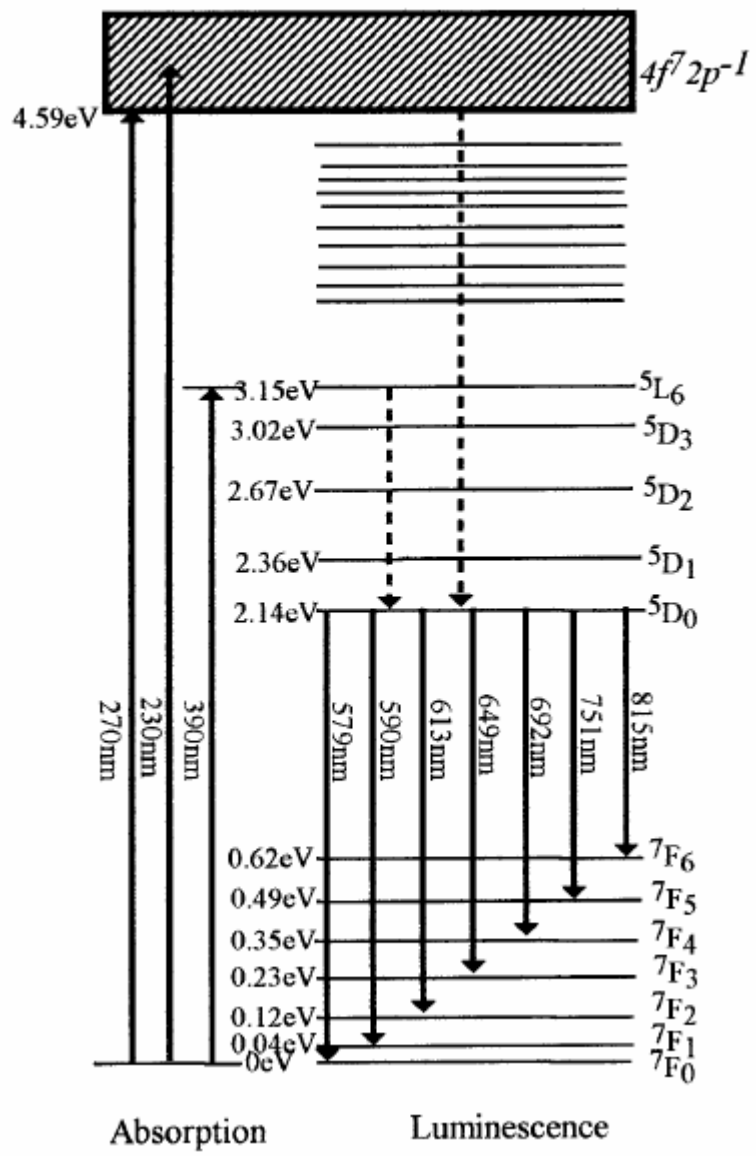

Figure 5-9: Energy level diagram of optical transitions of Eu(III)

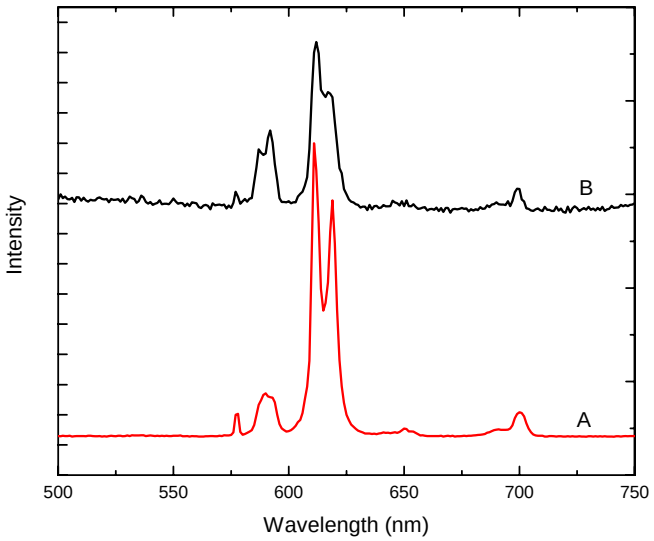

Figure 5-10: Emission spectra of (A) solid $Eu_8P_4W_{43}$ and (B) composite $Eu_8P_4W_{43}$/MCM-41, excited at 394 nm.

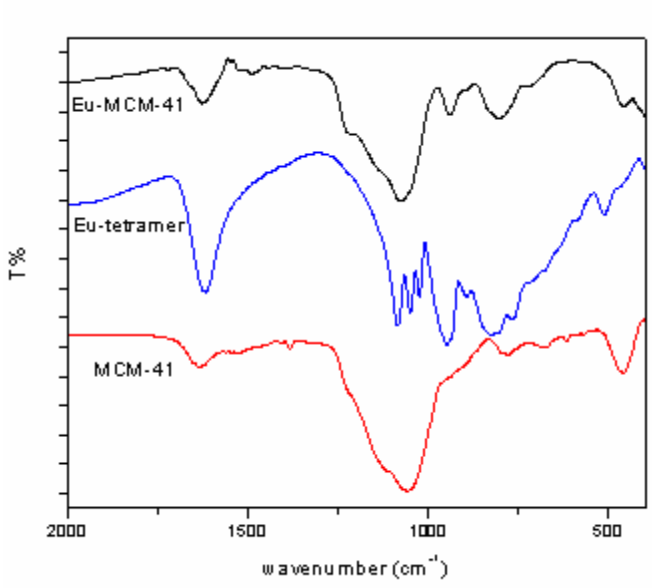

Figure 5-11: FT-IR spectra of (A) solid $Eu_8P_4W_{43}$ and (B) composite $Eu_8P_4W_{43}$/MCM-41.

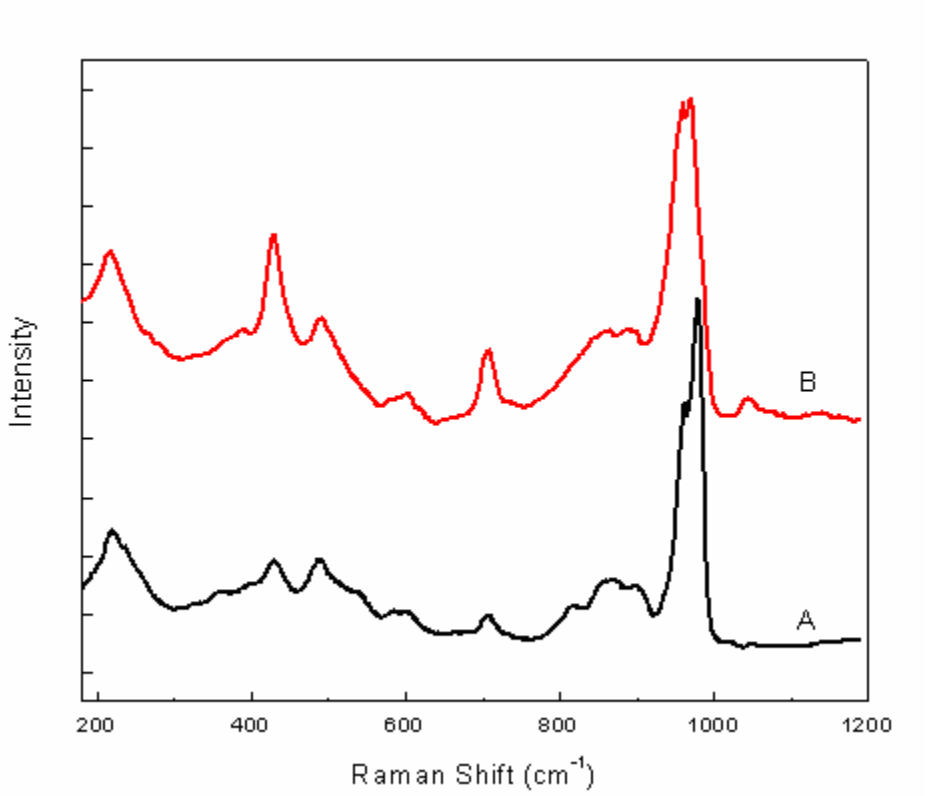

Figure 5-12: Raman spectra of (A) solid $Eu_8P_4W_{43}$; (B) composite $Eu_8P_4W_{43}$/MCM-41. Excitation wavelength is 615 nm.

Table 5-1: Pore structure parameters of (A) modified MCM-41, and (B) Eu8P4W43/MCM-41.

Samples	**S_{BET} (m^2g^{-1})**	**V_p (cm^3g^{-1})**	**d_{BJH} (nm)**
MCM-41	383.45	0.83	2.6
$Eu_8P_4W_{43}$/MCM-41	214.76	0.48	1.0

Chapter 6 Synthesis and Spectral Studies of Eu^{3+} in Mesoporous Sieves

Introduction

Luminescent materials, conventionally known as phosphors, are energy converters. These materials absorb energy from external energy sources such as high-energy photons, electrons, electric fields, chemical reactions, and other non-thermal sources, and re-radiate it as electromagnetic radiation over and above thermal radiation. light emission is produced by the relaxation of electrons from excited to ground states which produces photons with energies equal to the energy gap between the two transition states.

There are several terms used to describe the process by which luminescent materials emit electromagnetic radiation. Generally the types of luminescence can be characterized by the decay time, or the rate of electromagnetic radiation decays after the excitation ceases. Below are some of the several terms used to describe the types of luminescence, however luminescence is the general term used to describe all luminescent processes

1) Fluorescence describes very fast decay times, 10^{-9} to 10^{-3} seconds (1 ns to 1 ms)

2) Phosphorescence describes slower decay times 10^{-3} to 10 seconds

3) After glow describes very slow luminescent decay, greater than 10 seconds

Luminescent materials are either electrically semiconducting (band gaps < 3 eV) or insulating (band gaps > 3 eV). The differences in the band gaps give rise to

two mechanisms of luminescence; band gap and characteristic luminescence, respectively. For the former, luminescence occurs by electrons making transitions from the conduction to valence bands. Acceptor and donator ions influence the luminescent properties by introducing states into the band gap while the crystal field only dictates the energy gap between the valence and conduction bands. Characteristic luminescence arises by electrons making transitions from higher energy to lower energy states at localized centers, for instance at the site of the activator ion. In most cases, no visible transitions are seen by electrons transitioning between the conduction and valence bands in insulating materials due to the large energy gap, but do play a role in how the material luminescences.

For rare-earth ions, emission comes primarily from partially allowed f-f transitions when located in a solid. The splitting of the 4f levels of the rare-earth metals are not heavily influenced by the ligand field, because they are well shielded by the larger and completely filled 5s and 5p shells. The 6s shell is also completely filled and one electron is located in the 5d orbital for all rare-earths and is due to Hund's rule. The 4f electrons are heavily attracted by the nucleus, and is why they are shielded by the larger orbitals of the 5s and 5p electrons. The rare-earths are normally trivalent in the host lattice, with the two 6s and one 5d electron stripped off to create a trivalent ion. The 4f electrons first go in with all their spins parallel up until Gadolinium ($4f^7$), and then start to pair up until the 4f shell is full with Lutetium ($4f^{14}$).

The unique physical and chemical properties of the lanthanide make them useful in a variety of diverse applications, including phosphors, display monitors,

X-ray imaging, scintillators, lasers, and amplifiers for fiber-optic communication [1,2]. The luminescence of Eu^{3+} is particularly interesting because the major emission band is centered near 612 nm (red), which is one of the three primary colors, from which a wide spectrum of colors, including white, can be generated by appropriate mixing. For this reason, Eu^{3+} has been thoroughly investigated as a luminescent activator in many host lattices. The luminescence efficiency of these materials is often limited by the dynamics of the lanthanide ions, which depends on interactions with the host. The rationale to encapsulate Eu^{3+} within various hosts arises because the spectral and dynamic properties of these composites change when the reduced dimensions affect the chemistry and physical properties of the host. In a similar manner, the Eu^{3+} can also serve as a sensitive probe of the chemistry and structure of the hosts.

In our chapter, we tried to encapsulate Eu^{3+} in various mesoporous sieves, MCM-41, and Nb_2O_5, to study the spectral of Eu^{3+} in different environments. And also from the spectral studies, Eu^{3+} can act as a probe to detect the structure, defect of various matrices.

Experimental

Chemicals

For Synthesis MCM-41, Dodecyltrimethylammonium bromide (DOTAB) was used as template, which is from Aldrich. Tetraethyl orthosilicate (TEOS) was purchased from Spectrum. Trimethylammonium hydroxide (TMAOH) (25wt%, Aldrich0 was used. Commercial Nb_2O_5 with pore size 22 Å bought from Alfa

Aesar was used as one host. $Eu(NO_3)_3 \cdot 6H_2O$ (99.9%) was ordered from Alfa Aesar.

Synthesis of mesoporous sieves:

MCM-41 was synthesized with TEOS, DOTAB and TMAOH according to the ratio Si: DOTAB: TMAOH: H_2O=1.0:6.0:0.3:60 [3]. The mixture was stirred for 4h at room temperature, then transferred to Teflon-lined autoclave and heated at 393K for 1 day. The as synthesized powder was calcined at 873K for 6h.

Synthesis Eu-doped composites;

A typical method is mixing 0.2g mesoporous sieves and 20 ml 2g/l ethanolic $Eu(NO_3)_3 \cdot 6H_2O$ solution, adjusted pH value at ~6 and sonicated at room temperature for 2h [4,5]. The resultants were centrifuged and washed twice by ethanol and dried.

Instrumentation:

Absorption spectra were recorded using a Perkin-Elmer, Lambda 18, UV-vis-NIR spectrometer. The X-ray diffraction (XRD) instrument used was a Rigaku diffractometer using Cu $K_{\alpha 1}$ (0.154 nm) X-rays: typically run at a voltage of 40 kV and current of 30 mA. Steady-state fluorescence spectra were acquired using a SPEX, Fluorolog-ι2 spectrofluorometer. X-ray photonelectron spectrum was obtained by PHI 5500 ESCA (XPS)/ISS system.

Results and Discussion:

The X-ray patterns of those three mesoporous materials and Eu-doped composites are listed in Figure 1. All of these mesoporous materials show (100)

peaks. For MCM-41, it shows d spacing at 29 Å. A sample of mesoporous niobium oxide with a pore size of 22 Å displaying a peak in the XRD at d=32 Å. From the X-ray pattern, we can find out that MCM-41 is the most uniform structure, for the (100) peak is sharp and strong, while for the Nb_2O_3, the (100) peak is quite broad, which mean this kind of structure is more near amorphous structure. After encapsulation of the Eu_2O_3 nanoparticles, the structure of these two materials still maintained. In the long angle range, we can hardly find any peaks for those three samples in the long angle range, consistent with the idea that the nanoparticles formed are of extremely small diameters, less than 5nm . So although the pore sizes of these three materials are not so near, but it does not effect the Eu_2O_3 size too much, so that we can ignore this part effect.

Figure 2 listed the XPS signal of these three composites. In the inset of figure 2a, MCM-41/Eu_2O_3 composite, in the energy range of the Eu(3d) , on the basis of published Eu(3d) spectra of Eu_2O_3, we can assign the predominant peak around 1134eV to a Eu^{3+}(3d4f6)configuration. The other smaller peak around 1125 eV is attributed to a Eu^{2+} 5/2(3d4f7) configuration. The other 3/2 appears at 1165 and 1156 eV for +3 and +2, respectively. The existence of the divalent peak is found also by others, and in fact it always accompanies the XPS of Eu^{3+} ions. Its appearance may be due to the following possible reasons. The first possibility is that the divalent component comes from the surface layers, whose ground state is different from the bulk because of different geometric environments. This phenomenon of the so-called "surface valence transition" has been observed before in many rare-earth metallic compounds including europium. The other possibility is

that ground states of these commonly believed trivalent compounds are actually mixed valent, with both bivalent and trivalent components coexisting in the bulk ground state. In the Silica (2p) range, we observe one peak around 103 eV, assigned to the Si ($2p_{3/2}$) on the molecule sieves. And also we notice the Oxygen (1s,sat) around 541 eV, which suggest the oxide formation. The XPS of Nb_2O_5/Eu_2O_3 is shown in the figure 2b, we also observe peaks at 1125 eV and 1134 eV, and 1156 eV. (I_{1125}/I_{1134}=0.44) But compared with that of MCM-41/Eu_2O_3, we observe the relative intensity of I_{1125}/I_{1134} (0.25) is much stronger. So the surface valence transition is much stronger in this case. That's maybe due to this matrix and the nanoparticles are all lanthanide oxides.

Figure 3. is the DR-UV-Vis spectra of these three composites. For lanthanide elements, the optical transitions involve 4f orbitals, which are well shielded from their chemical environment by $^5s_2$ and $^5p_6$ electrons. The f-f transitions are parity forbidden. As a consequence, direct excitation of the lanthanide ions is unfavorable. .so we find out the RF-UV-vis of these three composites just mimic the absorption abilities of these three matrix. For example, the Eu/Nb_2O_5 shows same band absorption as Nb2O5 at middle point at 350nm. Eu/Er_2O_3 shows same band as Er_2O_3. , and at the same time, the peak which attribute to Eu^{3+} at 394nm is also observed. This is due to $^7F_j \rightarrow {}^5L_6$ transitions, which are the most intense 4f-4f absorption peaks. But for Eu^{3+} within MCM-41, the absorption is totally shielded by the silicate matrix. But the absorption around 230nm of 4f-4f72p-1 was seen.

The comparatively fast thermal relaxation of the excitation energy is a problem when using lanthanide ions for luminescence. This nonradiative relaxation may

occur by interaction of the electronic levels of the lanthanide ion with suitable vibrational modes of the environment. The efficency of these processes depends on the energy gap between the ground and excited states as well as the vibrational energy of the oscillators. For the MCM-41, which consists of a corner-sharing network of tetrahedarlly coordinated SiO_4 unites, only has low vibration quanta, which are not expected to contribute much to nonradiative deactivation of the excited state of the lanthanide ions. The photoluminescence was got by exciting the Eu^{3+} at 394nm. The structure is also confirmed by a consideration of the photoluminescence spectrum shown in Fig 4a. The $^5D_0 \rightarrow {}^7F_2$ is a hypersensitive transition and as such is highly dependent on environmental effects. It has been shown that this peak intensity is suppressed with respect to the $^5D_0 \rightarrow {}^7F_1$ upon a phase change to B-type monoclinic Eu_2O_3. In the nanocrystalline form of Eu_2O_3 described here, the emitting center does not occupy a center of symmetry. In such case, forced electric dipole transitions are possible, due to admixing of states of opposite parity by the crystal field. As $^5D_0 \rightarrow {}^7F_{2,4,6}$($^5D_0 \rightarrow {}^7F_2$, 612nm, $^5D_0 \rightarrow {}^7F_4$, 697nm) are strong, and then the emission is in the red. Magnetic dipole transitions $\Delta J=0,\pm1$ are also observed at 579nm($^5D_0 \rightarrow {}^7F_0$). If the Eu^{3+} center in a luminescent crystal is at a center of symmetry then only magnetic dipole transitions are observed and the emission appears orange.

Conclusion

Eu(III) doped MCM-41 and Nb_2O_5 were obtained. Surface valence transition of Eu(III) and Eu(II) is observed, which is much stronger in Nb_2O_5 mesoporous matrix. $7F_j \rightarrow 5L_6$ transitions around 394nm is totally shielded for Eu(III) in MCM-

41. But this band can be found in Eu(III)/Nb_2O_5 composite. For the MCM-41, which consists of a corner-sharing network of tetrahedarlly coordinated SiO4 unites, only has low vibration quanta, which are not expected to contribute much to nonradiative deactivation of the excited state of the lanthanide ions. And Eu(III) in MCM-41, the magnetic dipole transition is more obvious than that of Eu(III) in Nb_2O_5.

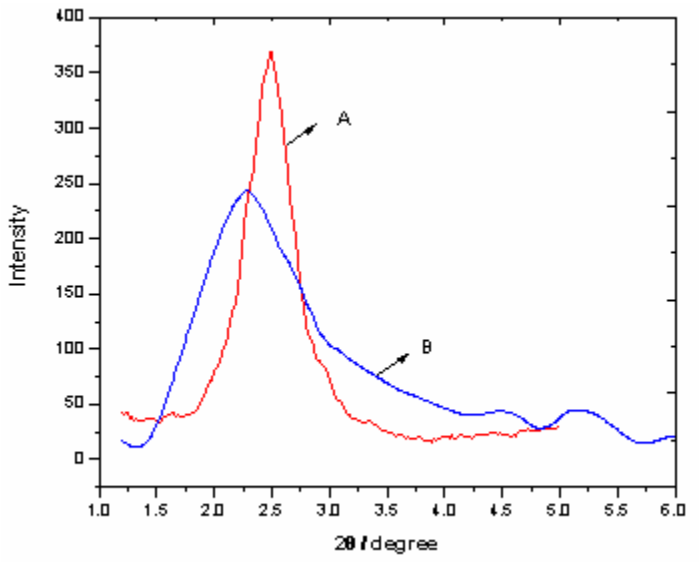

Figure 6-1. XRD patterns of (A) MCM-41; (B) Nb_2O_5.

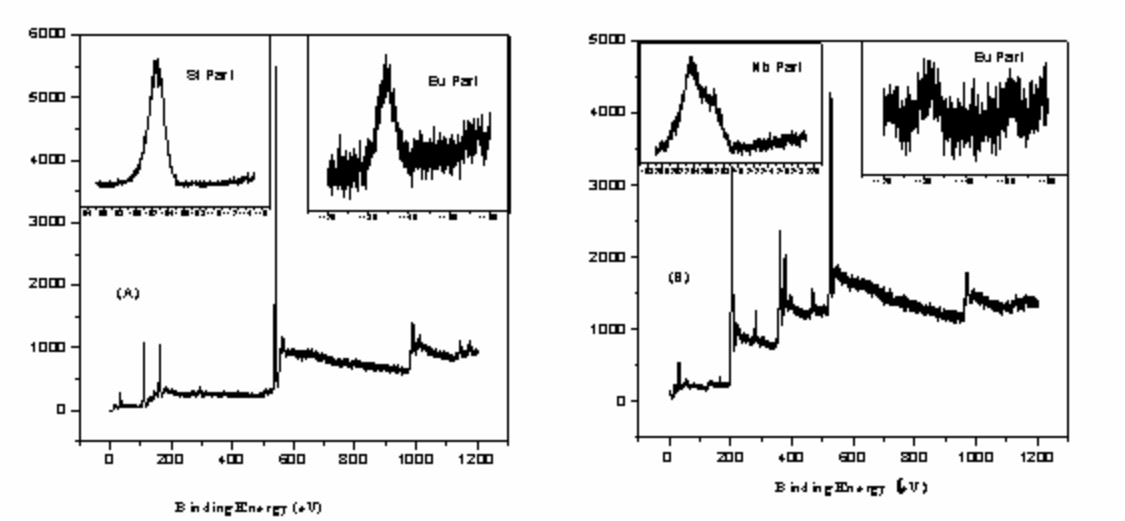

Figure 6-2. XPS of (A) MCM-41/Eu_2O_3 composites; (B) Nb_2O_5/Eu_2O_3 composites; (C) Er_2O_3/Eu_2O_3.

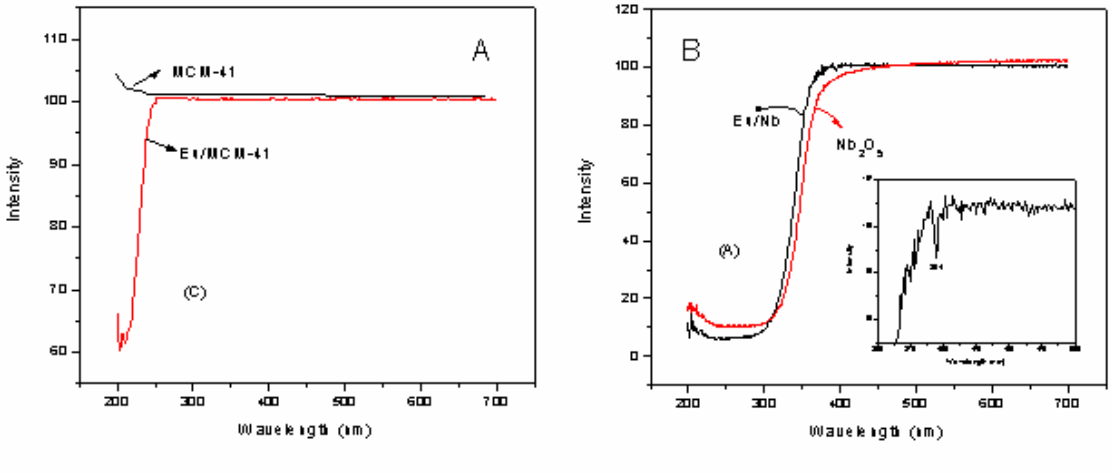

Figure 6-3. RFUV-Vis of (a)Eu_2O_3/MCM-41, and (b)Eu_2O_3/Nb_2O_5 composite.

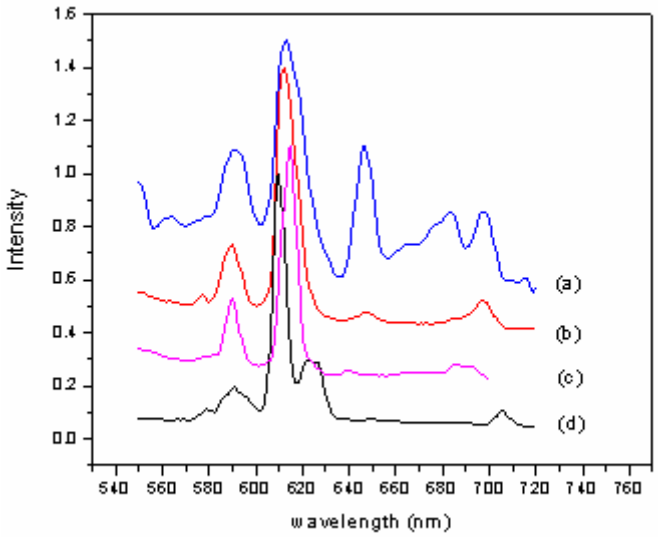

Figure 6-4 Fluorescence of (a) Eu_2O_3/MCM-41, (b) Eu_2O_3/Nb_2O_5, (c) $Eu(NO_3)_3$ and (d) Bulk Eu_2O_3.

REFERENCES

References for Chapter One

[1] Interrante, L. V.; Hampden-Smith, M. J. In Chemistry of Advanced Materials, An Overview **1998**, WILEY-VCH.

[2] Rao, C. N. R. Chemistry of Advanced Materials, A 'Chemistry for the 21 st Century' monograph, **1993**, Blackwell Scientific Publications, Oxford.

[3] Rao, C. N. R. J. Mater. Chem. **1999**, 9, 1.

[4] Alivisatos, A. P.; Barbara, P. F.; Castleman, A. W.; Chang, J.; Dixon, D. A.; Klein, M. L.; McLendon, G. L.; Miller, J. S.; Ratner, M. A.; Rossky, P. J.; Stupp, S. I.; Thompson, M. E. Adv. Mater. **1998**, 10, 1297.

[5] Ozin, G. A. Adv. Mater. **1992**, 4, 612.

[6] Chakravorty, D.; Giri, A. K. Chemistry of Advanced Materials, A 'Chemistry for the 21 st Century' monograph, **1993**, Blackwell Scientific Publications, Oxford.

[7] Smalley, R. E. Nanotechnology - A Revolution in the Making -- Vision for R&D in the Next Decade **1999**, Interagency Working Group on Nanoscience, Engineering, and Technology.

[8] Antonietti, M.; Göltner, C. Angew. Chem. Int. Ed. Engl. **1997**, 36, 911.

[9] Wallraff, G. M.; Hinsberg, W. D. Chem. Rev. **1999**, 99, 1801.

[10] Göltner, C. G.; Antonietti, M. Adv. Mater. **1997**, 9, 431.

[11] Hulteen, J. C.; Martin, C. R. J. Mater. Chem. **1997**, 7, 1075.

[12] Gonsalves, K. E.; Rangarajan, S. P.; Wang, J. Handbook of Nanostructured Materials and Nanotechnology, Volume 1, Synthesis and Processing, **2000**, Academic Press.

[13] Wang, Z. L. Characterization of Nanophase Materials **2000**, WILEY-VCH.

[14] Kresge, C. T.; Leonowicz, M. E.; Roth, W. J.; Vartuli, J. C.; Beck, J. S.; Nature, **1992**, 359, 710.

[15] Beck, J. S.; Vartuli, J. C.; Roth, W. J.; Leonowicz, M. E.; Kresge, C. T.; Schmitt, K. D.; Chu, C. T.-W.; Olson, D. H.; Sheppaard, E. W.; McCullen, S. B.; Higgins, J. B.; Schlenker, J. L. J. Am. Chem. Soc. **1992**, 114, 10834.

[16] Tanev, P. T.; Pinnavaia, T. J. Science **1995**, 267, 865.

[17] Attard, G. S.; Glyde, J. C.; Göltner, C. G. Nature **1995**, 378, 366.

[18] (a) Raman, N. K.; Anderson, M. T.; Brinker, C. J. Chem. Mater. **1996**, 8, 1682. (b) Sayari, A.; Liu, P. Microporous Mater. **1997**, 12, 149.

[19] A. Corma, Chem. Rev., 1997, 97, 2373.

[20] K. Moller and T. Bein, Chem. Mater., 1998, **10,** 2950.

[21] C. Garcia, Y. Zhang, F. DiSalvo and U. Wiesner, Angew. Chem., Int. Ed., 2003,42, 1526.

[22] B. Hu and J. L. Shi, J. Mater. Chem., 2003, 13, 1250.

[23] F. Marlow, M. D. McGehee, D. Zhao, B. F. Chmekla and G. D. Stucky, Adv. Mater., 1999, 11, 632.

[24] G. Wirnsberger, P. Yang, H. C. Huang, B. Scott, T. Deng, G. M. Whitesides, B. F. Chmelka and G. D. Stucky, J. Phys. Chem. B, 2001, 105, 6307.

[25] G. Wirnsberger and G. D. Stucky, Chem. Mater., 2000,12, 2525.

[26] J. Sauer, F. Marlow, B. Spliethoff and F. Schiith, Chem. Mater.,2002, 14, 217.

[27] (a) A.-B. Badiei and L. Bonneviot, Inorg. Chem., 1998, 37, 4142; (b) B. M. Weckhuysen and R. A. Schoonheydt, Chem. Commun., 1999, 445.

[28] L. K. Van Looveren, D. F. Geysen, K. A. Vercruysse, B. H. Wouters, P. J. Grobet and P. A. Jacobs, Angew. Chem., Int. Ed., 1998,37(4), 517.

[29] R. Mokaya and W. Jones, J. Mater. Chem., 1999, 9, 555.

[30] W. H. Zhang, J. L. Shi, L. Z. Wang and D. S. Yan, Chem. Mater., 2000, 12, 1408.

[31] W. H. Zhang, J. L. Shi, H. R. Chen, Z. L. Hua and D. S. Yan, Chem. Mater., 2001, 13, 648.

[32] Z. T. Zhang, S. Dai, X. Fan, D. A. Blom, S. J. Pennycook and Y.

Wei, J. Phys. Chem. B, 2001, 105, 6755.

[33] (a) T. Hirai, H. Okubo and I. Komasawa, J. Phys. Chem. B, 1999, 103, 4228; (b) T. Hirai, H. Okubo and I. Komasawa, J. Colloid Interface Sci., 2001, 235, 358.

[34] W. Xue, Y. Liao and D. L. Akins, J. Phys. Chem. B, 2002, 106, 11127.

[35] S. Subbiah and R. Mokaya, Chem. Commun., 2003, 860.

[36] A. Fukuoka, H. Miyata and K. Kuroda, Chem. Commun., 2003, 284.

References for Chapter Two

[1] Verhoeven, J. W. Pure Appl. Chem. **1990**, 63, 1585.

[2] Khundkar, L. R.; Stiegman, A. E.; Perry, J. W. J. Phys. Chem. **1990**, 94, 1224.

[3] Lueck, H.; Windsor, M.; Rettig, W. J. Phys. Chem. **1990**, 94, 4550.

[4] Launay, J. P.; Sowinska, M.; Leydier, L.; Gourdon, A.; Amouyal, E.; Boillot, M. L.; Heisel F.; Miehé, J. A. Chem. Phys. Lett. **1989**, 160, 89.

[5] Spange, S.; Zimmermann, Y.; Graeser, A. Chem. Mater. **1999**, 11, 3245.1.

[6] Yoshizawa, M.; Kubo, M.; Kurosawa, M. J. Lumin. **2000**, 87-89, 739.

[7] Bingermann, D.; Ernsting, N. P. J. Chem. Phys. **1995**, 102, 2691.

[8] Moulik, S. P.; Pal, B. K. Adv. Coll. Int. Sci. **1998**, 78, 99.

[9] Easter, D. C.; Baronavski, A. P. Chem. Phys. Lett. **1993**, 201, 153.

[10] Van der Meulen, P.; Zhang, H.; Jonkman A. M.; Glasbeek, M. J. Phys. Chem. **1996**, 100,5367.

[11] Gustavsson, T.; Baldacchino, G.; Mialocq J. -C.; Pommeret, S. Chem. Phys. Lett. **1995**, 236, 587.

[12] Maciejewski, A.; Naskrecki, R.; Lorenc, M.; Ziolek, M.; Karolczak, J.; Kubicki, J.; Matysiak, M.; Szymanski, M. J. Mol. Struct. **2000**,555,1.

[13] Pal, S. K.; Sukul, D.; Mandal, D.; Bhattacharyya, K. J. Phys. Chem. B **2000**, 104, 4529.

[14] Pal, S. K.; Sukul, D.; Mandal, D.; Sen, S.; Bhattacharyya, K. Chem. Phys. Lett. **2000**, 327, 91.

[15] Pal, S. K.; Mandal, D.; Sukul, D.; Sen, S.; Bhattacharyya, K. J. Phys. Chem. B **2001**, 105, 1438.

[16] Pal, S. K.; Sukul, D.; Mandal, D.; Sen, S.; Bhattacharyya, K. Tetrahedron **2000**, 56, 6999.

[17] Pal, S. K.; Mandal, D.; Sukul, D.; Bhattacharyya, K. Chem. Phys. Lett. **1999**, 312, 178.

[18] Martin, M. M.; Plaza, P.; Meyer, Y. H. Chem. Phys. **1995**, 192, 367.

[19] Zhou, Y.; Liu, Y.; Zhao, X.; Jiang, M. J. Mol. Struct. **2001**, 545, 61.

[20] Mandal, D.; Sen, S.; Bhattacharyya K.; Tahara, T. Chem. Phys. Lett. **2002** 359, 77.

[21] Wu, D.; Wang, L.; Liu, Y.; Ning, Y.; Zhao, J.; Liu, X.; Wu, S.; He, X.; Lin, J.; Wang, L.; Ma, D.; Wang, D.; Jing, X.; Wang, F. Synth. Metals. **2000**, 111-112, 563.

[22] Liu, C. J.; Li, S. G.; Pang, W. Q.; Che, C. M. Chem. Commun. **1997**, 65, 78.

[23] Galletero, M. S.; García, H.; Bourdelande, J. L. Chem. Phys. Lett. **2003**, 370, 829.

[24] Fayed, T. A.; Organero, J. A; Garcia-Ochoa, I.; Tormo, L.; Douhal, A. Chem. Phys. Lett. **2002**, 364, 108.

[25] (a) Xu, W.; Guo, H.; Akins, D. L. J. Phys. Chem. B **2001**, 105, 1543; (b) Xu, W.; Guo, H.; Akins, D. L. J. Phys. Chem. B **2001**, 105, 7686.

[26] Wery, E. In Effects of Molecular Environment on flourescence and Phosphorescence; Marcel Dekker, Ed.; New York, **1990**.

[27] Sarkar, N.; Das, K.; Nararyan Nath, D.; Bhattacharyya, K. Langmuir **1994** 10, 326.

[28] Datta, A.; Mandal D.; Kumar Pal, S.; Bhattacharyya, K. J. Phys. Chem. B. **1997**, 101, 10221.

[29] Kim, Y.; Lee, B. I.; Yoon, M. Chem. Phys. Lett. **1998**, 286, 466.

[30] Gu, G.; Ong P. P.; Li, Q. J. Phys. D: Appl. Phys. **1999**, 32, 2287.

[31] Márquez, F.; Garcia, H.; Palomares, E.; Fernández, L.; Corma, A J. Am. Chem. Soc. **2000**, 122, 6520.

[32] Yang, J.; He, Q.; Lin, H.; Fan, J.; Bai, F. Macromol. Rapid Commun. **2001**, 22, 1152.

[33] Kubelka, P. J. Opt. Soc. Am. **1948**, 38, 448.

References for Chapter Three

[1] M. Iwamoto, T. Abe, Y. Tachibana, J. Mol. Catal. A 155 (2000) 143.

[2] L. Huo, W. Li, L. Lu, H. Cui, S. Xi, J. Wang, B. Zhao, Y. Shen, Z. Lu, Chem. Mater. 12 (2000) 790.

[3] A. Bourlinos, A. Simopoulos, D. Petridis, H. Okumura, G. Hadjipanayis, Adv. Mater. 13 (2001) 289.

[4] B.M. Weckhuysen, D. Wang, M.P. Rosynek, J.H. Lunsford, Angew. Chem. Ini. Ed. Engl. 36 (1997) 2374.

[5] C. Pascal, J.L. Pascal, F. Favier, M.L.E. Moubtassim, C. Payen, Chem. Mater. 11 (1999) 141

[6] H. Guo, W. Xu, M.-H. Cui, N.-L. Yang, D.L. Akins, Chem. Comm. 12 (2003) 1432.

[7] J. Choma, W. Burakiewicz-Mortka, M. Jaroniec, Colloid Surface A 203 (2002) 97.

[8] A. Sayari, C. Danumah, I.L. Moudrakovski, Chem. Comm. 7 (1995) 813.

[9] A. Sayari, I. Moudrakovski, C. Danumah, C.I. Ratcliffe, J.A. Ripmeester, K.F. Preston, J. Phys. Chem. 99 (1995) 16373.

[10] D. Zhao, J. Feng, Q. Huo, N. Melosh, G.H. Fredrickson, B.F. Chmelka, G.D. Stucky, Science 279 (1998) 548.

[11] Z. Zhang, S. Dai, X. Fan, D.A. Blom, S.J. Pennycook, Y. Wei, J. Phys. Chem. B 105 (2001) 6755.

[12] A.B. Bourlinos, A. Simopoulos, N. Boukos, D. Petridis, J. Phys. Chem. B 105 (2001) 7432.

[13] J.F. Diaz, K.J.B. Jr., F. Bedioui, V. Kurshev, L. Kevan, Chem. Mater. 9 (1997) 61.

[14] X. Wang, X. Chen, X. Ma, H. Zheng, M. Ji, Z. Zhang, Chem. Phys. Lett. 384 (2004) 391.

[15] J. M. Xue, Z. H. Zhou, J. Wang, Mater. Chem. and Phys. 75 (2002) 81.

[16] K. Woo, h. J. Lee, J-P. Ahn, Y. S. Park, Adv. Mater. 15 (2003) 1761.

[17] S.E. Dapurkar, S.K. Badamali, P. Selvam, Catal. Today 68 (2001) 63.

[18] F. Jiao, B. Yue, K. Zhu, D. Zhao, H. He, Chem. Lett. 32 (2003) 770.

[19] C. Cannas, D. Gatteschi, A. Musinu, G. Piccaluga, C. Sangregorio, J. Phys. Chem. B 102 (1998) 7721.

[20] C. Cannas, G. Concas, D. Gatteschi, A. Falqui, A. Musinu, G. Piccaluga, C. Sangregorio, G. Spano, Phys. Chem. Chem. Phys. 3 (2001) 832.

[21] E.d. Barco, J. Asenjo, X.X. Zhang, R. Pieczynski, A. Julia, J. Tejada, R.F. Ziolo, Chem. Mater. 13 (2001) 1487.

References for Chapter Four

[1] Hench, L.L., J.K. West, and 1990, 33., Chem. Rev., 1990. 90: p. 33.

[2] Raman, N.K., M.T. Anderson, and C.J. Brinker, Chem. Mater., 1996. 8: p. 1682.

[3] Santra, S., R. Tapec, N. Theodoropoulou, J. Dobson, A. Hebard, and W. Tan, Langmuir, 2001. 17(10): p. 2900-2906.

[4] Huo, L., W. Li, L. Lu, H. Cui, S. Xi, J. Wang, B. Zhao, Y. Shen, and Z. Lu, Chem. Mater., 2000. 12(3): p. 790-794.

[5] Jing, Z. and S. Wu, J. Solid State Chem, 2004. 177(4-5): p. 1213-1218.

[6] Morales, M.P., T. Gonzalez-Carreno, M. Ocana, M. Alonso-Sanudo, and C.J. Serna, J. Solid State Chem, 2000. 155(2): p. 458-462.

[7] Leslie-Pelecky, D.L. and R.D. Rike, Chem. Mater., 1996. 8(8): p. 1770-1783.

[8] Ziolo, R.F., E.P. Giannelis, B.A. Weistein, M.P. O'Horo, B.N. Ganguly, V. Mehrotra, and M.W. Russell, Science, 1992. 257(5067): p. 219-223.

[9] Mayer, C.R., V. Cabuil, T. Lalot, and R. Thouvenot, Adv. Mater., 2000. 12(6): p. 417-420.

[10] Garcia, J.L., F.J. Lazaro, C. Martinez, and A. Corma, J. Magn. Magn. Mater., 1995. 140-144(Pt. 1): p. 363-364.

[11] Zhang, L., G.C. Papaefthymiou, and J.Y. Ying, J. Phys. Chem. B,

2001. 105(31): p. 7414-7423.

[12] Guo, H., W. Xu, M.-H. Cui, N.-L. Yang, and D.L. Akins, Chem. Commun., 2003. 12: p. 1432-1433.

[13] Perez-Robles, F., F.J. Garca-Rodrguez, S. Jimenez-Sandoval, and J. Gonzalez-Hernandez, J. Raman Spectrosc., 1999. 30: p. 1099.

[14] Faria, D.L.A.d., S.V. Silva, and M.T.d. Oliveira, J. Raman Spectrosc., 1997. 28: p. 873-878.

[15] Fabrizioli, P., T. Bu□gi, M. Burgener, S.v. Doorslaerb, and A. Baiker, J. Mater. Chem., 2002. 12: p. 619-630.

[16] Jitianu, A., M. Crisan, A. Meghea, I. Raub, and M. Zaharescu, J. Mater. Chem., 2002. 12: p. 1401?407.

[17] Bordiga, S., R. Buzzoni, F. Geobaldo, C. Lamberti, E. Giamello, A. Zecchina, G. Leofanti, G. Petrini, G. Tozzola, and G. Vlaic, J. Catal., 1996. 158: p. 486.

[18] Savii, C., M. Popovici, C. Enache, J. Subrt, D. Niznansky, S. Bakardzieva, C. Caizer, and I. Hrianca, Solid State Ionics, 2002. 151: p. 219-227.

[19] Chaneac, C., E. Tronc, and J.P. Jolivet, J. Mater. Chem., 1996. 6(12): p. 1905-1911.

[20] Cannas, C., D. Gatteschi, A. Musinu, G. Piccaluga, and C. Sangregorio, J. Phys. Chem. B, 1998. 102(40): p. 7721-7726.

[21] Aliev, F.G., M.A. Corra-Duarte, A. Mamedov, J.W. Ostrander, M. Giersig, L.M. Liz-Marzan, and N.A. Kotov, Adv. Mater., 1999. 11(12): p. 1106-1110.

[22] Testa, A.M., S. Foglia, L. Suber, D. Fiorani, L. Casas, A. Roig, E. Molins, J.M. Greneche, and J. Tejada, J Appl. Phys., 2001. 90(3): p. 1534-1539.

[23] Barco, E.d., J. Asenjo, X.X. Zhang, R. Pieczynski, A. Julia, J. Tejada, and R.F. Ziolo, Chem. Mater., 2001. 13(5): p. 1487-1490.

[24] Jolivet, J.-P., C. Chaneac, and E. Tronc, Chem. Commun., 2004: p. 481-487.

References for Chapter Five

[1] Berzelius, J.J., Ann. Phys. Chem., 1826. **6**: p. 369.

[2] Keggin, J.F., Nature, 1933. **131**: p. 908.

[3] Katsoulis, D.E., Chem. Rev., 1998. **98**: p. 359.

[4] Rhule, J.T., C.L. Hill, D.A. Judd, and R.F. Schinazi, Chem. Rev., 1998: p. 327.

[5] Coronado, E. and C.J. Gomez-Garcia, Chem. Rev., 1998. **98**(1): p. 273 -296.

[6] Briand, L.E., G.T. Baronetti, and H.J. Thomas, Applied Catalysis A: General, 2003. **256**(1-2): p. 37-50.

[7] Mizuno, N. and M. Misono, Chem. Rev., 1998. **98**(1): p. 199 -218.

[8] Inouye, Y., Y. Tokutake, T. Yoshida, Y. Seto, H. Hujita, K. Dan, A. Yamamoto, S. Nishiya, T. Yamase, and S. Nakamura, Antiviral Research, 1993. **20**(4): p. 317-331.

[9] Casafi-Pastort, N. and L.C.W. Baker, J. Am. Chem. Soc., 1992. **114**: p. 10384-10394.

[10] Muller, A., F. Peters, M.T. Pope, and D. Gatteschi, Chem. Rev., 1998. **98**(1): p. 239 -272.

[11] Tomsa, A.-R., L. Muresan, A. Koutsodimou, P. Falaras, and M. Rusu, Polyhedron, 2003. **22**(21): p. 2901-2909.

[12] Xu, L., E. Wang, Z. Li, D.G. Kurth, X. Du, H. Zhang, and C. Qin, New Journal of Chemistry, 2002. **26**(6): p. 782-786.

[13] Xu, L., H. Zhang, E. Wang, D.G. Kurth, and Z. Li, Journal of Materials Chemistry, 2002. **12**(3): p. 654-657.

[14] Damyanova, S., L. Dimitrov, R. Mariscal, J.L.G. Fierro, L. Petrov, and I. Sobrados, Applied Catalysis A: General, 2003. **256**(1-2): p. 183-197.

[15] Zhao, Z., W. Ahn, and R. Ryoo, Studies in Surface Science and Catalysis, 2003. **146**(Nanotechnology in Mesostructured Materials): p. 657-660.

[16] Lindlara, B., M. Luchingera, A. Rothlisbergera, M. Haouasa, G. Pirngrubera, A. Kogelbauerb, and R. Prins, J. Mater. Chem., 2002. **12**(3): p. 528 - 533.

[17] Kozhevnikov, I.V., K.R. Kloetstra, A. Sinnema, H.W. Zandbergen, and H. van Bekkum, J Mol Catal A: Chemical, 1996. **114**(1-3): p. 287-298.

[18] Jalil, P.A., M.A. Al-Daous, A.-R.A. Al-Arfaj, A.M. Al-Amer, J. Beltramini, and S.A.I. Barri, Appl Catal A: General, 2001. **207**: p. 159.

[19] Kurth, D.G. and D. Volkmer, Polyoxometalate Chemistry, 2001: p. 301.

[20] Kaleta, W. and K. Nowi′nska, Chem. Commun., 2001: p. 535-536.

[21] Xu, W., Q. Luo, H. Wang, L.C. Francesconi, R.E. Stark, and D.L. Akins, J. Phys. Chem. B, 2003. 1**07(**2): p. 497 -501.

[22] Zhang, C., R.C. Howell, K.B. Scotland, F.G. Perez, L. Todaro, and L.C. Francesconi, Inorg. Chem., 2004. 4**3(**24): p. 7691 -7701.

[23] Guo, H., X. Zhang, M. Aydin, W. Xu, H.-R. Zhu, and D.L. Akins, J. Mol. Struct., 2004. 6**89(**1-2): p. 153-158.

[24] Liu, C.-J., S.-G. Li, W.-Q. Pang, and C.-M. Che, Chem. Commun., 1997(1): p. 65-66.

[25] Zheng, S., L. Gao, Q. Zhang, W. Zhang, and J. Guo, J. Mater. Chem., 2001. 1**1(**2): p. 578 - 583.

[26] Nowinska, K., R. Formaniak, W. Kaleta, and A. Waclaw, Applied Catalysis A: General, 2003. 2**56(**1-2): p. 115-123.

[27] Naruke, H. and T. Yamase, J. Lumin., 1991. 5**0:** p. 55-60.

[28] Zhang, H.Y., L. Xu, E.B. Wang, M. Jiang, A.G. Wu, and Z. Li, Materials Letters, 2003. 5**7(**8): p. 1417-1422.

[29] Aquino, J.M.F.B., A.S. Araujo, D.M.A. Melo, J.E.C. Silva, M.J.B. Souza, and A.O.S. Silva, J Alloys and Compounds, 2004. 3**74(**1-2): p. 101-104.

[30] Wang, X., Y. Guo, Y. Li, E. Wang, C. Hu, and N. Hu, Inorg. Chem., 2003. 4**2(**13): p. 4135-4140.

[31] Joseph, T., S.S. Deshpande, S.B. Halligudi, A. Vinu, S. Ernst, and M. Hartmann, J Mol. Catal. A: Chemical, 2003. 2**06**: p. 13-21.

[32] Jin, H., Q. Wu, and W. Pang, Mater. Lett., 2004. 5**8(**29): p. 3657-3660.

[33] Tomsa, A.-R., L. Muresan, A. Koutsodimou, P. Falaras, and M. Rusu, Polyhedron, 2003. 2**2(**21): p. 2901-2909.

References for Chapter Six

[1] Tissue, B. M.; *Chem. Mater.;* **1998**; *10*(10); 2837-2845.

[2] Chen, W.; Joly, A. G.; Kowalchuk, C. M.; Malm, J.-O.; Huang, Y.; Bovin, J.-O.; *J. Phys. Chem. B. ;* **2002**; *106*(28); 7034-7041.

[3] Yoshitake, H.; Yokoi, T.; Tatsumi, T.; *Chem. Mater.;* **2002**; *14*; 4603.

[4] Pol, V. G.; Reisfeld, R.; Gedanken, A.; *Chem. Mater.;* **2002**; *14*; 3920.

[5] Pol, V. G.; Palchik, O.; Gedanken, A.; Felner, I.; *J. Phys. Chem. B. ;* **2002**; *106*; 9737.